Muon performance studies in ATLAS towards a search for the Standard Model Higgs boson

ACADEMISCH PROEFSCHRIFT

ter verkrijging van de graad van doctor
aan de Universiteit van Amsterdam
op gezag van de Rector Magnificus
prof. dr. D.C. van den Boom
ten overstaan van een door het college van promoties
ingestelde commissie,
in het openbaar te verdedigen in de Agnietenkapel
op donderdag 26 januari 2012, te 10:00 uur

door

Egge Freek van der Poel

geboren te Nchelenge, Zambia

Promotor:	Prof. dr. F.L. Linde
Copromotor:	Dr. drs. ir. P.M. Kluit
Overige leden:	Prof. dr. S.C.M. Bentvelsen
	Prof. dr. ir. P.J. de Jong
	Prof. dr. E.L.M.P. Laenen
	Prof. dr. R.J.M. Snellings
	Dr. F. Cerutti
	Dr. F. Filthaut
	Dr. M. Vreeswijk

Faculteit der Natuurwetenschappen, Wiskunde en Informatica

Cover: *Higgs, the end of the puzzle* door Daniel Karso en Egge van der Poel
Print: Ponsen & Looijen
ISBN: 978-90-6464-522-8

Dit werk maakt deel uit van het onderzoekprogramma van de Stichting voor Fundamenteel Onderzoek der Materie (FOM), die deel uit maakt van de Nederlandse Organisatie voor Wetenschappelijk Onderzoek (NWO).

Gerard Joling over de deeltjesversneller

hoeeeeee
hahahahahahahaha
ohhhhh wat een verschutting
een buis van 7 kilometer
keiharde delen die op elkaar botsen
en als toetje ook nog
een zwart gat
eeuwig zonde dat ik
nooit heb doorgeleerd

dichter/schrijver/muzikant Nico Dijkshoorn,
n.a.v. TV uitzending DWDD, 31 maart 2010

Contents

1 Particle physics: what and why? 1
1.1 Particle physics: what? . . . 1
1.2 Big questions about small particles . . . 3
1.3 The Large Hadron Collider project . . . 3
1.3.1 CERN . . . 4
1.3.2 The LHC . . . 4
1.4 The ATLAS detector . . . 5
1.4.1 The ATLAS Muon Spectrometer . . . 5
1.5 Particle physics: why? . . . 6
1.6 Thesis overview . . . 6

2 Production and decay of the Z and Higgs boson at hadron colliders 7
2.1 Elementary particles and forces in the Standard Model . . . 7
2.1.1 A closer look at the weak force . . . 9
2.2 Electroweak symmetry breaking . . . 12
2.3 Production and decay of the Z boson at hadron colliders . . . 17
2.3.1 Production of the Z boson . . . 17
2.3.2 Z decay channels . . . 19
2.3.3 The cross section for $pp \to q\bar{q} \to \gamma^*/Z \to \mu^-\mu^+$ . . . 20
2.4 Simulation of $Z \to \mu^-\mu^+$ in ATLAS . . . 21
2.5 Production and decay of the Higgs boson at the LHC . . . 23

3 Particle detection in the ATLAS detector 25
3.1 Introduction . . . 25
3.1.1 Coordinate system . . . 26
3.2 Trigger . . . 26
3.3 Magnet systems . . . 27
3.4 Detector technologies . . . 27
3.4.1 Inner Detector . . . 28
3.4.2 Calorimeter . . . 30

3.4.3 Muon Spectrometer . . . 32
3.5 Muon reconstruction algorithms . . . 37
3.5.1 Standalone muons . . . 38
3.5.2 Combined muons . . . 38
3.5.3 Segment tagged muons . . . 38
3.5.4 Calorimeter tagged muons . . . 38
3.5.5 Reconstruction of cosmic-ray muons . . . 39
3.6 Precision of the Muon Spectrometer . . . 41
3.7 Summary . . . 43

4 Performance of the Muon Spectrometer with cosmic-ray data 45
4.1 Introduction . . . 45
4.2 Data sample . . . 45
4.3 Sagitta resolution . . . 47
4.3.1 Introduction . . . 47
4.3.2 Event, track and segment selection . . . 48
4.3.3 Analysis of the sagitta resolution . . . 49
4.3.4 Results . . . 50
4.4 Momentum resolution . . . 51
4.4.1 Introduction . . . 51
4.4.2 Event and track selection . . . 53
4.4.3 Analysis of the momentum resolution . . . 54
4.4.4 Results . . . 54
4.5 Discussion . . . 56
4.6 Results of combined cosmic data taking . . . 57
4.7 Summary . . . 58

5 Performance of the Muon Spectrometer with collision data 59
5.1 Introduction . . . 59
5.2 Muon reconstruction efficiency . . . 59
5.2.1 Tag and probe method . . . 59
5.2.2 Data-set and event selection . . . 62
5.2.3 Results . . . 62
5.3 Muon momentum resolution studies . . . 66
5.3.1 Event selection . . . 68
5.3.2 Results . . . 68
5.4 Conclusions . . . 72

6 Observation of $Z \to \mu^-\mu^+$ in $PbPb$ collisions at $\sqrt{s_{NN}} = 2.76$ TeV 75

7 Search for $H \to ZZ^{(*)} \to \mu^-\mu^+\mu^-\mu^+$ in 1 fb^{-1} of 7 TeV pp collisions 93
7.1 Introduction . . . 93
7.2 Data-set . . . 93
7.3 Event selection . . . 94
7.4 Discovery/exclusion of a Higgs signal . . . 100

7.4.1 Results . . . 102
7.5 Conclusions . . . 105

8 Summary and conclusions **107**

A Momentum resolution **111**
A.1 Uncertainties . . . 111
A.2 Comparing $\sigma(s)$ to $\sigma(p_T)/p_T$ . . . 112

B Samples used for Higgs studies **113**

C More on the profile likelihood function **115**

References **117**

Samenvatting **123**

Acknowledgements **127**

1

Chapter 1

Particle physics: what and why?

1.1 Particle physics: what?

Particle physics is a field in science that studies the properties of and interactions between the smallest particles that we know of. These *elementary* particles are not visible in everyday life and are therefore unknown to most people. This is unfortunate as all of the wonderful world around us is built up from these ‘invisible’ particles, like the beautiful Victoria Falls shown in Figure 1.1.

Figure 1.1: Victoria Falls at the border of Zambia and Zimbabwe.

Let’s start with something that *is* known to everybody: water, like the water falling down in Figure 1.1. Almost everybody learned that water molecules are denoted by the chemical formula H_2O. Many people know about the hydrogen (H) and oxygen (O) atoms that build up the water molecules. A few have heard of protons and neutrons that build up the core of the atoms, and of electrons that circle around this core. Even fewer people know about the constituents of protons and neutrons, so-called *quarks*, and only a tiny group op people study the behavior of these quarks. These people are particle physicists. So why should society bother with this tiny group of interested specialists? Surely there are more urgent issues to address (and finance) nowadays.

Let's clarify things a bit further: from the water falling down the Victoria Falls we zoom in to the water molecules and subsequently to the atoms that constitute these molecules. From this point onwards you might start to feel uneasy. There is no need for that. Figure 1.2 illustrates the next stages in our quest for the smallest building blocks of matter. From the atom to the proton and neutrons in the atomic nucleus and on to the quarks that form these protons and neutrons. Quarks together with *leptons*, like the electron, are the elementary[1] building blocks of all matter. The properties of and interactions between these elementary particles are the subject of the field of study known as particle physics.

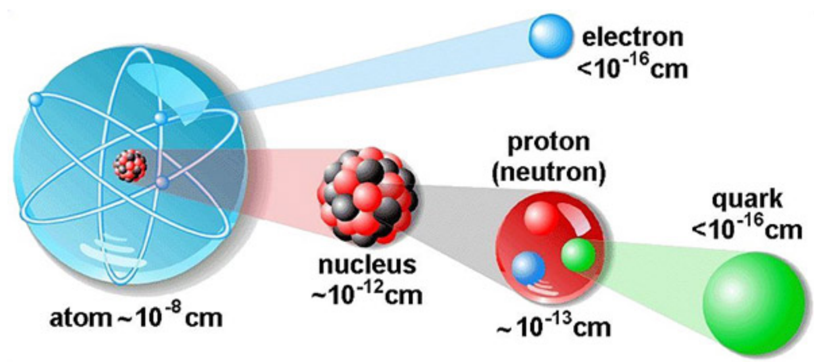

Figure 1.2: Zooming into the atomic structure.

Since the beginning of the twentieth century particle physics has gone through major developments, nicely and concisely described in ref. [2]. In 1910 Rutherford was the first to observe that the atom consists of a small nucleus. This nucleus was found to contain protons and neutrons, with electrons circling around it. As experimental techniques evolved, and theoretical knowledge deepened, eventually the existence of quarks was proven. Protons and neutrons were no longer classified as elementary particles but as composite particles, consisting of quarks. By probing deeper and deeper into the structure of atoms and their nuclei physicists needed to develop new technologies. The key issue was always to probe the particle of study at higher energy. The way current experiments achieve high energies sounds less sophisticated than it actually is: tiny particles are accelerated to almost the speed of light and then smashed into each other. The machines that do this are called particle accelerators. We will come to the largest accelerator ever built in Section 1.3, after we have described some of the biggest puzzles that currently exist.

[1] *Elementary* as far as we currently know. Another question is whether our knowledge actually describes physical reality. Quoting Niels Bohr on this: "It is wrong to think that the task of physics is to find out how nature *is*. Physics concerns what we can *say* about nature." [1]

1.2 Big questions about small particles

We have learned many things about elementary particles in the history of science. But by discovering new features about nature also new puzzles emerged. This is how science works: answers create puzzles which need to be answered again. Today, several big puzzles remain to be solved. Two puzzles will be explained here, others are discussed in the literature, see e.g. ref. [2].

As mentioned above, all matter consists only of quarks and leptons. All *detectable* matter that is. In 1980 measurements of velocity curves in spiral galaxies first showed that there is much more matter in such galaxies than can be accounted for by direct observation[2] [4]. At this moment the amount of observable matter is believed to be only 4%. An astonishing amount of 96% remains unknown and is usually referred to as dark matter and dark energy for 23% and 73%, respectively. To reveal the properties of dark matter is an important motivation for various experiments in (astro)particle physics.

Another motivation takes us back to the 4% of matter that *is* known to us. Let us refer to this 4% as ordinary matter. We mentioned the quarks and leptons that are the building blocks of this ordinary matter. Although too small to see with the naked eye these building blocks are in fact *massive* particles. This seems an obvious statement, if you think of the fact that in everyday life we are used to *massive* objects like rocks, cars, monkeys and people. That the building blocks of these objects themselves are also massive seems trivial. However, this is in fact far from trivial when setting up a formalism to describe particle interactions at the elementary level.

In the early 1960s a framework was in place to describe elementary particles and the forces that govern them. One minor issue was that all particles were predicted to be massless, which was in contradiction with many observations. It took some theoretical gymnastics to elegantly solve this puzzle. Peter Higgs was, simultaneously with Robert Brout and François Englert, one of the people that found a way out. His mechanism predicts the existence of a yet undiscovered particle, now called the Higgs boson. The discovery of this Higgs boson is referred to by some as the holy grail of particle physics. However you wish to qualify this quest, it was a major motivation for the construction of the Large Hadron Collider.

1.3 The Large Hadron Collider project

The Large Hadron Collider (LHC) is currently the largest and most powerful man-made particle accelerator. It is located at the European Organization for Nuclear Research, CERN[3], near Geneva, Switzerland.

[2] Fritz Zwicky was way ahead of his time and reported about "missing mass" already in 1933 [3].
[3] In French: Conseil Européen pour la Recherche Nucléaire.

1.3.1 CERN

CERN was founded in 1954 with the aim of creating a research center that would not only unite European scientists, but would also share the costs of constructing and operating technologically challenging experiments. The Netherlands were one of the twelve founding member states. CERN conducts experiments in nuclear physics and particle physics and has evolved from a European to a worldwide collaboration[4].

The first particle accelerator that came into operation in 1957 at CERN was the synchrocyclotron with a beam energy of 0.6 GeV (giga-electronvolt). It was soon replaced, for particle physics experiments, by the proton synchrotron in 1959. Its beam energy of 28 GeV was at that moment record breaking. Today, the proton synchrotron is still in operation. Not as the main accelerator, but as a supplier of particles to the LHC. This reaches a beam energy of 7,000 GeV, i.e. about 11,000 times more powerful than the first CERN accelerator. With higher collision energies the formation of particles with large masses becomes possible according to Einstein's famous equation $E = mc^2$. That is why, every time, an increase of collision energy marks an exciting new step in physics research. Measurements are then about to show what nature has in store for us. On several occasions nature proved to be much richer than our imagination.

Not only accelerator technologies have taken a giant leap forward at CERN. New detection principles have been designed, tested and implemented at CERN experiments. One famous example is the development of the multiwire proportional chamber by Georges Charpak in 1968. This was the first detector that could make use of computers and achieve a counting rate a thousand times higher than before. Today at the LHC, detectors are needed that can cope with collision frequencies up to 40 MHz. A huge challenge with currently available technologies, let alone with the detector technologies available at the time of planning the LHC, some 25 years ago.

1.3.2 The LHC

The LHC is a circular accelerator with a circumference of about 27 km, located 100 m below the ground close to Geneva, Switzerland. It accelerates proton beams in opposite directions and collides them at four dedicated points along the accelerator ring.

Before reaching the LHC ring, the proton beams are formed and accelerated in several other rings as shown in Figure 1.3. Proton beams enter the LHC ring with an energy of 450 GeV and are currently accelerated up to 3,500 GeV (or 3.5 TeV) per beam. Acceleration in the LHC is performed with electric fields within radiofrequency cavities.

To keep the proton beams in a circular path the beams are located within strong superconducting magnets. The strength of these magnets is what limits the achievable acceleration and thus the maximal collision energy. With equal *bending power* an even larger circular accelerator would be needed to reach higher energies.

[4] Although the current twenty member states are still all European.

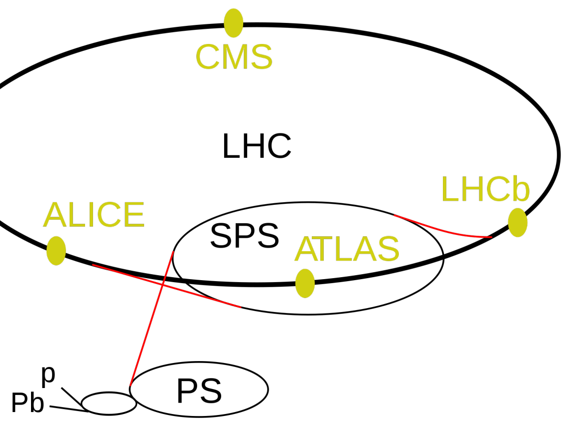

Figure 1.3: Schematic overview of the LHC (pre-)accelerator and the four experiments.

The design collision energy of 14 TeV will not be reached before 2013. With the current collision energy of 7 TeV the LHC reaches more than 3.5 times higher energies than the former record holding collider, the Tevatron at Fermilab, near Chicago. At 7 TeV a search for the Higgs boson can be performed over a large mass range from 100 to 1,000 GeV.

The LHC experiments have been fully commissioned and are taking 7 TeV collision data since March 2010. In this thesis we will discuss results from the ATLAS detector, one of the four experiments located around the LHC ring.

1.4 The ATLAS detector

The ATLAS detector is a so-called general purpose detector. It aims at the detection of a wide variety of physics processes that can occur after a proton-proton collision. ATLAS is a cylindrical detector, 45 m long and 25 m high, with a layered structure. Each layer is designed to detect a particular class of particles. This thesis focuses on the outer detection layer of ATLAS where only *muons*[5] are expected to be detected: the Muon Spectrometer. Other particles are either stopped in the inner layers, e.g. electrons, or are intrinsically undetectable for ATLAS, e.g. neutrinos.

1.4.1 The ATLAS Muon Spectrometer

The ATLAS Muon Spectrometer is designed to efficiently detect muons from collisions and accurately measure their position, direction and momentum. *Tracking* chambers provide precision measurements. *Trigger* chambers provide muon trigger information, making it possible to select collisions with at least one muon in their decay products.

[5] Muons are like electrons but with higher mass. More on this in Chapter 2.

The Muon Spectrometer plays an important role in searches for the Higgs boson. The Higgs boson is an unstable particle that will decay shortly after being produced. One of the possible Higgs decays is to two Z bosons. Each Z boson can subsequently decay to two muons, resulting in a final state with four muons. Efficient and accurate muon measurements are vital for this analysis.

1.5 Particle physics: why?

We discussed developments in accelerators and detectors that seem to be of use restricted to particle physics experiments, far from everyday life. This is far from being true. For example, particle detection techniques developed in experiments (such as) at CERN are applied for medical purposes all around the world. In its search for a global communication platform Sir Tim Berners-Lee and Robert Cailliau from CERN created the World Wide Web, something that seems indispensable in our everyday life. Many other examples can be listed, but the pattern is more important: through the development and construction of technologies applied in fundamental research (usually) unforeseen applications make their way to ordinary life. It is as physicist Victor Weisskopf said:

> *"The problems at the frontier of science are exactly those that can not be solved with established methods".*

The implications of current day Higgs searches for everyday life can not be predicted, but nevertheless should not be underestimated. Experiences from the past teach us that truly groundbreaking science is worth the effort that society puts into it. However, at the moment of performing the research the emphasis should not be on the (short-term) benefits for society. Instead, the driving force and motivation to solve the puzzles on the frontier of science is curiosity. That is what puts the *fun* in fundamental research.

1.6 Thesis overview

The theory relevant for the scope of this thesis contains production and decay mechanisms for the Z and Higgs bosons. This will be the topic of the next chapter. The detector technologies of ATLAS are discussed in detail in Chapter 3, with emphasis on the Muon Spectrometer. A search for the Higgs boson in a four muon final state will be presented in Chapter 7. The effectiveness of this search depends on a good understanding of the performance of the Muon Spectrometer. We have first studied this performance with cosmic-ray data, before proton-proton collision data were available. Results for these cosmic-ray studies are presented in Chapter 4. When collision data became available the performance studies were continued with these data. Di-muon signatures from Z boson decays were used to study the efficiency and momentum resolution of the Muon Spectrometer. These results are discussed in Chapter 5. In addition to the Higgs search and the muon performance studies Chapter 6 shows results for di-muon analyses in heavy-ion collisions.

Chapter 2

Production and decay of the Z and Higgs boson at hadron colliders

In this chapter we will cover the production and decay of the well known Z boson and the predicted Standard Model Higgs boson at hadron collider experiments. First the elementary particles and forces in the Standard Model are introduced in Section 2.1. The weak force and one of its carriers, the Z boson, will be addressed in more detail in Section 2.1.1. After that, Section 2.2 introduces the mechanism of electroweak symmetry breaking, a necessary ingredient in incorporating particle masses into the Standard Model. This mechanism also predicts the existence of the Higgs boson.

The production of the Z boson and its decay channels are covered in Section 2.3, where we also derive an expression for the cross section for $pp \to q\bar{q} \to \gamma^*/Z \to \mu^-\mu^+$. This is the principal result that is used in the muon momentum resolution studies of Section 5.3. The simulation of production and decay of Z bosons in ATLAS is discussed in Section 2.4. In Section 2.5 we turn our attention to the production and decay of the Standard Model Higgs boson at hadron colliders. We also briefly discuss the simulation of the dominant production mechanism of the Higgs at the LHC in that section.

2.1 Elementary particles and forces in the Standard Model

The current understanding of elementary particles and forces is described within a theoretical framework called the Standard Model [5–7]. The Standard Model was developed by numerous physicists from the early 1960s onwards and has been extremely successful in describing and predicting the elementary particles and their interactions.

The Standard Model describes particle interactions as a result of local gauge symmetries [8]. It incorporates three of the four known fundamental forces: the electromagnetic force, the strong force and the weak force. Gravity is too weak at the scales with which particle physics is concerned and is not incorporated in the Standard Model. Figure 2.1 shows a schematic overview of the Standard Model particles and interactions. We will discuss the particles and their interactions in more detail below.

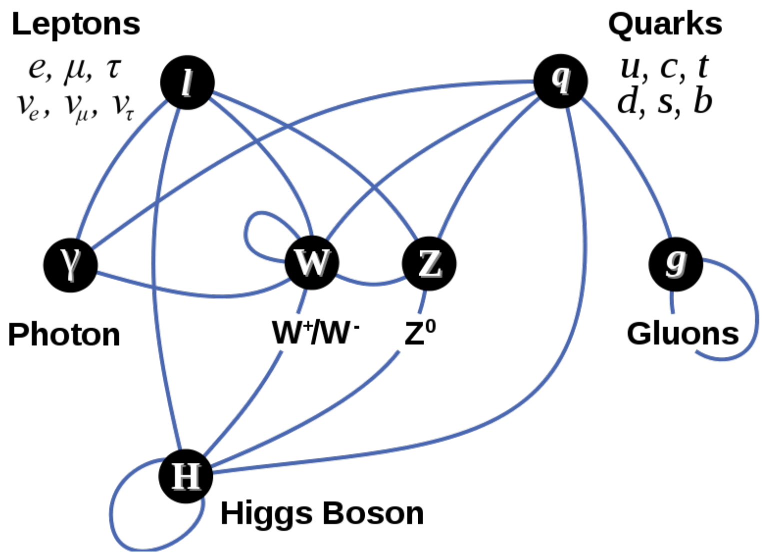

Figure 2.1: Elementary particle couplings are represented by lines.

Force particles

Each of the fundamental forces is mediated by a fundamental particle: the hypothetical graviton for gravity, the photon for electromagnetism, the gluon for the strong force and the $W^{\pm}$ and Z bosons for the weak force. A particle experiences a force if it couples to the respective force mediator, or force carrier. All force carrier particles are *bosons*, i.e. particles with integer spin.

Matter particles

The elementary building blocks of ordinary matter are leptons and quarks. These are classified as *fermions*, particles with half integer spin. The quantum properties of a fermion determine with which force(s) it interacts: fermions with electric charge interact electromagnetically, with color charge strongly and with weak isospin weakly.

Leptons are fermions that interact through the weak force. The electron is a *charged* lepton that therefore interacts both through the electromagnetic and the weak force.

Protons and neutrons are examples of composite particles, each containing three quarks. Particles consisting of quarks are called hadrons, which explains the naming of the Large Hadron Collider (LHC), a proton-proton collider.

All fermions can be divided in three so-called generations of families, as illustrated in Figure 2.2. A particle from a higher generation has the same quantum numbers as the related particle from a lower generation and differs only in mass. For example, the up-, charm- and top-quark have identical quantum numbers but the up- and top-quark differ about five orders of magnitude in mass.

All particles and interactions can be described by imposing local gauge invariance on the Standard Model Lagrangian. In the Standard Model the electromagnetic and the weak force are unified in one *electroweak* description. However, this description leaves the particles massless, something that conflicts with experimental data. In 1964 several papers were written to address this issue [9–11]. A mechanism of *electroweak symmetry breaking* was proposed, now commonly known as the Higgs mechanism[1]. This mechanism introduces a new field, the Higgs field, and predicts the existence of a new particle, the Higgs boson. Elementary particles acquire mass by interactions with the Higgs field. The search for the Higgs boson is a major motivation for building the LHC. The mechanism of electroweak symmetry breaking is discussed in Section 2.2. For a more thorough review of the Higgs mechanism the reader is referred to refs. [5–7].

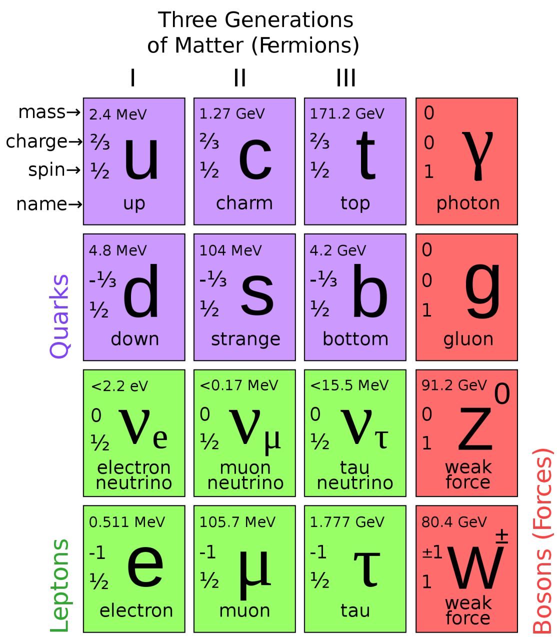

Figure 2.2: The particles of the Standard Model.

2.1.1 A closer look at the weak force

Force carriers

Weak interactions are mediated by $W^{\pm}$ and Z gauge bosons. Weak interactions involving a $W^{\pm}$ boson are referred to as charged weak interactions. Neutral weak interactions involve a Z boson. The Z boson couples to particles with weak isospin.

[1]It is also known as the Englert-Brout-Higgs-Guralnik-Hagen-Kibble mechanism, to mention all major contributors.

Both the $W^{\pm}$ and Z bosons are massive particles, limiting the weak interactions to short ranges. They have first been observed by the UA1 and UA2 experiments at the CERN SPS [12–14]. The mass of the Z has been measured at e^+e^- experiments at LEP and at the Stanford Linear Collider (SLC) to be 91.1876 ± 0.0021 GeV with a full width of 2.4952 ± 0.0023 GeV [15]. It decays shortly after being produced.

QED as an example for the theory of weak interactions

The theory of weak interactions was first modeled on a very successful other theory in particle physics: quantum electrodynamics (QED). QED is the quantum field theory of relativistic electrodynamics. It is the first theory in which full agreement between special relativity and quantum mechanics was obtained. Because of the success of QED it served as an example for the construction of the theory of weak interactions. Calculating probabilities for a process to occur in QED was simplified by the introduction of the Feynman rules. An introduction to these rules is beyond the scope of this thesis, but we will briefly mention the steps involved.

First the physics process is represented in a Feynman diagram, such as Figure 2.3. Two incoming particles, or Dirac fields ψ_A and ψ_B, annihilate to a new particle, the *propagator*, which subsequently decays to two particles[2]. Every vertex is assigned a factor $ig_e\gamma^\mu$, where γ^μ represents the Dirac matrices and g_e represents the coupling strength. A massless propagator is assigned a factor $ig_{\mu\nu}/q^2$, where in this case q^2 is the sum of the two incoming four-momenta.

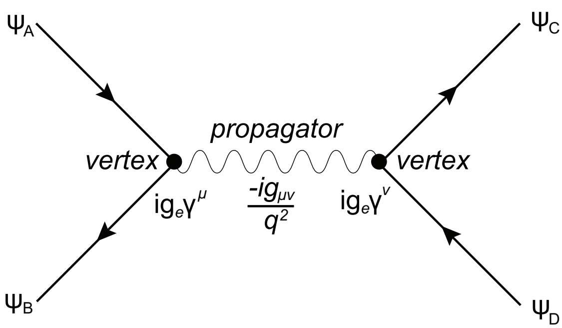

Figure 2.3: An example of a Feynman diagram.

The probability for the process to occur is proportional to the square of the matrix element, $\mathcal{M}$. This matrix element is calculated with Equation 2.1 using the incoming and outgoing particles and the assigned factors in the Feynman diagram[3].

[2]An example of such a process is e^+e^- annihilation into a photon, which subsequently decays to an e^+e^- pair. This process is also known as Bhabha scattering.

[3]This is a simplified example. Actually, matrix elements for *all* possible Feynman diagrams (i.e. with the same incoming and outgoing particles) need to be summed before taking the square.

$$\begin{aligned} i\mathcal{M} &= [\bar{\psi}_B i g_e \gamma^\mu \psi_A] \frac{i g_{\mu\nu}}{q^2} [\bar{\psi}_C i g_e \gamma^\nu \psi_D] \\ &= \frac{-i g_e^2}{q^2}\, g_{\mu\nu}\, [\bar{\psi}_B \gamma^\mu \psi_A][\bar{\psi}_C \gamma^\nu \psi_D]. \end{aligned} \tag{2.1}$$

In QED, the expression for the matrix element contains terms of the form $\bar{\psi}\gamma^\mu\psi$. Similar calculation rules have been applied on weak interaction processes, but experiments revealed a remarkable difference which required a different underlying theory.

V-A structure of weak interactions

It turns out *from experiment* that weak interactions are parity violating, i.e. the weak force couples differently to particles with left-handed chirality than to particles with right-handed chirality. This feature is not understood fundamentally but follows from various measurements dating back to 1957 [16, 17]. Mathematically, a Dirac field ψ can be projected into its left-handed and right-handed components using the γ^5 matrix[4] as

$$\psi_L = \frac{1}{2}(1-\gamma^5)\psi, \tag{2.2}$$

$$\psi_R = \frac{1}{2}(1+\gamma^5)\psi, \tag{2.3}$$

where ψ_L and ψ_R denote the left-handed and right-handed component, respectively. In the ultra-relativistic limit chirality is equal to helicity, which is more easily interpreted: a particle with left-handed helicity has its spin in opposite direction of its momentum[5].

The first description of charged weak interactions, i.e. processes involving $W^\pm$, used terms with $\bar{\psi}\gamma^\mu\psi$ in its matrix element calculations. This pure *vector* description turned out to be wrong. New terms of the form $\bar{\psi}\gamma^\mu\frac{1}{2}(1-\gamma^5)\psi$ were required, showing equally strong vector (γ^μ) and *axial-vector* ($\gamma^\mu\gamma^5$) components. This is referred to as the V-A structure of weak interactions. Comparing this V-A structure to Equation 2.2 shows that the W boson only couples to the left-handed component of ψ.

For charged weak interactions the vector and axial-vector components are equally strong. For neutral weak interactions, i.e. processes involving Z, this is not the case and we have $\gamma^\mu\frac{1}{2}(c_V^f - c_A^f\gamma^5)$ where c_V and c_A are the vector and axial-vector coupling respectively. These couplings are defined as

$$c_V^f = T_f^3 - 2Q_f \sin^2\theta_W, \tag{2.4}$$

$$c_A^f = T_f^3, \tag{2.5}$$

where T_f^3 is the third component of the weak isospin and Q_f is the electric charge of the fermion. The angle θ_W is the weak mixing angle. This angle is related to the masses of the weak gauge bosons via $\cos\theta_W = M_W/M_Z$. Table 2.1 shows values for Q_f, $T_f^3 (= c_A^f)$ and c_V^f for different fermions f.

[4] Using Dirac matrices γ^μ and with $\gamma^5 \equiv i\gamma^0\gamma^1\gamma^2\gamma^3$.

[5] The first experiment indicating parity violation used the decay of polarized cobalt nuclei and showed a clear preference for electrons to be emitted in a direction opposite to that of the nuclear spin.

f	Q_f	$T_f^3(=c_A^f)$	c_V^f
ν_e, ν_μ, ν_τ	0	$\frac{1}{2}$	$\frac{1}{2}$
e^-, μ^-, τ^-	-1	$-\frac{1}{2}$	≈ -0.04
u, c, t	$\frac{2}{3}$	$\frac{1}{2}$	$\approx \ 0.19$
d, s, b	$-\frac{1}{3}$	$-\frac{1}{2}$	≈ -0.35

Table 2.1: Values for Q_f, $T_3^f = c_A^f$ and c_V^f for different fermions.

The quantum properties T_f^3 and Q_f are of importance for Z decays. The Z boson is an unstable particle and will decay shortly after being produced. The decay rate for a Z decaying into a fermion anti-fermion pair can be calculated from the quantum properties of the involved fermions. The third component of the weak isospin and the charge of the particular fermion determine the Z decay rate via

$$\Gamma(Z \to f\bar{f}) = N_C \frac{\sqrt{2} G_F M_Z^3}{6\pi} \cdot \left[(T_f^3 - Q_f \sin^2\theta_W)^2 + (Q_f \sin\theta_W)^2 \right], \tag{2.6}$$

where G_F is the Fermi coupling constant and N_C is the number of colors [15]. For $q\bar{q}$ final states $N_C = 3$, otherwise $N_C = 1$.

2.2 Electroweak symmetry breaking

The Standard Model describes the strong and electroweak interactions by an $SU(3)_C \times SU(2)_L \times U(1)_Y$ gauge symmetry. The $SU(3)_C$ gauge symmetry describes the strong interactions and will not be discussed in this thesis. The gauge symmetry $SU(2)_L \times U(1)_Y$ is the unified electroweak description of the weak force and electromagnetism. The Standard Model Lagrangian for the electroweak interactions is invariant under *local* gauge transformations[6]. Requiring a local symmetry results in four[7] gauge fields ($W_{1,2,3}$ and B) and four gauge bosons ($W^\pm$, Z and γ) plus interaction terms. Another consequence of this invariance is that the gauge bosons are required to be massless. For the electromagnetic part of the theory this is not a problem as the photon is indeed massless. However, the limited range of the weak interaction clearly indicates that the W and Z bosons are massive and that the theoretical description is incomplete.

One solution is to add mass terms for the gauge bosons in the Lagrangian by hand. For the W bosons, the Z boson and the photon one expects mass terms of the form $-M_W^2(W_\mu)^2$, $-\frac{1}{2}M_Z^2 B_\mu^2$ and $-\frac{1}{2}M_\gamma^2 A_\mu^2$ respectively. These terms are not gauge invariant and make the theory non-renormalizable. This is clearly not a successful approach.

[6] This is highly non-trivial. In fact, it is because it *happens* to describe the observed interactions that this local gauge invariance requirement keeps on being used.

[7] $SU(2)$ gives $2^2 - 1 = 3$ gauge fields, $U(1)$ the other $1^2 = 1$.

Higgs mechanism

A solution to this problem was provided by Peter Higgs in 1964 [10] and is known as the Higgs mechanism. It introduces two complex fields in an isospin doublet ϕ and adds a term, $\mathcal{L}_{\text{scalar}}$, to the Standard Model Lagrangian for these fields.

$$\mathcal{L}_{\text{scalar}} = (D^\mu\phi)^\dagger(D_\mu\phi) - \underbrace{\left(\mu^2\phi^\dagger\phi + \lambda(\phi^\dagger\phi)^2\right)}_{V(\phi)}, \tag{2.7}$$

where the isospin doublet has the form

$$\phi = \begin{pmatrix} \phi^+ \\ \phi^0 \end{pmatrix} = \frac{1}{\sqrt{2}} \begin{pmatrix} \phi_1 + i\phi_2 \\ \phi_3 + i\phi_4 \end{pmatrix}. \tag{2.8}$$

The covariant derivative D_μ contains the weak hypercharge Y and the $SU(2)_L$ and $U(1)_Y$ gauge couplings g and g'.

$$D_\mu = \partial_\mu + ig\frac{1}{2}\vec{\tau} \cdot \vec{W}_\mu + ig^{'}YB_\mu, \tag{2.9}$$

where $\vec{\tau}$, $\vec{W}_\mu$ and B_μ represent the Pauli matrices, the $SU(2)_L$ gauge fields and the $U(1)_Y$ gauge fields respectively. A detailed discussion about the Higgs mechanism is beyond the scope of this thesis. However, it is instructive to know why this mechanism is referred to as electroweak symmetry breaking.

For simplicity, imagine a classical scalar field ϕ with a potential given by

$$V(\phi) = \frac{1}{2}\mu^2\phi^2 + \frac{1}{4}\lambda\phi^4, \tag{2.10}$$

where $\lambda > 0$. The corresponding terms for this field ϕ in the Lagrangian are

$$\mathcal{L}_\phi = \underbrace{\frac{1}{2}(\partial_\mu\phi)^2 - \frac{1}{2}\mu^2\phi^2}_{\text{particle, mass}=\mu} - \underbrace{\frac{1}{4}\lambda\phi^4}_{\text{self}-\text{interactions}} . \tag{2.11}$$

Equation 2.11 is symmetric in ϕ and describes a particle with mass μ. By choosing $\mu^2 < 0$ we see that the particle mass is *imaginary*. However, we need to evaluate the perturbations around the minimum of the potential, which is at $v = \pm\sqrt{\mu/\lambda}$. If we now introduce a quantum field h which is centered at the vacuum, i.e. $h = \phi - v$, we can rewrite the Lagrangian in terms of h as

$$\mathcal{L}_h = \underbrace{\frac{1}{2}(\partial_\mu h)(\partial^\mu h) - \lambda v^2 h^2}_{\text{particle, mass}=\sqrt{2\lambda v^2}} - \underbrace{\lambda v h^3 - \frac{1}{4}\lambda h^4}_{\text{self}-\text{interactions}} - \underbrace{\frac{1}{4}\lambda v^4}_{\text{constant}} . \tag{2.12}$$

A *positive* mass term, $m_h = \sqrt{2\lambda v^2}$, appears for the corresponding particle, i.e. the Higgs boson. The Lagrangian is still symmetric in the field ϕ but the vacuum is no longer symmetric in the field h. This is referred to as spontaneous symmetry breaking.

2

Mass of the gauge bosons

We return to the problem of *massless* gauge bosons, resulting from the requirement of local gauge invariance. Equation 2.7 gives the term that is added to the Standard Model Lagrangian by the Higgs mechanism. The choice of potential results in the symmetry breaking, as was shown before. We will now focus our discussion on the kinetic term, $(D^\mu\phi)^\dagger(D_\mu\phi)$, which will give rise to the mass of the gauge bosons.

The isospin doublet that breaks $SU(2)_L \times U(1)_Y$ but leaves $U(1)_Q$ invariant, and thus the photon massless, is

$$\phi_0 = \frac{1}{\sqrt{2}} \begin{pmatrix} 0 \\ v+h \end{pmatrix}, \tag{2.13}$$

which corresponds to Equation 2.8 for $\phi_1 = \phi_2 = \phi_4 = 0$ and $\phi_3 = v + h$.

Using Equations 2.9 and 2.13 to calculate $(D^\mu\phi)^\dagger(D_\mu\phi)$ results in terms proportional to v^2, vh and h^2. Here we will only discuss the terms $\propto v^2$ because these give rise to the masses of the gauge bosons. Neglecting other terms and recognizing $Y_{\phi_0} = 1$ we have

$$(D^\mu\phi_0)^\dagger(D_\mu\phi_0) = \frac{1}{8}v^2\left[g^2(W_1^2 + W_2^2) + (-gW_3 + g'B_\mu)^2\right] + \mathcal{O}(vh) + \mathcal{O}(h^2). \tag{2.14}$$

No mass terms can be identified in this equation. In fact, the gauge fields W_1 and W_2 mix to form well defined masses, i.e. the W^+ and W^- bosons observed in experiments: $W^\pm = \frac{1}{\sqrt{2}}(W_1 \mp iW_2)$. Similarly the gauge fields W_3 and B_μ mix to form the Z boson, $Z_\mu = \frac{1}{\sqrt{g^2+g'^2}}(gW_3 - g'B_\mu)$, and the photon $A_\mu = \frac{1}{\sqrt{g^2+g'^2}}(g'W_3 + gB_\mu)$. Inserting this in Equation 2.14 gives

$$(D^\mu\phi_0)^\dagger(D_\mu\phi_0) = \frac{1}{8}v^2\left[2g^2W^+W^- + (g^2 + g'^2)Z_\mu^2 + 0 \cdot A_\mu^2\right]. \tag{2.15}$$

From this equation, the mass terms can immediately[8] be identified as $M_{W^\pm} = \frac{1}{2}vg$, $M_Z = \frac{1}{2}v\sqrt{g^2 + g'^2}$ and $M_\gamma = 0$. Exactly the result that Higgs and others were trying to achieve: three massive gauge bosons and one massless gauge boson for the electroweak symmetry group.

While the terms proportional to vh and h^2 can be neglected for the discussion on gauge boson masses, they are important terms for other reasons. These terms describe the interactions between the gauge bosons and the Higgs field. The gauge fields enter quadratically, indicating a three-point interaction and four-point interaction of the Higgs to two gauge bosons for terms with vh and h^2, respectively. One example of a three-point interaction is $H \to ZZ$. This is exactly the interaction that motivates our search for a Standard Model Higgs in a four muon final state with two intermediate Z bosons (cf. Chapter 7). The strength of the coupling, and thereby the decay rate, is determined by the mass of the Higgs boson and the mass of the gauge boson. The mass of the Higgs boson is unknown, but once it is known the predicted coupling strengths can be tested.

[8] Note that $W^+W^- = \frac{1}{2}\left(W_1^2 + W_2^2\right)$.

Mass of the fermions

The fermion mass terms can not be added by hand in the Standard Model Lagrangian. Like was the case for the gauge bosons, these mass terms of the form $-m_f\bar{\psi}\psi$ would not be local gauge invariant. This can be seen by expanding ψ into its left-handed and right-handed components as

$$\begin{aligned} -m_f\bar{\psi}\psi &= -m_f(\overline{\psi_R}+\overline{\psi_L})(\psi_R+\psi_R) \\ &= -m_f(\overline{\psi_R}\psi_L+\overline{\psi_L}\psi_R), \end{aligned} \tag{2.16}$$

where we use $\overline{\psi_R}\psi_R = \overline{\psi_L}\psi_L = 0$. The left-handed doublet and the right-handed singlet transform differently under $SU(2)_L \times U(1)_Y$ and therefore Equation 2.16 is not gauge invariant under local $SU(2)_L \times U(1)_Y$ transformations.

However, by using the Higgs field (ϕ) that we introduced before, we can construct a Yukawa interaction term that does remain gauge invariant under local $SU(2)_L \times U(1)_Y$ transformations.

$$\lambda_f(\overline{\psi_R}\phi^\dagger\psi_L+\overline{\psi_L}\phi\psi_R), \tag{2.17}$$

where λ_f is the Yukawa coupling. Taking the electron as an example we can work out the resulting electron term for the Lagrangian from Equation 2.17.

$$\begin{aligned} \mathcal{L}_e &= -\lambda_e\left[\overline{e_R}\phi^\dagger e_L+\overline{e_L}\phi e_R\right] \\ &= -\lambda_e\frac{(v+h)}{\sqrt{2}}(\overline{e_R}e_L+\overline{e_L}e_R) \\ &= -\lambda_e\frac{(v+h)}{\sqrt{2}}\bar{e}e \\ &= -\frac{\lambda_e v}{\sqrt{2}}\,\bar{e}e-\frac{\lambda_e}{\sqrt{2}}\,h\,\bar{e}e. \end{aligned} \tag{2.18}$$

The first term in Equation 2.18 gives the electron mass, $m_e = \lambda_e v/\sqrt{2}$. The second term describes the electron-Higgs interaction. As was the case for the gauge bosons, this interaction is proportional to the electron mass, since $\lambda_e/\sqrt{2} = m_e/v$.

Mass of the Higgs boson

An expression for the mass of the Higgs boson followed from our discussion above and is given by $m_h = \sqrt{2\lambda v^2}$. From muon decay experiments it is derived that $v \approx 246$ GeV [15]. Since the Higgs self-coupling λ is a free parameter, the mass of the Higgs boson is not predicted in the Standard Model. Direct searches at LEP and Tevatron exclude, at 95% confidence level, a Standard Model Higgs boson with a mass of $M_H < 114.4$ GeV and $156 < M_H < 177$ GeV, respectively [18, 19].

In addition to experimental limits, there are also theoretical bounds on the Higgs mass. A detailed discussion about the argumentation behind these bounds is beyond the scope of this thesis, but we will briefly mention some arguments.

The Standard Model Higgs boson plays an important role in the cancellation of high-energy divergences in the amplitude for elastic scattering processes of longitudinally polarized massive gauge bosons. Due to this cancellation of divergences the theory remains unitary and renormalizable. Requiring perturbation theory to remain valid puts an upper bound on the Higgs mass of about 700 GeV[9].

The self-coupling, λ, is not a constant but depends on the energy scale, Q^2. The evolution function, $\beta_\lambda \equiv d\lambda/d(\ln Q^2)$, can be evaluated at very large and very small values of λ, i.e. $\lambda \gg g, g'$and h_t[10] or $\lambda \ll g, g'$and h_t. For $\lambda \gg g, g'$and h_t there is some cut-off scale Λ_1 at which $\lambda(\Lambda_1)$ becomes infinite. This so-called Landau pole defines an upper bound on the Higgs mass.

For $\lambda \ll g, g'$and h_t there is some cut-off scale Λ_2 at which $\lambda(\Lambda_2)$ becomes negative. The requirement of a positive value for λ is referred to as vacuum stability and provides a lower bound on the Higgs mass. Figure 2.4 shows the upper and lower bounds as a function of the energy scale Λ. The allowed region derived from the running of the self-coupling is indicated in the figure.

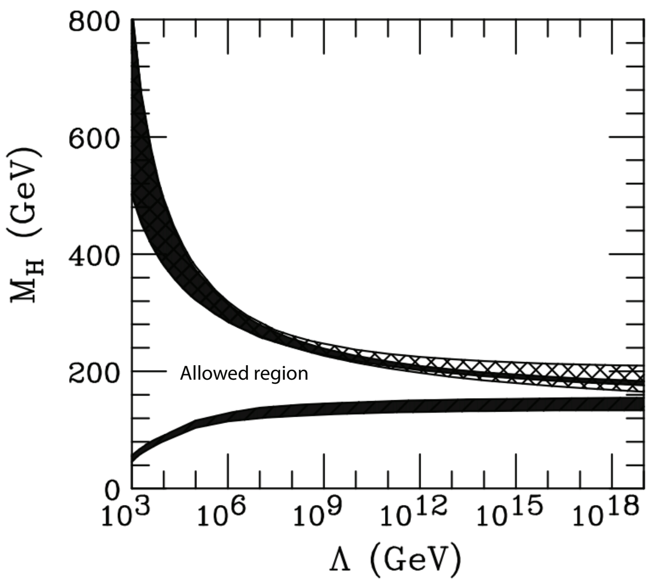

Figure 2.4: Theoretical limits on the Standard Model Higgs boson mass, derived from the running of the self-coupling. A top quark mass of 175 GeV is assumed [20].

[9] A consequence of this is that *if* we don't find the Higgs, or something else that cancels these divergences and fits the Standard Model, *then* the Standard Model must be wrong!

[10] h_t is the top quark Yukawa coupling.

2.3 Production and decay of the Z boson at hadron colliders

The muon performance studies that are presented in Chapter 5 make use of $Z \to \mu^-\mu^+$ events in ATLAS. Before addressing this Z decay channel we look at the production of Z bosons in hadron colliders. Afterwards we discuss the Z decay channels in general, and the $\mu^-\mu^+$ decay channel in particular. Since we will be looking at these *di-muon* final states we cover the di-muon invariant mass distribution. The shape of this distribution is referred to as the di-muon invariant mass *lineshape* and is discussed in some detail.

2.3.1 Production of the Z boson

Many different particles can be produced in hadronic collisions such as at the proton-proton (pp) collisions of the LHC and at the proton-antiproton ($p\bar{p}$) collisions of the Tevatron. The main figures of merit for an accelerator are its center of mass energy, $\sqrt{s}$, and instantaneous luminosity, $\mathcal{L}$. The instantaneous luminosity in a particle collider is a measure for the number of collisions per unit area per second. The number of produced particles per second, N, in a collision is proportional to $\mathcal{L}$ and the particle production cross section, $\sigma(\sqrt{s})$, via

$$N = \mathcal{L}\ \sigma(\sqrt{s}). \tag{2.19}$$

For fixed $\mathcal{L}$ the particle production cross sections can be compared for various values of $\sqrt{s}$. Figure 2.5 shows an example of such a comparison with the expected number of events per second on the right vertical axis [21]. It shows an increase of one order of magnitude in the production of Z bosons going from the Tevatron center of mass energy to the LHC design center of mass energy of 14 TeV.

The Z boson couples weakly to all fermions because all fermions carry weak isospin. In hadron colliders and at leading order the only possible s-channel Feynman diagram for Z production is from quark-antiquark ($q\bar{q}$) annihilation. This annihilation process can also produce a virtual photon γ^*, since quarks couple to the electromagnetic force carrier. Therefore we get two possible Feynman diagrams, which are often shown in one diagram as in Figure 2.6. Drell and Yan were the first to explain this $q\bar{q}$ annihilation process, using the parton model [22].

Whether the $q\bar{q}$ annihilation in Figure 2.6 results in a virtual photon or a Z boson depends on the energy available in the hard scattering process. This in turn depends on the proton momentum fractions, x, carried by the quark and anti-quark. The momentum fractions for quarks and gluons are modeled by parton distribution functions (PDFs). Figure 2.7 shows the distribution function $f(x, Q^2)$ multiplied by x for a proton at two energy scales Q^2. For anti-protons the quarks and anti-quarks in Figure 2.7 are inverted.

At the Tevatron ($p\bar{p}$ collider) the $q\bar{q}$ annihilation mostly occurs between two valence quarks. At the LHC (pp collider) Drell-Yan Z production is only possible with an anti-quark from the *sea quarks*, i.e. quarks from virtual $q\bar{q}$ pairs that arise from gluon splitting. Sea quarks carry on average a lower momentum fraction than the valence quarks (cf. Figure 2.7).

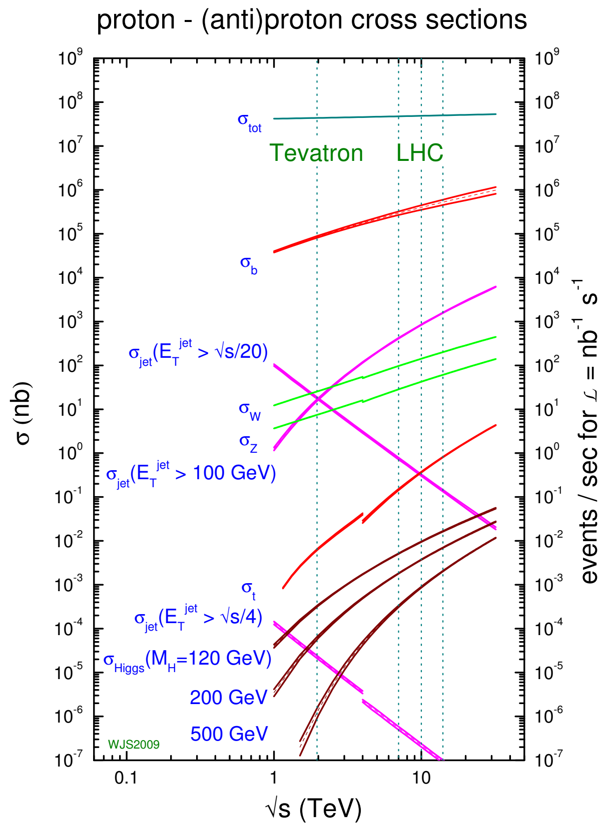

Figure 2.5: Production cross sections as a function of center of mass energy $\sqrt{s}$.

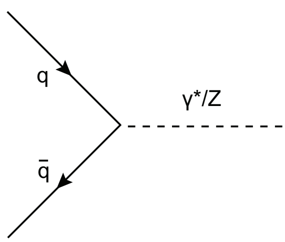

Figure 2.6: Feynman diagram for Drell-Yan production in a hadron collision.

The calculation of the Z production cross section involves a summation over all quarks with sufficient energy to produce a Z. Since at the LHC a sea quark is required, the production cross section would be reduced compared to the Tevatron, for equal $\sqrt{s}$. However, at the center of mass energy of the LHC more sea quarks with sufficient energy to produce a Z are available. This effect dominates by far and causes an increased Z production cross section at the LHC compared to the Tevatron.

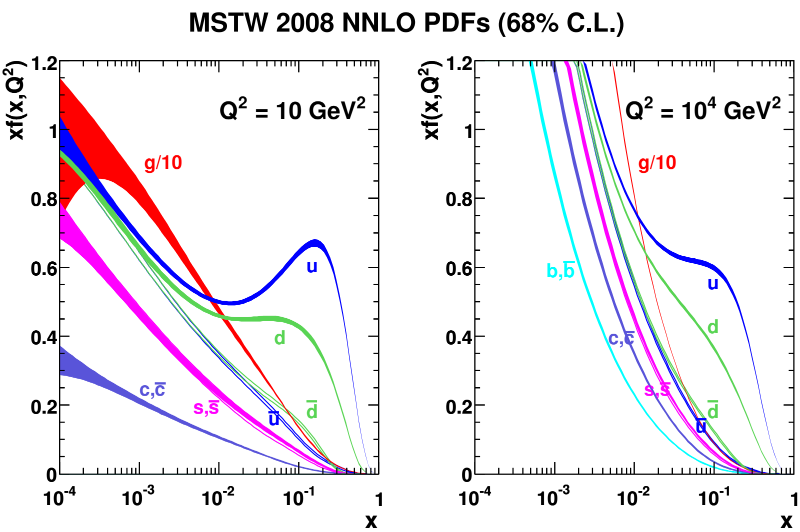

Figure 2.7: NNLO parton distribution functions for a proton [21].

2.3.2 Z decay channels

When studying Z decay channels it is important to remember that the Z boson couples weakly to all fermions, f. Conservation of charge and weak isospin only allows for $Z \to f\bar{f}$ decays to occur, e.g. $Z \to \mu^+\mu^-$. Table 2.2 shows the decay modes of the Z and their respective measured decay widths [15]. The observed differences can be explained by the quantum properties of the fermions, as was shown in Equation 2.6.

Z decay modes	Γ_i/Γ
e^-e^+	$3.363 \pm 0.004\%$
$\mu^-\mu^+$	$3.366 \pm 0.007\%$
$\tau^-\tau^+$	$3.367 \pm 0.008\%$
$\nu\bar{\nu}$	$20.00 \pm 0.06\%$
$q\bar{q}$	$69.91 \pm 0.06\%$

Table 2.2: Z boson decay modes and their relative decay widths.

Although most Z bosons decay into hadrons ($q\bar{q}$) this is not a very clean experimental signature. QCD backgrounds overwhelm the signal from hadronic Z decays. In contrast, the excellent momentum resolution of electrons and muons in ATLAS results in a clear signal from the leptonic Z decays. The implementation of lepton triggers in ATLAS helps in selecting interesting events for this analysis. Requiring isolated electrons and muons reduces the QCD background in these decay channels to a negligible level.

Using the properties of the Z boson, one of the *standard candles* in particle physics, extensive performance studies are possible. For example the di-muon invariant mass spectrum around the mass of the Z boson can be used to study the muon momentum resolution as described in Section 5.3. For this purpose a theoretical description of the expected di-muon invariant mass distribution, or lineshape, is required.

2.3.3 The cross section for $pp \to q\bar{q} \to \gamma^*/Z \to \mu^-\mu^+$

The di-muon invariant mass lineshape is a direct reflection of the production cross section $\sigma(pp \to q\bar{q} \to \gamma^*/Z \to \mu^-\mu^+)$. To obtain the theoretical prediction for this lineshape we follow the Feynman rules. At leading order there are two Feynman diagrams that contribute to this process, shown in Figure 2.8. Therefore we have two matrix elements which have to be summed and then squared, giving us three terms in the production cross section formula: a pure photon term, a pure Z term and an interference term.

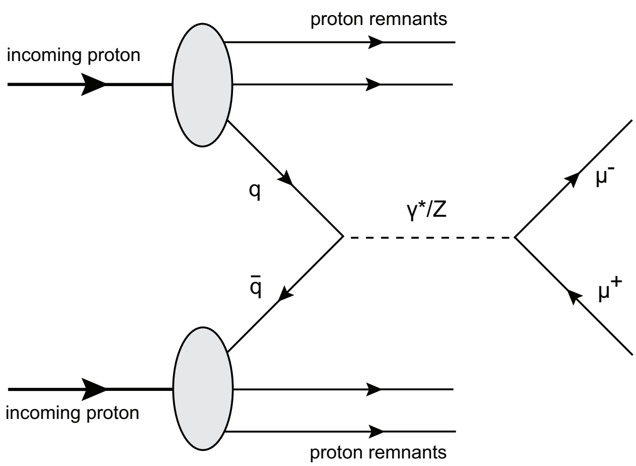

Figure 2.8: Feynman diagram for Drell-Yan production in a proton-proton collision, followed by a decay into two muons.

In reference [7] a detailed overview of the calculation is given. The total cross section σ for producing a lepton pair is obtained by weighting the subprocess cross section $\sigma(q\bar{q} \to l^+l^-)$ with the parton distribution functions $f(x)$ as

$$\sigma = \sum_q \int dx_1 dx_2 f_q(x_1) f_{\bar{q}}(x_2) \sigma(q\bar{q} \to l^+l^-). \tag{2.20}$$

The subprocess cross section depends on the energy available in the hard scatter, $\hat{s}$, and is given by

$$\hat{\sigma}(q\bar{q} \to l^+l^-)(\hat{s}) = \frac{4\pi\alpha^2}{3\hat{s}} \frac{1}{N} \left(Q_q^2 - 2Q_q c_V^l c_V^q \chi_1(\hat{s}) + ({c_A^l}^2 + {c_V^l}^2)({c_A^q}^2 + {c_V^q}^2)\chi_2(\hat{s}) \right), \tag{2.21}$$

where α and N are the electromagnetic coupling and an overall color averaging factor, respectively.

$\chi_1(\hat{s})$ and $\chi_2(\hat{s})$ are defined as

$$\chi_1(\hat{s}) = \kappa \frac{\hat{s}(\hat{s}-M_Z^2)}{(\hat{s}-M_Z^2)^2+\Gamma_Z^2 M_Z^2}, \tag{2.22}$$

$$\chi_2(\hat{s}) = \kappa^2 \frac{\hat{s}^2}{(\hat{s}-M_Z^2)^2+\Gamma_Z^2 M_Z^2}, \tag{2.23}$$

where M_Z and Γ_Z are the mass and full width of the Z boson and $\kappa = \frac{\sqrt{2}G_F M_Z^2}{16\pi\alpha}$ with G_F the Fermi coupling constant. Section 5.3 shows how Equation 2.20 is applied in ATLAS: how the structure functions are modeled by fits to simulation and how detector resolution effects are included.

We see that Equation 2.21 indeed shows three terms:

- a pure photon term ($\propto \frac{1}{\hat{s}}$);
- a pure Z term ($\propto \frac{\hat{s}}{(\hat{s}-M_Z^2)^2+\Gamma_Z^2 M_Z^2}$);
- an interference term ($\propto \frac{\hat{s}-M_Z^2}{(\hat{s}-M_Z^2)^2+\Gamma_Z^2 M_Z^2}$).

To a good approximation $\sqrt{\hat{s}}$ can be taken to be the measured di-muon invariant mass. For $\hat{s} << M_Z^2$ the photon term dominates. For $\hat{s} \approx M_Z^2$ the Z term dominates.

2.4 Simulation of $Z \to \mu^-\mu^+$ in ATLAS

To obtain a good understanding of the production and decay of Z bosons in ATLAS data the observations are compared to simulated samples. The simulation needs to incorporate up-to-date knowledge on production processes and decay channels, but also a detailed description of the detector used in the analysis.

The simulation software is integrated into the ATLAS software framework, `ATHENA` [23], and uses the `Geant4` simulation [24] for its detector description. The simulation is generally divided into three steps:

1) event generation - simulating the collision and its collision products;
2) detector simulation - describing the detector geometry and how the collision products interact with the (in)active detector material;
3) digitization - translating particle-detector interactions into times, amplitudes and electronics signals such as voltages, currents, bits and bytes as they would be measured by the detector in real collisions.

The file formats after step three are identical to the ones after data taking. This allows for a direct comparison between data and simulation by running particle reconstruction algorithms (cf. Section 3.5) on these identical file formats. A more detailed description of the simulation steps can be found in ref. [25]. The different steps involved in event generation are discussed in more detail below.

Event generation

Each collision event, including production and decay of intermediate particles such as the Z boson, can be split up in several stages according to the factorization theorem [26]. The description of a proton-proton collision includes:

- the structure of the incoming protons;
- the hard scattering process;
- parton showering;
- hadronization.

In Section 2.3 we discussed the importance of the structure of the incoming protons in the context of parton distribution functions (PDFs). In the case of Drell-Yan production the available energy in the hard scattering determines whether a virtual photon or a Z boson can be created. The hard scattering is the core process of the hadronic collision and describes the interaction of the incoming partons.

In all stages of the collision process stochastic processes are involved. Monte Carlo (MC) generators are widely used to model this stochastic behavior. Simulation samples in ATLAS are therefore commonly referred to as 'Monte Carlo' samples[11].

Several types of MC generators are used in ATLAS studies. A distinction is made between general purpose event generators that perform the full simulation chain and specialized matrix element generators. For a detailed description of the (differences between) MC generators the reader is referred to refs. [25, 27]. The following generators are most common for $Z \to \mu^-\mu^+$ studies in ATLAS:

- `PYTHIA`: a widely used general purpose event generator capable of performing the full simulation chain. A wide range of hard scattering processes are available at leading order (LO) calculation. For higher order corrections the parton shower approach is used;
- `HERWIG`: a similar, and also widely used, general purpose event generator. `HERWIG` differs from `PYTHIA` in the modeling of the parton showers and the hadronization;
- `MC@NLO`: a matrix element generator including full next-to-leading order (NLO) calculations for QCD processes during the hard scattering process. It includes higher order approximations of the parton shower and can be interfaced with `HERWIG`;
- `ALPGEN`: a matrix element generator that can generate LO matrix elements for up to six additional final state partons. Spin correlations are also taken into account and interfaces to `PYTHIA` and `HERWIG` exist.

[11] One will also hear people mentioning *"Monte Carlo data"*, which I think is wrong and confusing.

Depending on the order of calculation parton showering techniques can be applied in the event generation. Parton showering models are applied for LO calculations. Perturbative corrections from the emission of gluons by the (anti-)quarks[12] are approximated by parton showering models: a gluon splits into a $q\bar{q}$ pair which in turn radiates gluons after which the splitting of the gluons can occur again until a cut-off energy is reached.

Particle decays are modeled using measured and predicted particle masses, lifetimes and branching ratios. The decay of the Z boson is simulated using the decay widths discussed in Section 2.3.2. However, in the configuration of the event generator a choice for a specific decay channel can be made. This effectively selects only the required decay channel to be in the generator output and reduces the computing time needed for the further steps of detector simulation and digitization.

If the decay products contain (anti-)quarks the parton showering can also be applied at that stage. Eventually only *color free* quark composite particles, i.e. hadrons, are allowed in nature. These states should be formed from the produced (anti-)quarks and gluons. This process of hadronization involves non-perturbative processes and cannot be calculated analytically.

2.5 Production and decay of the Higgs boson at the LHC

The mass of the Higgs boson is an unknown parameter in the Standard Model. Depending on its mass, the production cross-section for the Higgs boson varies. The main production mechanism for the Standard Model Higgs at the LHC is via gluon-gluon (gg) fusion. Figure 2.9 shows a leading order Feynman diagram for this process.

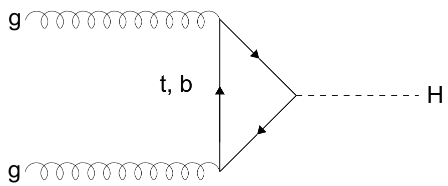

Figure 2.9: Feynman diagram for Higgs production via gluon-gluon fusion.

The second largest production mechanism is via vector boson fusion (VBF). In addition to these two largest mechanisms several *associated* production mechanisms exist in which the Higgs boson is produced in association with other particles. Table 2.3 shows production cross sections at several assumptions for the Higgs mass [28]. Figure 2.10(a) shows the total production cross section and the sub-leading contributions.

The Higgs boson is an unstable particle and will decay shortly after being produced. Many possible decay channels exist for the Standard Model Higgs boson. In this thesis we will focus on the decay channel where the Higgs boson decays into two Z bosons,

[12] The incoming (anti-)quarks can emit photons and/or gluons because of their electromagnetic and color charge, respectively. Gluon emission dominates in hadronic collisions.

which subsequently decay into two muons each. A four muon final state could then be detected in the Muon Spectrometer. Figure 2.10(b) shows the branching ratios for various decay channels of the Higgs boson, including the decay to two Z bosons.

Production	$M_H = 114$ GeV	130 GeV	150 GeV	200 GeV	300 GeV
gg fusion	18	14	10	5	2.4
VBF	1.35	1.15	0.96	0.64	0.30
WH	0.78	0.49	0.30	0.10	0.020
ZH	0.42	0.28	0.17	0.061	0.012
$t\bar{t}$H	0.11	0.077	0.049	0.018	0.0047

Table 2.3: Higgs production cross-sections in pb for various Higgs masses.

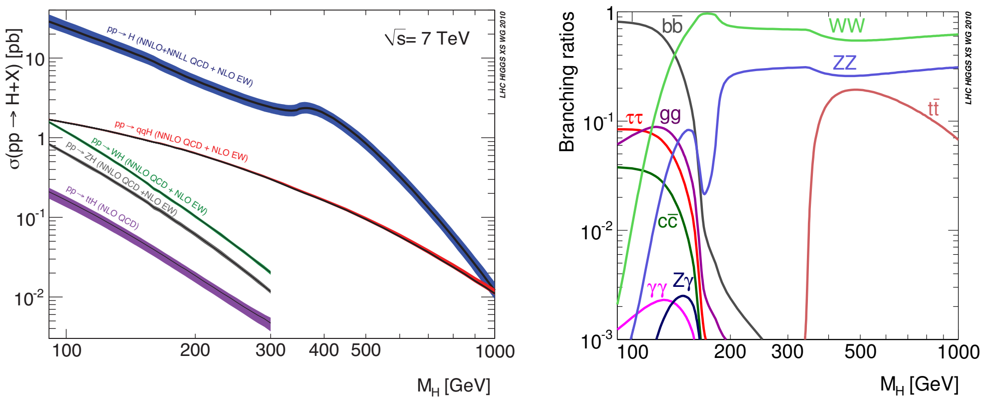

(a) (b)

Figure 2.10: Higgs production cross section and branching ratio at various masses [28].

Simulation of the Higgs boson at the LHC

The simulation of the Higgs production is performed by several event generators. `POWHEG` generates events with next to leading order (NLO) calculations and can be easily interfaced to a shower generator [29]. Within ATLAS `POWHEG` is currently the event generator of preference for studies of signals where the Higgs boson decays to lepton final states. Therefore, our studies of Chapter 7 are performed with samples where `POWHEG` is interfaced to `PYTHIA`. We obtain the shapes of Higgs mass distributions from these simulated samples but scale these according to a recent update of Higgs production cross sections and branching ratios [28]. This will give us the most up to date prediction of the expected number of Higgs bosons in our studies.

Chapter 3

Particle detection in the ATLAS detector

3

3.1 Introduction

The ATLAS detector is a general purpose detector that aims at the detection of a wide range of possible event signatures. This implies an optimized implementation of several particle detection technologies discussed in this chapter. ATLAS has a layered structure in which each layer is aimed at the detection of a specific type of particle. Figure 3.1 is an illustration of the ATLAS detector showing its size and components.

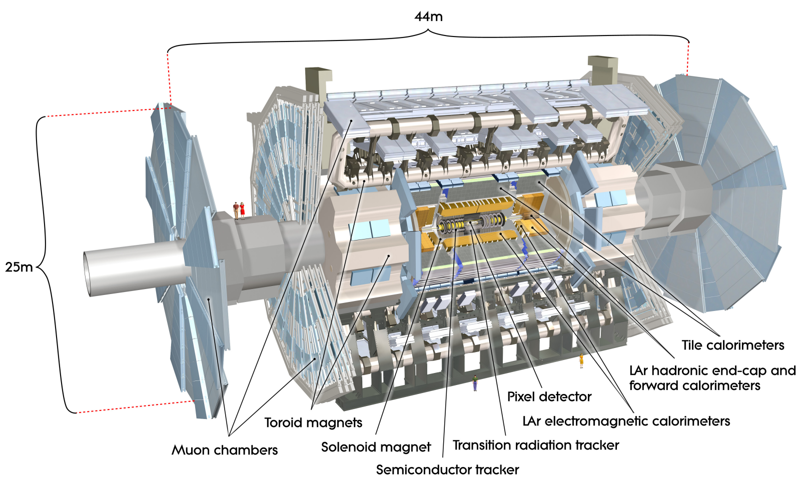

Figure 3.1: Illustration of the ATLAS detector with size and components indicated.

Before discussing the applied detector technologies we will address the ATLAS trigger system in Section 3.2 and the magnet systems in Section 3.3. From the interaction point outwards various detector technologies are applied. They are discussed in Section 3.4 where subsequently the Inner Detector, Calorimeter and Muon Spectrometer are described. A more thorough discussion of the ATLAS sub detector components can be found in [30]. The reconstruction of muon tracks is addressed in Section 3.5. The precision of the Muon Spectrometer is important for many physics studies, including $Z \rightarrow \mu^-\mu^+$ decay studies, and is discussed in Section 3.6.

3.1.1 Coordinate system

The ATLAS experiment uses a right-handed coordinate system with the origin at the nominal proton-proton interaction point. The positive x-axis points towards the center of the LHC ring and the positive y-axis points upwards. The positive z-axis points in the beam direction that forms a right-handed coordinate system. Transverse momentum, p_T, and transverse energy, E_T, are defined in the x-y plane, e.g. $p_T = \sqrt{p_x^2 + p_y^2}$.

Two angles are defined: the azimuthal angle ϕ is measured around the beam axis and the polar angle θ is measured with respect to the beam axis. The polar angle is used to define the pseudorapidity $\eta = -\ln\tan(\theta/2)$. The separation between two reconstructed physics objects is expressed in terms of the azimuthal and polar angular differences as $\Delta R = \sqrt{(\Delta\phi)^2 + (\Delta\eta)^2}$.

3

3.2 Trigger

In a high luminosity environment such as at the LHC, it is important to select interesting events at an early stage and bring down the data flow to a rate that can be handled by offline computing power and storage capacity. The ATLAS trigger system selects interesting events from the design bunch crossing rate of 40 MHz. The data are written to tape with a *design* rate of 200 Hz. In 2010 and 2011 proton-proton (pp) collision data taking this rate was *measured* to be 300 Hz [31,32]. The event rate reduction is achieved in three consecutive stages:

- **Level 1 (L1) -** the first stage is a hardware-based selection using calorimeter and muon trigger detector information to define regions of interest (RoI). The L1 trigger is the fastest trigger (decisions take on average 2.5 μs per event) and reduces the design (measured) rate to about 75 kHz (40 kHz);
- **Level 2 (L2) -** the second stage takes the RoI information provided by the L1 trigger and continues the selection of events by using a finer detector granularity and some tailored (i.e. fast) reconstruction algorithms. These additions make the L2 trigger slower than the first stage (about 40 ms per event). The design (measured) output rate is about 3.5 kHz (4 kHz);
- **Event Filter (EF) -** the last stage of the trigger system uses all available data for events selected by the L2 trigger. The EF uses object reconstruction algorithms as available in offline reconstruction. It is the slowest trigger stage (about 4 s per event) and brings down the design (measured) rate to about 200 Hz (300 Hz).

Each stage of the trigger system allows for selections of low-p_T or high-p_T particles. When the LHC moves from startup settings to higher instantaneous luminosity the low-p_T triggers are prescaled to reduce their output to a manageable rate.

Triggering on events biases the output dataset to events where you *expect* something interesting. Of course, the rest of the dataset could also be containing interesting *unexpected* events. For this reason ATLAS stores, at a rate of 5 Hz, a random sample of events that do not pass trigger requirements.

3.3 Magnet systems

The design of the ATLAS detector was driven by a choice for the magnet systems. The magnet layout consist of one solenoid magnet and three toroid magnets: one in the barrel and one for each of the two endcaps. Figure 3.2 shows an illustration of the magnet layout as implemented in ATLAS.

The solenoid provides a 2 T axial magnetic field for the Inner Detector. It is located before the calorimeter and its layout is optimized to keep the material thickness in front of the calorimeter as low as possible.

The toroid magnets are located after the calorimeter and provide bending power for the Muon Spectrometer. The air-core magnet concept minimizes the amount of material traversed by the muons after exiting the calorimeters. This design however implies a large diameter for the toroid magnet system ($\approx$ 20 m), and thus also for the ATLAS detector[1]. Barrel and endcap toroids each consist of eight coils, indicated in Figure 3.2. They provide a magnetic field of approximately 0.5 T and 1 T for the muon detectors in the barrel and endcap regions, respectively.

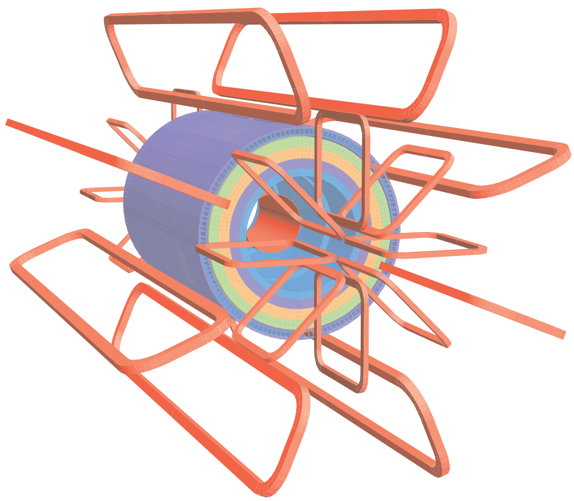

Figure 3.2: Illustration of the magnet layout used in ATLAS.

3.4 Detector technologies

Several detection principles are applied in ATLAS. *Tracking* detectors are used for precision measurements of the particle momentum of charged particles and *calorimeters* are used for precision measurements of the energy of charged and neutral particles. From the interaction point outwards the ATLAS detector can be divided in three components where tracking, calorimetry and again tracking are used:

[1]It is this characteristic design feature that gives ATLAS its name: A *Toroidal* Lhc ApparatuS.

- The Inner Detector measures the position, direction and momentum of charged particles close to the interaction point;
- the electromagnetic (EM) and hadronic calorimeters measure energy deposits of charged and neutral particles, respectively. The calorimeters are situated outside the Inner Detector;
- the Muon Spectrometer measures the position, direction and momentum of muons. It is situated outside the calorimeters.

During the design of ATLAS several performance goals were formulated to achieve the necessary precision for the physics program. Table 3.1 shows the required resolution for the various detector components in ATLAS. Units of p_T and E in this table are GeV.

Detector component	**Required resolution**	η **coverage**
Inner Detector	$\sigma_{p_T}/p_T = 0.05\%\ p_T \bigoplus 1\%$	± 2.5
EM calorimetry	$\sigma_E/E = 10\%/\sqrt{E} \bigoplus 0.7\%$	± 3.2
Hadronic calorimetry		
barrel and endcap	$\sigma_E/E = 50\%/\sqrt{E} \bigoplus 3\%$	± 3.2
forward	$\sigma_E/E = 100\%/\sqrt{E} \bigoplus 10\%$	$3.1 < \lvert\eta\rvert < 4.9$
Muon Spectrometer	$\sigma_{p_T}/p_T = 10\%$ at $p_T = 1$ TeV	± 2.7

Table 3.1: General performance goals for the ATLAS detector [30].

3.4.1 Inner Detector

The Inner Detector (ID) measures the position, direction and momentum of charged particles close to the interaction point. It is the detector closest to the interaction point and has to deal with approximately 1,000 tracks per *pp*-collision [30]. The ID consists of three complementary sub-detectors: a silicon pixel detector, a silicon strip detector and a straw tube detector. The latter is a transition radiation tracker (TRT) and forms the outer part of the ID. The silicon pixel detector (Pixel) is closest to the beampipe and thus has to deal with the highest particle fluxes in ATLAS. The silicon strip detector is a semiconductor tracker (SCT) and is located between Pixel and TRT.

The ID is contained within a concentric cylindrical envelope of length ± 3512 mm and radius 1150 mm. It is immersed in the 2 T solenoidal magnetic field which is aligned to the beam axis. Figure 3.3 shows the Inner Detector components and size.

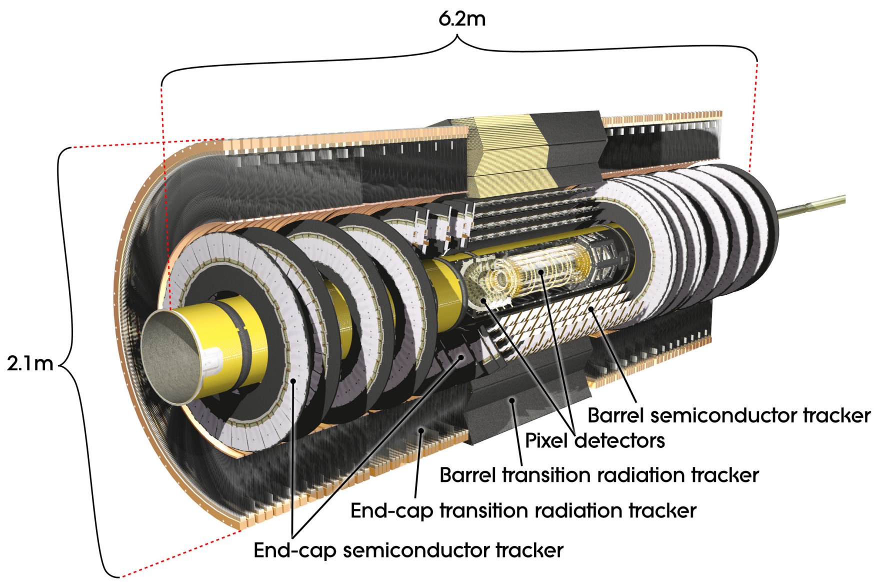

Figure 3.3: Illustration of the Inner Detector with size and components indicated.

3

Pixel

The pixel detector design needed to meet very stringent specifications on radiation hardness, resolution and occupancy in the innermost layers. The layout consists of silicon pixel sensors in three cylindrical layers around the beam pipe and three endcap disks on each side of the interaction point. A pixel sensor has a nominal size of $50 \times 400\ \mu\text{m}^2$ and provides a discrete space-point measurement. There are about 80 million sensors in total in the pixel detector. The hermetic design ensures that at least three pixel hits are generated by charged particles within the acceptance of $|\eta| < 2.5$. The intrinsic measurement accuracy in the barrel (endcap) region is 10 μm in $R - \phi$ and 115 μm in z (115 μm in R), with R the radial distance $\sqrt{x^2 + y^2}$.

SCT

The SCT uses silicon strips that are assembled in modules, with two strips placed at 40 mrad stereo angle between them. Each module provides a two-dimensional measurement in the precision plane, i.e. $R - \phi$ for the barrel and $R - z$ for the endcap. The modules are placed in four concentric cylinders around the beam pipe and one endcap on each side of the interaction point. On both sides, each endcap consists of nine disks of SCT modules. A total of 4088 SCT modules is implemented in ATLAS providing at least four precision measurements within the acceptance of $|\eta| < 2.5$. The intrinsic measurement accuracy is 17 μm and 580 μm for the precision plane and the non-precision coordinate, respectively.

TRT

The TRT is a drift tube detector that has the possibility to measure transition radiation. Its most important design goals are to improve the transverse momentum resolution and to enhance separation between electrons and pions by using emitted transition radiation.

Straw tubes with a diameter of 4 mm are used. They contain a 3 μm tungsten anode wire and a $Xe:CO_2:O_2$ (70:27:3) gas mixture. A passing charged particle ionizes the gas and a signal is read out at the tube ends. The drift radius accuracy of a single straw is 130 μm in $R - \phi$. The drift tube detection principle is also applied in the Muon Drift Chambers and will be adressed in more detail in Section 3.4.3.

The straws are interleaved with polypropylene fibers or foil for barrel and endcap regions, respectively. When a charged particle crosses the boundary between straw tube and fiber/foil it passes between two material layers with different dielectric constants. It can then emit transition radiation with a probability proportional to $\gamma = E/m$. The mass of the pion is more than 250 times larger than the mass of the electron, resulting in a significantly larger γ for electrons. Transition radiation will result in an increase in signal amplitude of about one order of magnitude and is detected by readout voltages passing a high threshold. Figure 3.4 shows the probability for an electron/pion to produce a high-threshold hit in the barrel TRT region as a function of γ.

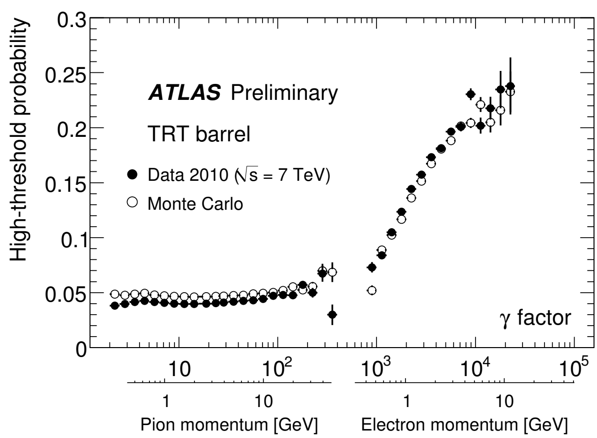

Figure 3.4: Probability of a high-threshold TRT hit as a function of $\gamma = E/m$ [33].

3.4.2 Calorimeter

Calorimeters are used for precision measurements of the energy of charged and neutral particles. In ATLAS both electromagnetic (EM) and hadronic calorimeters are used. EM calorimeters measure electrons and photons through their EM interactions. Hadronic calorimeters measure hadrons through their strong and EM interactions. EM calorimeters form the inner layer of the ATLAS calorimeter. The outer layer contains hadronic calorimeters. Figure 3.5 shows the components of the ATLAS calorimeter.

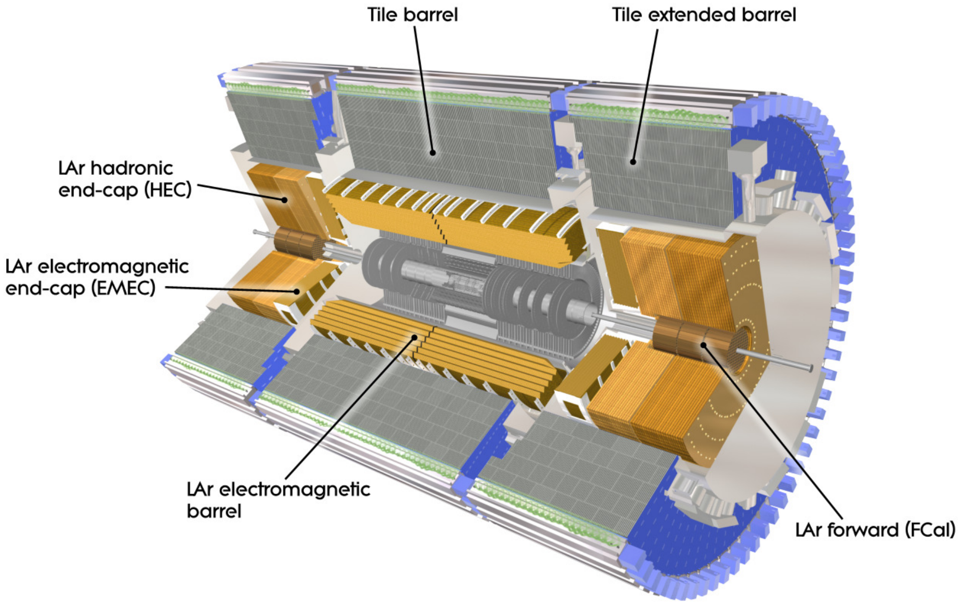

Figure 3.5: Illustration of the ATLAS Calorimeter with components indicated.

3

The ATLAS calorimeters are *sampling* calorimeters, consisting of alternating layers of an absorber material and an active medium. The absorber degrades the energy of the incident particle, the active medium provides the detectable signal. In the *electromagnetic* calorimeters liquid argon and lead are used as the active medium and absorber, respectively. In the electromagnetic part of the forward calorimeter (FCal) liquid-argon and copper are applied.

The *hadronic* calorimeter uses various sampling materials. In the tile calorimeter at $|\eta| < 1.7$ steel and scintillator are used as the absorber and active medium, respectively. The hadronic endcap calorimeter is a copper/liquid-argon sampling calorimeter which covers $1.5 < |\eta| < 3.2$. The hadronic forward calorimeters ($3.1 < |\eta| < 4.9$) use copper and tungsten as absorbers and again liquid-argon as active medium.

The cumulative material at the exit of the electromagnetic calorimeter corresponds to more than 22 and more than 24 radiation lengths, X_0, in the barrel and endcap, respectively. This is enough to stop (almost) all electrons and photons. At the exit of the hadronic calorimeter the cumulative material corresponds to about 11 interaction lenghts, λ. This has been shown to be sufficient to reduce hadron punch-through, e.g. π/K, well below the irreducible level of prompt or decay muons [30]. The good stoppage power, together with the large η coverage, ensures a good measurement of missing energy, E_T^{miss}. Particles that escape the detectors undetected, e.g. neutrinos, will result in net missing transverse energy when summing the contributions from all detected particles.

3.4.3 Muon Spectrometer

The outermost part of the ATLAS detector is the Muon Spectrometer. Tracking chambers measure the position, direction and momentum of muons. Monitored Drift Tube chambers (MDTs) are precision tracking chambers in the barrel and endcap region. In both regions the MDTs are placed in three measurement layers. At large pseudorapidity, $2.0 < |\eta| < 2.7$, Cathode Strip Chambers (CSCs) replace the first layer of MDTs. CSCs are designed to withstand the high counting rates in this η region.

In addition to these precision measurements the spectrometer provides muon trigger information for $\eta < 2.4$. Resistive Plate Chambers (RPCs) and Thin Gap Chambers (TGCs) are used for triggering in the barrel and endcap region, respectively. Figure 3.6 shows the different components of the Muon Spectrometer.

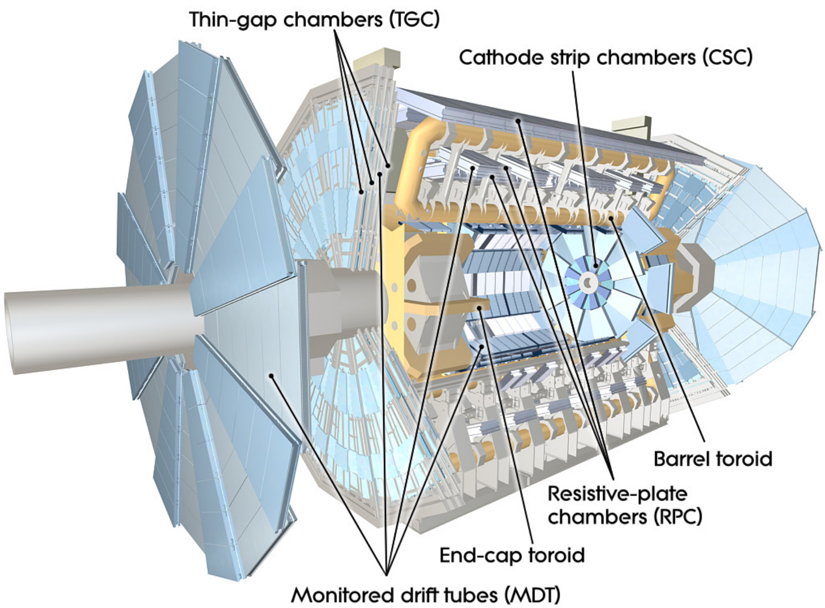

Figure 3.6: Illustration of the ATLAS Muon Spectrometer with components indicated.

MDT

The MDTs in the barrel region, $|\eta| < 1.05$, are placed in three cylindrical layers around the beampipe. Figure 3.7(a) shows an x-y cross section of the detector. Sixteen ϕ-sectors are defined, with alternating large and small MDTs. MDTs from the three layers are named inner, middle and outer chambers according to their distance from the interaction point[2]. Abbreviations are used to indicate the type of chamber. For example, a BOL chamber indicates a large chamber in the outer layer of the barrel.

[2]The Inner layer is obviously located closest to the interaction point.

In the endcap region there are three MDT wheels, with the same sixteen ϕ-sectors and alternating large and small chambers configuration as in the barrel. The naming of inner, middle and outer chambers again follows the orientation with respect to the interaction point. An EMS chamber is a small chamber in the middle layer of the endcap.

Additional MDTs are placed between barrel and endcap, in the region around the endcap toroid. The magnetic field integral for this region is very low. The BEE and EEL/EES chambers should improve the muon measurements in this challenging region. Figure 3.7(b) shows a y-z cross section of the spectrometer.

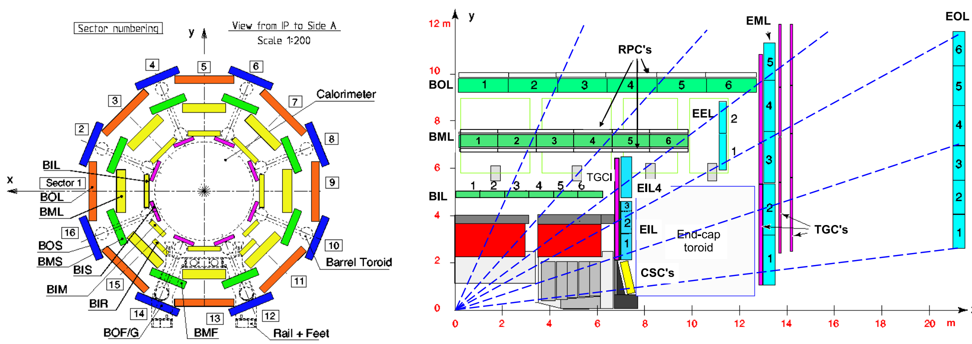

(a) (b)

Figure 3.7: (a) Transverse and (b) longitudinal cross sections of the spectrometer.

Each MDT chamber consists of two multilayers of monitored drift tubes. The drift tubes are aluminum tubes with a diameter of about 30 mm. Each tube contains an anode wire of 50 μm and an Ar:CO_2 gas mixture (93:7). A positive high voltage of 3080 V is applied to the wire. Figure 3.8(a) shows the operation principle of an MDT.

A muon passing a tube ionizes the gas, resulting in a flow of electrons towards the wire and ions towards the tube wall. Close to the wire the kinetic energy of the electrons is sufficient to free new electrons, creating an *avalanche* of electrons. The drifting charges induce a changing potential which causes an electric signal in the readout of the wire. The signal pulse shape has a steep rising edge, due to the fast electrons, but a long tail, due to the slow ions. Readout electronics measure both the time at which the signal pulse passes a predefined threshold value and the accumulated charge in the next 20 ns.

The measured drift time consists of several contributions, which need to be corrected for. These contributions include, for example, delays due to cabling and front-end electronics, t_0, and time slewing, t_{slew}. The latter can be corrected for by using the measured accumulated charge. The value of t_0 is obtained from a calibration procedure. For cosmic data taking a special procedure was developed, which will be discussed in Section 3.5.5. During reconstruction the corrected drift time is converted into the closest radial position of the muon to the anode wire, R_{min}, using an rt-relation. A dedicated calibration procedure determines the rt-relation from data. A detailed discussion on the operation of the MDTs can be found in ref. [34].

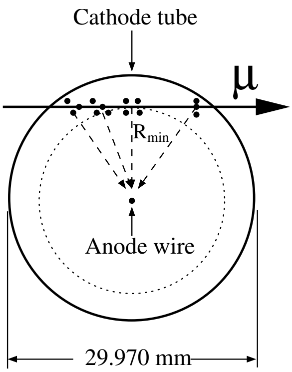

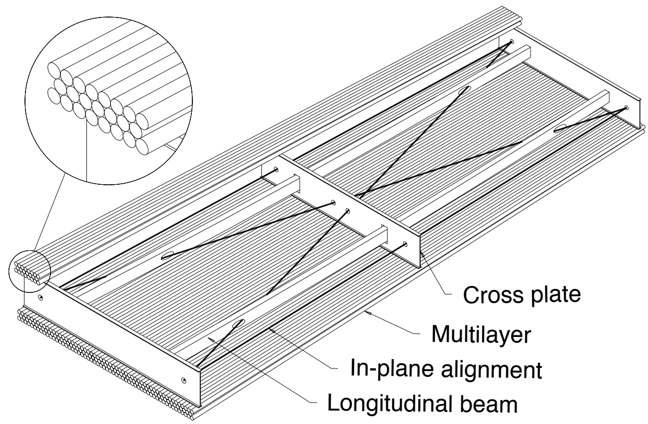

Figure 3.8: Illustration of (a) the operation principle of an MDT and (b) the layout of an MDT chamber.

Each multilayer has three (four) layers of tubes for the Middle and Outer (Inner) chambers, resulting in an average of six (eight) measurements, or *hits*, per chamber per muon. Figure 3.8(b) shows the layout of an MDT chamber. The tubes are oriented perpendicular to the beam axis, aligned with the toroidal magnetic field. This way the precision measurement of R_{min} is in the yz-plane, i.e. in θ. The MDT chambers in general have no sensitivity in the xy-plane, i.e. in ϕ, and use information from the trigger chambers for this. Some special twin tube chambers, which do provide information on the xy-position for the muon track, are designed and installed in the Muon Spectrometer. A proof of principle for operation of these chambers with cosmic data is given in ref. [35].

CSC

The CSCs are located in the first layer of the endcap at $2.0 < |\eta| < 2.7$, as shown in Figure 3.7(b). They are precision tracking chambers like the MDTs but the CSCs are designed to withstand the high counting rates at large pseudorapity. There is one CSC endcap disk on each side of the interaction point. As for the MDTs the CSCs are segmented in large and small chambers. Figure 3.9 shows the eight large and eight small chambers in one CSC endcap disk.

CSCs are multiwire proportional chambers. Instead of one cathode tube and one anode wire, as was the case for MDTs, CSCs have two cathode strip planes and multiple anode wires in a single CSC plane. The wire to anode distance is equal to the wire-to-wire distance of 2.5 mm. The cathode strips are segmented perpendicular to each other, where one strip is parallel to the wires. This way each CSC plane provides a measurement on η and ϕ of the muon. There are four CSC planes in a chamber. A typical muon passing the CSCs acceptance will thus have four measurements of the η and ϕ coordinates of the muon.

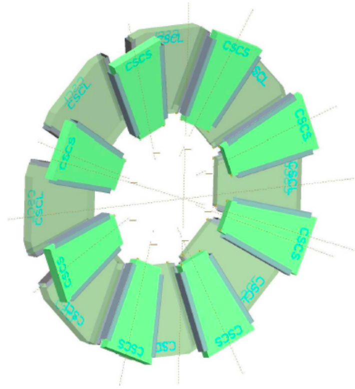

Figure 3.9: Schematic view of the layout of a CSC disk.

RPC

RPCs are used in the barrel region ($|\eta| < 1.05$) to trigger on muons and to measure the ϕ coordinate of the muon. As for the MDTs there are three layers of RPCs. Two are mounted on both sides of the barrel middle MDTs. One is located on the barrel outer MDT chamber. Figure 3.10 shows this configuration in an x-y cross section.

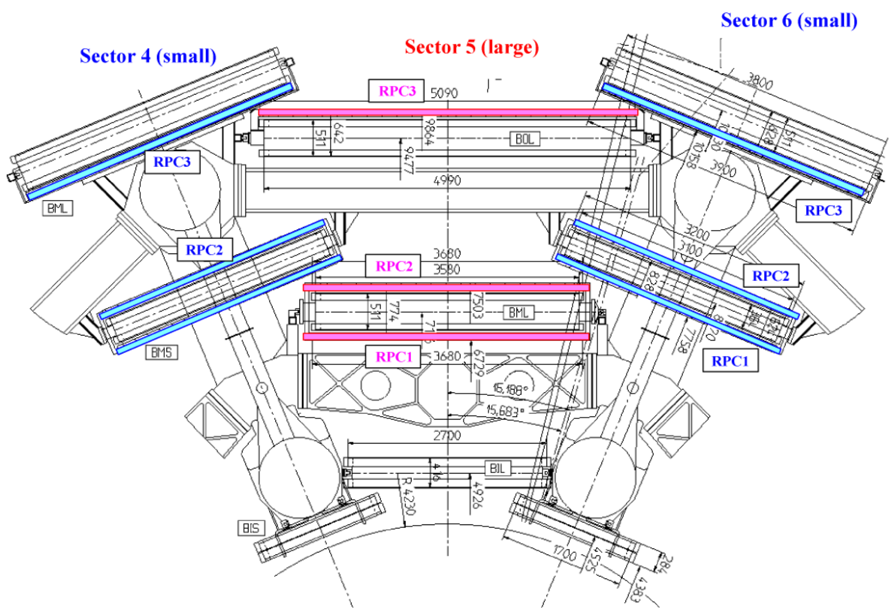

Figure 3.10: RPC positioning on MDT chambers.

An RPC is a gaseous parallel electrode-plate detector operated in avalanche mode. When a charged particle passes through the gas it creates an avalanche of secondary charges particles. The two plates are at 2 mm distance and are connected to two read-out strips. One strip reads out the ϕ coordinate, the other the η coordinate. A ϕ-strip length and time jitter is on average half that of a η-strip, giving it a more precise timing. The ϕ-strip information is also needed for the pattern recognition.

Low-p_T muons ($4-10$ GeV) are triggered by coincidences in the two innermost RPC layers, i.e. RPC1 and RPC2 in Figures 3.10 and 3.11 . For high-p_T muons (> 10 GeV) an additional coincidence is required in the RPC3 layer.

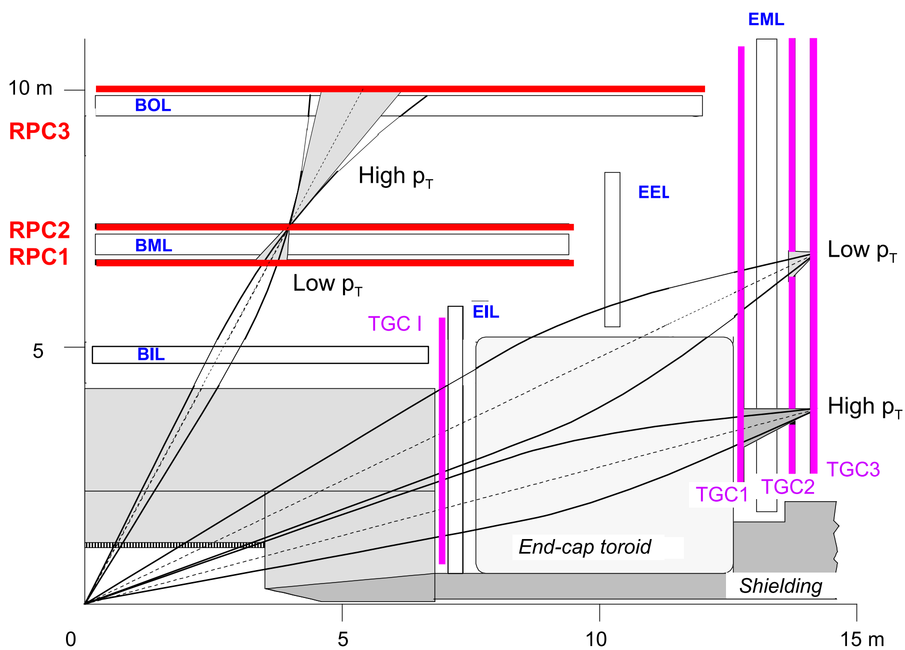

Figure 3.11: Schematic view of low-p_T and high-p_T triggers in RPC and TGC.

TGC

Triggering in the endcap ($1.05 < |\eta| < 2.4$) is performed by the TGCs. These are located as indicated in Figure 3.11: one layer before the inner MDT endcap wheel and three layers around the middle MDT wheel. No measurement is needed at the outer MDT wheel since accurate extrapolations are possible from middle to outer wheels, due to the absence of a magnetic field in that region.

TGCs are multi-wire proportional chambers, like the CSCs. The wire to anode distance of 1.4 mm is smaller than the wire-to-wire distance of 1.8 mm. Figure 3.12 shows the structure of a TGC chamber. The smaller wire-to-wire distance in TGCs lead to very good time resolution properties, sufficient for triggering in ATLAS.

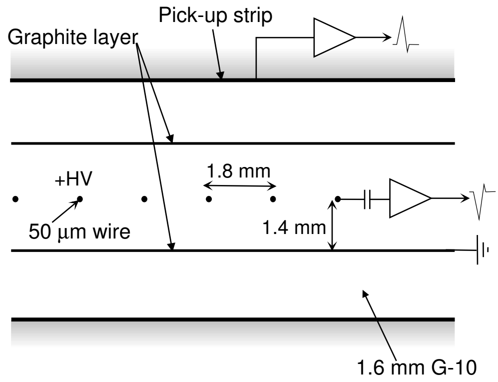

Figure 3.12: TGC structure.

3.5 Muon reconstruction algorithms

For physics measurements we are interested in the properties of the muon, in particular its (transverse) momentum. These can be derived from the trajectory, or track, of the muon in the detector. The curvature, or sagitta, of the track is a measure of the muon momentum. Reconstruction of the muon track in the Muon Spectrometer is performed in three steps:

1. **pattern finding -** all hits in each other's vicinity are grouped together in a *pattern* to obtain a first crude estimate of the muon properties. The pattern recognition uses Hough transforms, a robust technique for identifying multidimensional shapes and patterns and estimating their parameters[3] (cf. refs. [36, 37]);

2. **segment making -** the hits from the pattern recognition are grouped per MDT chamber layer. Straight track fits are performed per layer to obtain *segments*;

3. **track fitting -** segments are recombined while adding ϕ measurements. A *track* is fitted to these combinations, giving the best possible information on the properties of the muon.

Selections are applied at each step to ensure reconstructed muons of good quality for physics analyses. At the time of writing this thesis, two main reconstruction chains exist in ATLAS[4]: `MUID` [38] and `STACO` [39]. We will address `MUID` reconstruction strategies below. More information on the pattern recognition can be found in refs. [34, 37].

In addition to measurements in the Muon Spectrometer also measurements from the Inner Detector and Calorimeters can be used to reconstruct muon tracks. Different strategies to combine information from the various detector components are implemented in ATLAS and will be discussed below.

[3] It was originally developed in 1962 by Paul Hough to analyze bubble chamber pictures at CERN.
[4] They are currently being merged into one chain by a dedicated task force.

3.5.1 Standalone muons

The standalone reconstruction of a muon track is based on information from the Muon Spectrometer only. The track resulting from the three steps described above is the output muon track. Muon properties can be expressed at two locations: the entrance to the Muon Spectrometer (i.e. the inner MDT chamber layer) or the interaction point. The latter requires an extrapolation of the muon trajectory through the Calorimeter and Inner Detector material. Depending on whether or not such an extrapolation was performed these muons are referred to as standalone muons or extrapolated standalone muons. Most physics analyses are interested in the muon properties close to the interaction point and thus use the extrapolated standalone muons.

3.5.2 Combined muons

Combined reconstruction uses tracks from the Muon Spectrometer (MS) and Inner Detector (ID) to perform a refit. A muon track from the MS is matched to a track from the ID. A full refit of the track is performed, resulting in so-called combined muons. These combined muons are the highest quality muons in ATLAS. They have the best momentum measurement as they combine the track parameters from the ID and MS in an optimal way. For low-p_T muons the ID resolution dominates the combined momentum measurement. The MS resolution dominates for high-p_T muons.

3.5.3 Segment tagged muons

The combined reconstruction algorithm requires a reconstructed track in both the Inner Detector and the Muon Spectrometer. In some cases no standalone muon track is found and only segments are available. This can for example be the case for low-p_T muons or muons in regions where the Muon Spectrometer has little or no coverage, e.g. $\eta \approx 0$.

Dedicated segment tagger algorithms were developed to recover these muons. These algorithms start from the Inner Detector track and match it to Muon Spectrometer segments. Kinematic cuts as well as quality cuts are applied to ID tracks and MS segments to reduce computing time. When a match is found, the ID track is tagged as a muon. The ID track parameters are stored as the muon properties. More information on the procedure for segment tagged muons can be found in ref. [40].

3.5.4 Calorimeter tagged muons

This algorithm is similar to the segment tagged algorithm since it also aims at tagging an ID track as a muon track. The tagging is performed by looking at energy deposits in the calorimeter. Calorimeter tagged muons can e.g. be used to recover muons in the Muon Spectrometer gap region at $\eta < 0.1$. They can also be used to reject fake muons, for example from pions passing through the calorimeter. Because the calorimeter measurements are independent of the Muon Spectrometer they can be used to measure precisely the muon reconstruction efficiency. More information on the calorimeter muon reconstruction can be found in ref. [41].

Table 3.2 gives an overview of the different reconstruction algorithms and their input sources of information.

	Information used from		
Algorithm	Inner Detector	Calorimeter	Muon Spectrometer
Standalone	-	-	tracks
Combined	tracks	-	tracks
Segment tagged	tracks	-	segments
Calorimeter tagged	tracks	energy deposits	-

Table 3.2: Muon reconstruction algorithms.

3.5.5 Reconstruction of cosmic-ray muons

Chapter 4 shows results for Muon Spectrometer performance studies with cosmic-ray muons. These studies were performed in the barrel region ($|\eta| < 1.05$) of the detector. In this region muons are triggered and detected by RPCs and MDTs. Several adjustments in the reconstruction algorithms were needed to allow for an efficient reconstruction of cosmic-ray muons.

Muon reconstruction algorithms are optimized to reconstruct muons that originate from the Interaction Point (IP) and with trigger signals that are synchronized with LHC bunch crossings. Cosmic-ray muons do not originate from the IP and are asynchronous with the detector clock. The latter results in a 25 ns time jitter with respect to the clock used by the trigger chambers. In addition to this, the trigger chambers were not timed with sufficient precision during the cosmic-data taking because of ongoing commissioning efforts. At the moment of cosmic data taking a precise alignment of the MDTs was not available[5]. Some requirements for track reconstruction had to be relaxed to allow for efficient measurements of these out of time and non-pointing cosmic-ray muons.

Reconstruction adjustments

As discussed above the muon reconstruction consists of three steps: pattern recognition, segment making and track fitting. In all of these steps several adjustments were made to obtain a high reconstruction efficiency in cosmic-ray data.

In the pattern recognition the straight line Hough transform was adjusted to allow for non-pointing tracks. In addition the cuts on the distance between obtained pattern and segment candidates were relaxed.

[5]In fact, the cosmic-ray muons were used to align the MDTs, see e.g. ref. [42].

In the segment finding no cuts on missing MDT hits were applied. A missing MDT hit is a tube where a hit was expected but not measured. During the segment fitting a t_0 refit procedure was applied which will be discussed in detail below. If this segment fit failed the MDT errors were enlarged to 1 mm and the fit was performed again. Hits with a distance to segment of more than 7σ were removed from the segment.

The track fit was performed with enlarged MDT errors. The error was set to 2 mm to account for uncertainties in the alignment of the MDT chambers.

The performance of the muon reconstruction algorithms was optimized for collision data using simulation samples. The optimization is always a matter of trying to obtain a high efficiency while keeping the number of fake muons acceptable. Relaxing the optimized cuts in collision data would lead to an increase of efficiency at the cost of an increase of fake muons. However, for cosmic-ray data the number of fake muons is negligible and the cuts can be relaxed.

t_0 refit

Figure 3.8(a) illustrates the operation principle of an MDT for a passing muon: the muon ionizes the gas and the drifting electrons and ions create a signal at the read-out electronics of the wire. The electronics registers the time at which the wire signal passes a predefined threshold value. The measured time is delayed with respect to the actual time of passing the tube. Per MDT the distribution of measured drift times can be used to extract the minimum and maximum drift times t_0 and t_{max}, respectively. Figure 3.13 shows a typical drift time spectrum where a fit of a Fermi function is overlaid on the rising edge. The t_0 is determined from this fit.

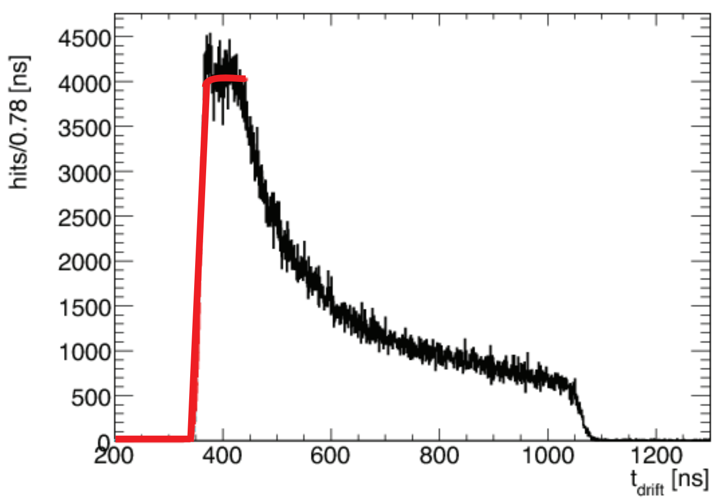

Figure 3.13: Typical drift time spectrum for an MDT chamber in cosmic-ray data [42].

After commissioning of the Muon Spectrometer the t_0 values for each tube will be known and monitored. However, during the period of cosmic-data taking the MS was not yet fully commissioned and a procedure called Global t_0 refit was implemented to improve the quality of track reconstruction [43]. This is an iterative procedure which determines a single t_0 value for all hits on a reconstructed segment in the Muon Spectrometer. It contains the following steps:

1) vary t_0 for all hits on a segment;
2) calculate drift times using the new t_0;
3) calculate drift radii using the drift times and the rt-relation (cf. Section 3.6);
4) calculate hit residuals, i.e. distance from hit to segment;
5) calculate $\chi^2 = \Sigma \frac{residuals_i^2}{\sigma_i^2}$, where σ is the uncertainty on the residual[6];
6) repeat steps 1 to 5 until minimum value for χ^2 is obtained.

The value for t_0 which minimizes the χ^2 is used for all hits on the segment. A typical t_0 resolution of 2 to 4 ns is obtained using this procedure.

3.6 Precision of the Muon Spectrometer

The design of the Muon Spectrometer was driven by the momentum resolution requirement listed in Table 3.1: $\sigma_{p_T}/p_T = 10\%$ at $p_T = 1$ TeV. Various sources contribute to the momentum resolution of the spectrometer. Figure 3.14 shows their expected relative contributions. Three different momentum regions can be identified: low-p_T ($p_T < 20$ GeV), intermediate-p_T ($20 < p_T < 100$ GeV) and high-p_T ($p_T > 100$ GeV).

In the low-p_T region the resolution is dominated by energy loss fluctuations in the calorimeter. For low-p_T muons the use of combined muons will prevent this resolution degradation as the Inner Detector is designed to provide good momentum resolution at low-p_T. At intermediate-p_T the multiple scattering is the largest contribution. In this region the Muon Spectrometer and Inner Detector have a similar momentum resolution. For high-p_T muons the Muon Spectrometer has a better momentum resolution. The intrinsic resolution of the MDTs and the chamber alignment give the largest contributions to the momentum resolution at high-p_T. The main contributions at intermediate and high-p_T are discussed below.

[6] The MDT uncertainties were set to twice the value obtained from test beam results.

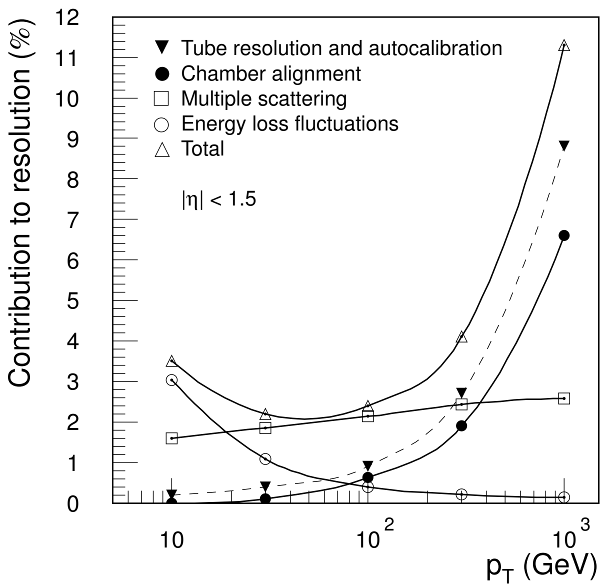

Figure 3.14: Expected Muon Spectrometer momentum resolution for $|\eta| < 1.5$ [44].

Multiple Scattering

Multiple scattering refers to the repeated scattering of the muon when it passes through detector material. The probability that a particle is deflected by an angle θ after traveling a distance L in the material is given by a Gaussian distribution with a sigma of

$$\theta_0 = \frac{0.0136}{\beta cp[GeV/c]} Z_1 \sqrt{\frac{L}{X_0}}, \tag{3.1}$$

where X_0 is the radiation length of the material, Z_1 is the charge of the particle and p is the momentum of the particle.

The track curvature, or sagitta s, is inversely proportional to the muon momentum, i.e. $s \propto 1/p$. The uncertainty on the sagitta measurement that comes from multiple scattering effects is $\Delta s(MS) \simeq \theta_0 L$, with $\theta_0 \propto 1/p$. When evaluating the relative contribution $\Delta s(MS)/s$ we find that the momentum cancels out to first approximation. Figure 3.14 indeed shows a fairly constant contribution to the momentum resolution.

Tube resolution and autocalibration

The precision tracking chambers of the Muon Spectrometer are MDTs and CSCs. The average intrinsic resolution for a single MDT is 80 μm. A segment in a middle or outer (inner) MDT chamber has on average 6 (8) MDT hits, resulting in a contribution to the segment resolution of 35 (30) μm. For a single CSC plane the average intrinsic resolution is 60 μm. With four CSC planes per chamber this results in a contribution to the segment resolution of 35 μm.

The calibration of the tubes is an important ingredient to the tube resolution. The measured drift time t is converted to a drift radius r via a calibrated rt-relation. This rt-curve is determined daily by an autocalibration procedure which compensates for variations of external parameters such as pressure, temperature, impurities, magnetic field and count rate. The required rt accuracy of 20 μm can be achieved with about 2,000 segments per chamber [45].

Chamber alignment

To achieve the performance goals for momentum resolution the relative positioning of the MDTs and CSCs should be known to 30 μm accuracy. An optical alignment system is implemented in the detector to monitor the relative positioning of the detector components. No attempt is made at physical chamber repositioning. The optical alignment systems are accurate to several micrometers.

Chambers that are not optically linked to other chambers can be aligned using tracks crossing an overlap between two ϕ-sectors. The alignment of the two endcaps with respect to the barrel should be done by tracks overlapping chambers in barrel and endcap. Toroid off runs are foreseen to provide straight muon tracks that can be used for this alignment with overlap tracks. About 15,000 tracks with $p_T > 10$ GeV per chamber triplet would provide the necessary accuracy of 30 μm. This corresponds to about a day of data taking at a luminosity of 10^{33} cm^{-2}s^{-1}.

3.7 Summary

In this chapter the ATLAS detector was discussed in some detail. We addressed the trigger system needed to keep data taking at a rate manageable by offline computing power and storage capacity. The ATLAS magnet system was covered, showing the huge toroidal magnet structures that dictate the dimensions of the ATLAS detector. All the detector technologies were discussed, ranging from the tracking detectors in the innermost and outermost regions of ATLAS to the calorimeters in between.

The expected precision of the Muon Spectrometer and its main contributions at intermediate and high-p_T were discussed. These are the momentum regions of interest for the $Z \rightarrow \mu^-\mu^+$ studies covered in Chapter 5. The muon reconstruction algorithms were discussed in some detail as these will be of particular interest in the following chapters. Some adjustments in the reconstruction algorithms are needed to cope with cosmic-ray muons, which are used for the Muon Spectrometer performance analyses described in the next chapter.

Chapter 4

Performance of the Muon Spectrometer with cosmic-ray data

4.1 Introduction

In the absence of collision data a large part of the commissioning of the ATLAS Muon Spectrometer was performed using cosmic-ray muons. These cosmic muons were exploited in several ways to study the performance of the Muon Spectrometer, as published in refs. [42] and [46]. This chapter focuses on two methods using either straight tracks or curved tracks for the analysis. In Section 4.3 the sagitta resolution method is discussed. The momentum resolution method uses tracks curved by the magnetic field and is the subject of Section 4.4.

Cosmic muons do not cross all of the Muon Spectrometer with equal frequency. Their incident angles are close to the vertical axis and therefore most statistics are obtained in the barrel region of the detector ($|\eta| < 1.05$). This is illustrated in Figure 4.1, where the ATLAS x and z-coordinates[1] of cosmic muon tracks extrapolated to the surface level (i.e. $y = 81$ m) are displayed. Large and small (access) shafts are visible at $z = +15$ m and -25 m respectively. Other smaller (elevator) shafts are visible at $x = +30$ m and -30 m. In the barrel, only the top and bottom sectors have sufficient statistics for performance studies with cosmic-ray data.

4.2 Data sample

The data sample used to evaluate the performance of the Muon Spectrometer amounts to approximately 60 million cosmic-ray events. These were obtained between September 2008 and July 2009 with various trigger and magnetic field configurations as is detailed in Table 4.1. Most data were obtained with a barrel trigger (i.e. RPC, cf. Section 3.4.3).

During the fall 2008 period only five out of 1,110 MDT chambers were not included in the data taking: two were not yet connected to services and three had problems with the gas system [42]. This illustrates the fact that cosmic data allowed for a full commissioning of the ATLAS MDT chambers.

[1] z-axis is along the beamline, x-axis point towards center of the LHC ring (cf. Section 3.1.1).

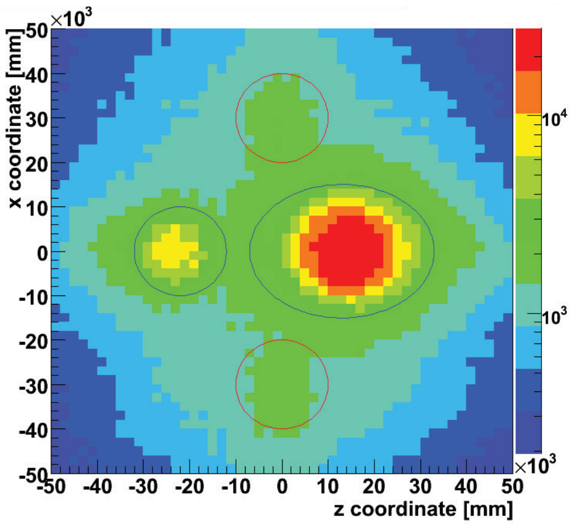

Figure 4.1: x and z-coordinates of cosmic-ray muons extrapolated to the surface level.

Run	Trigger	B-field	N of Evts	Period
89106	TGC	Off	0.4 M	Fall '08
89403	TGC	Off	0.4 M	Fall '08
91060	RPC	Off	17 M	Fall '08
91060	TGC	Off	0.2 M	Fall '08
91803	TGC	On	50 k	Fall '08
91890	RPC	On	16 M	Fall '08
113860	RPC	Off	6 M	Spring '09
121080	RPC	On	21 M	Summer '09

Table 4.1: Data taking periods used for cosmic analysis as reported in [42].

4.3 Sagitta resolution

4.3.1 Introduction

The Muon Spectrometer (MS) consists of three layers of MDT chambers (cf. Chapter 3). The reason behind this layout is to measure the muon at three points, reconstruct a muon track and determine the track curvature. This curvature is inversely proportional to the muon momentum.

The sagitta, s, is a measure for the curvature and is defined as the deviation from a straight line as is schematically illustrated in Figure 4.2. In ATLAS the curvature of path L normally is the result of the Lorentz force acting on the muon, due to the presence of a magnetic field B. But in the datasets used for the sagitta resolution studies no B-field was present in the MS[2]. A nonzero sagitta can then be the result of various causes, such as a misalignment of the detector and multiple scattering of the muon in the detector material.

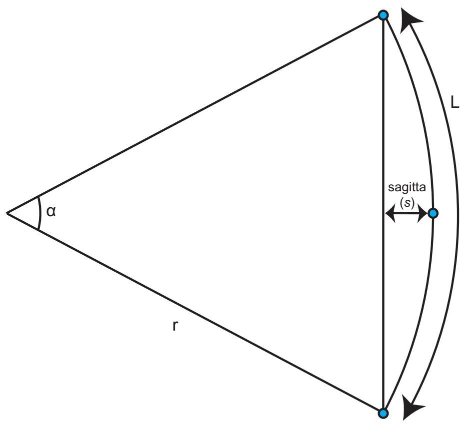

Figure 4.2: Definition of the sagitta. The dots schematically represent the three chamber layer measurements within the ATLAS Muon Spectrometer.

An alignment campaign with cosmic-ray data was ongoing at the time of data taking. Although the final alignment results were not yet available in the reconstruction used in our analysis, the results did benefit from this effort. Figure 4.3 illustrates the effect of the alignment corrections on the measured sagitta distributions in the endcap regions. More information on the alignment campaign can be found in ref. [42].

There is a significant difference in material that is crossed for muons in large and small MDT chamber sectors: in the small sectors the toroid magnet coils have to be traversed. The contribution of the multiple scattering to the sagitta resolution in the small sectors is therefore about twice as large. In the analysis following hereafter large and small sectors are treated separately.

[2]The solenoid was however operational allowing for a momentum measurement in the Inner Detector.

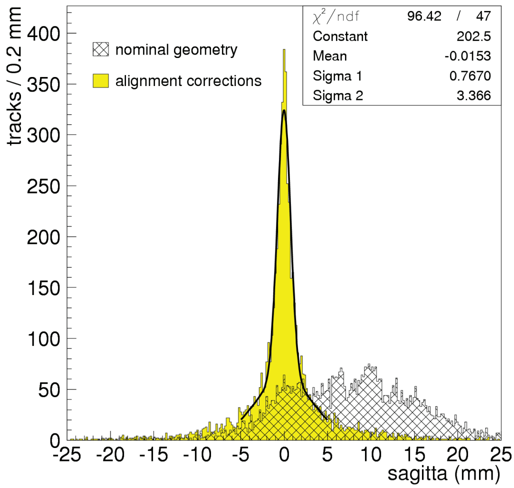

4

Figure 4.3: The sagitta distribution for cosmic-ray muons reconstructed in the endcap regions with nominal geometry and after alignment corrections.

4.3.2 Event, track and segment selection

The sagitta resolution analysis is based on muon tracks. Events, tracks and segments for the analysis are selected with a few well understood selections:

- events are discarded if they contain more than 20 segments, thereby rejecting cosmic showers;
- exactly one Inner Detector (ID) track per event is required to ensure an unambiguous (and thus correct) matching between ID and MS tracks;
- all hits on a track need to be within the same ϕ-sector, preventing effects from possible misalignments between different ϕ-sectors[3];
- the track should contain at least two RPC ϕ-layer hits, providing an unambiguous measurement of the ϕ-angle of the track;
- the fit-χ^2/D.O.F. of the MS track is required to be smaller than 5;
- the MS track is required to have segments in all three MDT chamber layers;
- the inner, middle and outer segments should each contain at least 5, 4 and 4 hits, respectively. To ensure high quality segments a successful t_0 refit is required (cf. Section 3.5.5).

[3]This also ensures the separation between large and small MDT chambers.

4.3.3 Analysis of the sagitta resolution

The Sagitta Analysis [47] starts with a selected muon track and divides the hits on the track in two groups: hits from the inner+outer chambers and hits from the middle chamber. The two groups of hits are used to obtain straight line fits, resulting in one straight line through inner+outer chamber hits and one line through the middle chamber hits. Both of the straight lines are projected in the precision plane of the MS. The sagitta s is then defined as the distance between the center of the line through the middle chamber and the line through the inner+outer chambers, as illustrated in Figure 4.4. It is calculated for each muon passing the selections mentioned in Section 4.3.2.

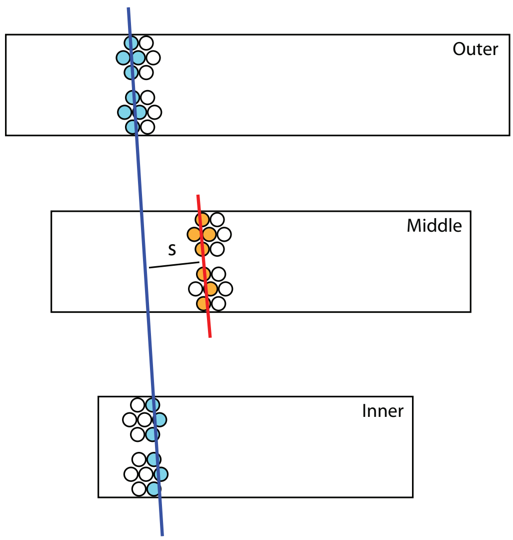

Figure 4.4: Illustration of the performed measurement of the sagitta, s.

The sagitta distributions obtained in this way are used to evaluate the performance of the MS. A double Gaussian function, with a common mean value, is fitted to the sagitta distribution. An example of such a fit is shown in Figure 4.5.

The narrow Gaussian describes the resolution in the core of the sagitta distribution. The standard deviation of the narrow Gaussian is taken as the sagitta resolution. The broader Gaussian describes the tails of the sagitta distribution and predominantly contains contributions from low-p_T, i.e. multiple scattering dominated, muons. The fraction of events in the narrow Gaussian is fixed to 70%, resulting in the best fits. By using the momentum measurement of the matched tracks from the ID (where the momentum is determined from the curvature in the solenoidal field) one can study the sagitta resolution versus momentum.

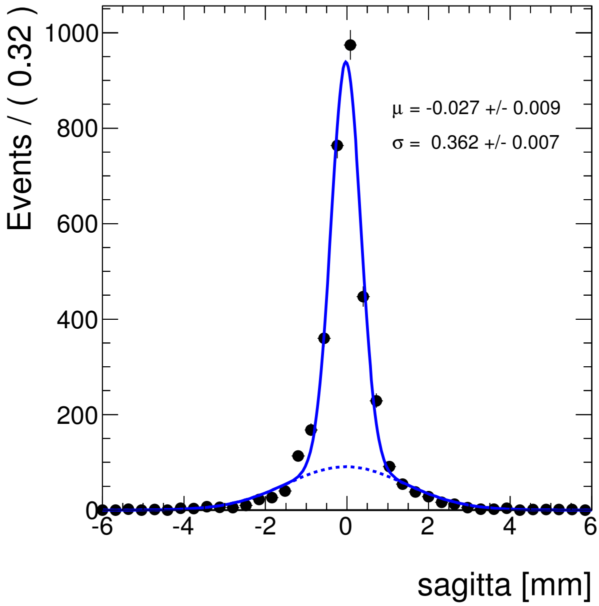

Figure 4.5: Sagitta distribution for ϕ-sector 05 in run 91060.

4.3.4 Results

Figure 4.5 shows an example of a sagitta distribution, for ϕ-sector 05 at the top of the Muon Spectrometer, in run number 91060. The mean value of -0.027 ± 0.009 mm is compatible with the design goal for alignment precision of 30 μm [45].

Fits are performed for successive momentum intervals ranging from 10 to 350 GeV, covering the momentum range of cosmic-ray muons. A comparison to simulation is performed by running the analysis on a simulated cosmic-ray sample. The simulation uses a dedicated event generator based on the work described in ref. [48] and the standard GEANT4 detector simulation [24].

The obtained sagitta resolution as a function of momentum for top sectors is shown in Figure 4.6 for data and simulation. The curves are fitted using the parametrization

$$\sigma_s = \frac{K_0}{p} \oplus K_1, \tag{4.1}$$

where K_0 and K_1 represent the multiple scattering and intrinsic resolution term, respectively.

The obtained values for K_0 and K_1 in cosmic-ray data and simulation are listed in Table 4.2. Note that the multiple scattering term is on average indeed about twice as large for small compared to large sectors as was mentioned in Section 4.3.1.

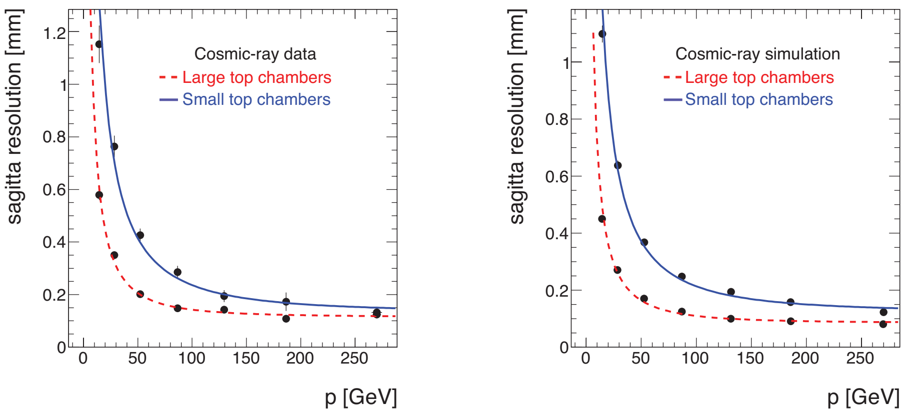

(a) (b)

Figure 4.6: Sagitta resolution as a function of muon momentum for top sectors in (a) data and (b) simulation. The curve indicates the fitted function as described in the text.

Chamber type	Sample	K_0 [mm×GeV]	K_1 μm
Large	Data	8.6 ± 0.2	114 ± 6
	Simulation	7.0 ± 0.1	84 ± 2
Small	Data	19.2 ± 0.8	160 ± 3
	Simulation	17.0 ± 0.3	151 ± 8

Table 4.2: Results of the sagitta resolution analysis on cosmic-ray data and simulation.

Both K_0 and K_1 show differences between the values obtained for data and simulation. The difference for K_0 can be understood as a deficit in material used in the simulated sample. For K_1 the difference arises from various causes, including alignment, chamber deformations and calibrations. Both differences are also observed in the momentum resolution studies and will be discussed in Section 4.5.

4.4 Momentum resolution

4.4.1 Introduction

In addition to the sagitta resolution studies with straight tracks, the performance of the Muon Spectrometer (MS) was further studied using curved tracks.

If a cosmic muon is energetic enough it can traverse the full ATLAS detector and two tracks can be reconstructed: one in the top and one in the bottom sectors of the MS. It is this category of energetic cosmic muons that is used in the momentum resolution analysis. The analysis exploits the fact that there are two momentum measurements obtained for the same cosmic muon, i.e. p_{up} and p_{down}.

Each muon momentum measurement can be expressed at two locations in the ATLAS detector: at the Interaction Point (IP) and at the entrance of the MS. The latter is defined as the MS measurement closest to the interaction point[4]. When expressing the momentum at the IP energy loss corrections have to be applied to account for the energy lost by the muon when traversing the calorimeter. In the barrel region the typical energy loss correction is 2.5 GeV (4 GeV) for a muon of 10 GeV (1 TeV) [45].

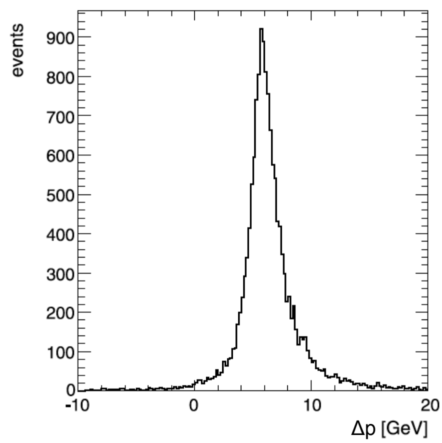

Figure 4.7: Distribution of the difference in momentum between up and down tracks for tracks with $p_T > 15$ GeV and momenta expressed at the entrance of the MS.

Figure 4.7 shows $\Delta p \equiv p_{up} - p_{down}$ for momenta expressed at the entrance of the MS. The average value of this distribution is 6.3 GeV, corresponding to about twice the average energy lost when a muon traverses the calorimeter material. A non-Gaussian tail due to energy loss fluctuations can be observed. This particular shape is described by a Landau distribution in the resolution analysis. Figure 4.8 shows the momentum distributions for up and down tracks before and after energy loss corrections, i.e. expressed at the entrance to the MS and at the IP respectively.

The momentum resolution analysis uses the relative momentum difference to measure the momentum resolution directly. In fact the relative *transverse* momentum difference will be used as this is the more convenient measure in hadron collider experiments:

$$\frac{\Delta p_T}{p_T} \equiv 2\,\frac{p_{T_{up}} - p_{T_{down}}}{p_{T_{up}} + p_{T_{down}}}. \tag{4.2}$$

[4]The definition is with the assumption that the muons are from collisions.

The transverse momentum resolution is equivalent to the momentum resolution if the angles θ_{up} and θ_{down} are approximately equal, as is the case for cosmic-ray muons.

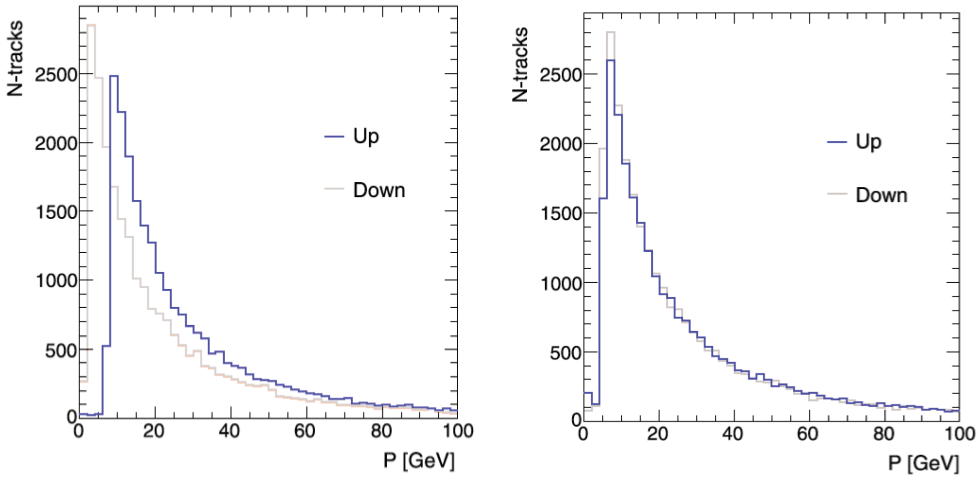

(a) (b)

Figure 4.8: Momentum distributions for up and down tracks showing (a) the measurements at entrance to the Muon Spectrometer and (b) the measurements after extrapolation to the interaction point.

4.4.2 Event and track selection

The following selections are applied on events and tracks:

- the event should contain two tracks;
- the tracks should be back to back, i.e. $\Delta\theta < 10°$ and $\Delta\phi < 10°$.

The above selections are designed to obtain a sample of candidate cosmic-ray muon tracks, where each muon leaves back to back tracks in the upper and lower hemisphere of the MS. In addition each track is required to pass the following selections:

- at least 17 MDT hits, of which $\geq$ 7 in inner, $\geq$ 5 in middle and $\geq$ 5 in outer chamber stations;
- at least two RPC ϕ-layer hits;
- all MDT hits should be within the same ϕ-sector;
- polar angle: $65° < \theta < 115°$;
- impact parameters: $z_0 < 2$ m and $|d_0| < 1$ m, where $|d_0| \equiv \sqrt{x_0^2 + y_0^2}$.

These selections provide high quality tracks with incident polar angle and impact parameters that are expected for cosmic-ray muons. Each track is required to be within a single ϕ-sector to remove possible effects from overlap between sectors. The selections resulted in approximately 19,000 cosmic-ray events.

4.4.3 Analysis of the momentum resolution

The momentum resolution as a function of p_T is obtained by performing fits to $\Delta p_T/p_T$ distributions (cf. Equation 4.2) in eleven bins of p_T. The fitting function is a double Gaussian with common mean. The double Gaussian is chosen for the same reasons as in the sagitta resolution studies: the narrow Gaussian describes the core and the broad Gaussian describes the tails of the distribution. In this analysis, however, the narrow Gaussian is convoluted with a Landau function to account for the non-Gaussian tails arising from energy loss fluctuations in the extrapolation to the IP (cf. Section 4.4.1).

The contribution of these energy loss fluctuations to the momentum resolution decreases for increasing bins of muon momenta. For lower momenta the non-Gaussian tails of the $\Delta p_T/p_T$ distribution are more pronounced and therefore the relative fraction of the narrow Gaussian (convoluted with a Landau) is fixed to 95% in this momentum regime. For higher momenta ($p_T > 10$ GeV) the energy loss fluctuations form a negligible contribution to the $\Delta p_T/p_T$ distribution and the fraction of the narrow Gaussian is lowered to 70%, as was the case for the fits to the sagitta distributions.

Applying standard error propagation rules and neglecting higher order terms we see that the resolution of the $\Delta p_T/p_T$ distribution gives us the relative p_T resolution, $\sigma(p_T)/p_T$, which is obtained from the standard deviation of the narrow Gaussian and the width of the Landau as

$$\frac{\sigma(p_T)}{p_T} = \frac{\sqrt{\sigma^2_{Gauss} + \sigma^2_{Landau}}}{\sqrt{2}}, \tag{4.3}$$

where the $\sqrt{2}$ comes from the fact that we are using two momentum measurements.

4.4.4 Results

Since the average energy loss is approximately 6.3 GeV (cf. Figure 4.7) the dependence on the Landau term in the distributions of $\Delta p_T/p_T$ should become less pronounced when going to higher momenta. In the fits in Figure 4.9 this can indeed be observed.

A parametrized fit is performed to describe $\sigma(p_T)/p_T$ as a function of p_T:

$$\frac{\sigma_{p_T}}{p_T} = \frac{P_0}{p_T} \oplus P_1 \oplus P_2 \cdot p_T. \tag{4.4}$$

The uncertainty on the energy loss corrections is denoted by P_0, the multiple scattering term by P_1 and the intrinsic resolution term by P_2. The obtained values in cosmic-ray data for P_0, P_1 and P_2 are listed in Table 4.3, showing a comparison to results from an analytic calculation [45]. Differences between data and calculation are observed for the multiple scattering and the intrinsic resolution term, similar to what was found in the sagitta resolution analysis. These differences are discussed further in the next section.

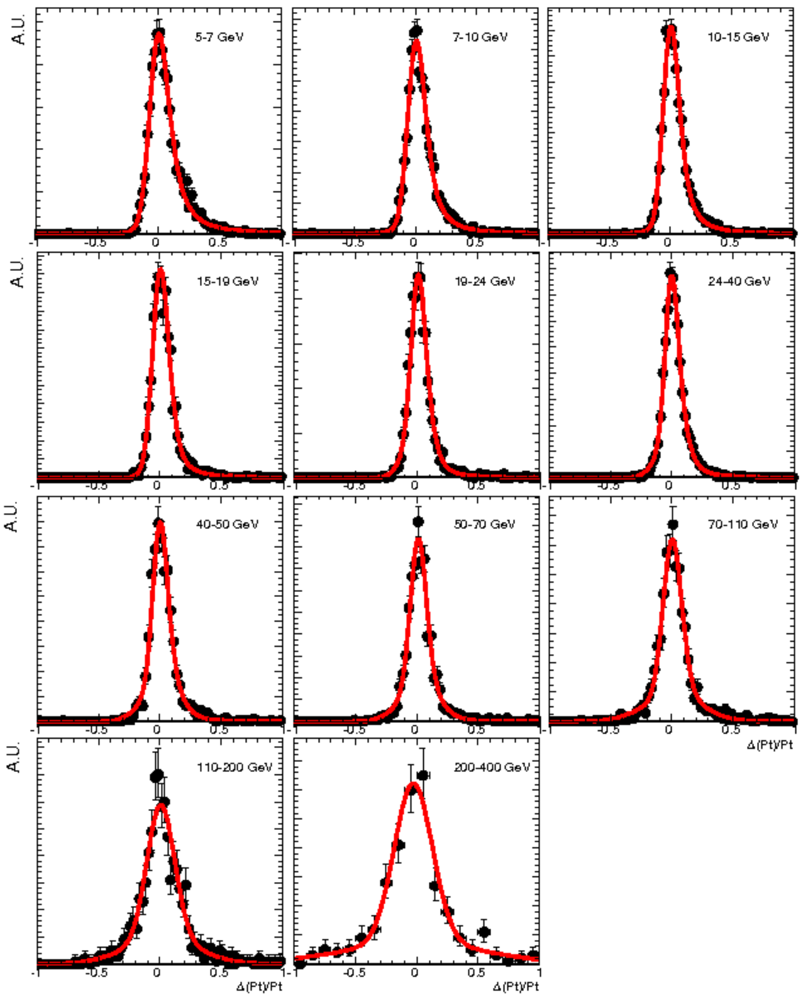

Figure 4.9: The $\Delta p_T/p_T$ distributions in eleven bins of increasing p_T. The dots indicate the data, the curve indicates the fitted function as described in the text.

Sample	$P_0[GeV]$	P_1 [%]	P_2 $[10^{-4}\ GeV^{-1}]$
Data	0.35 ± 0.02	0.038 ± 0.001	2.0 ± 0.3
Calculation	0.35	0.035	1.2

Table 4.3: Momentum resolution analysis results for data and analytic calculation [45].

4.5 Discussion

In the sagitta and momentum resolution analyses presented in this chapter differences between cosmic-ray data and simulation were observed. The multiple scattering term contributing to the resolution was found to be higher in data than in simulation for both analyses, indicating an underestimation of the multiple scattering term in simulation due to a material budget deficit of about $10 - 15\%$ in the detector description. Recent studies show that by adding passive material (such as detector services, rails and trigger boxes) the discrepancy reduces in the barrel region [49].

The obtained results from Table 4.3 are illustrated in Figure 4.10. The measured momentum resolution shows good agreement with the analytic calculation for transverse momenta below about 40 GeV. For high momenta larger discrepancies can be observed.

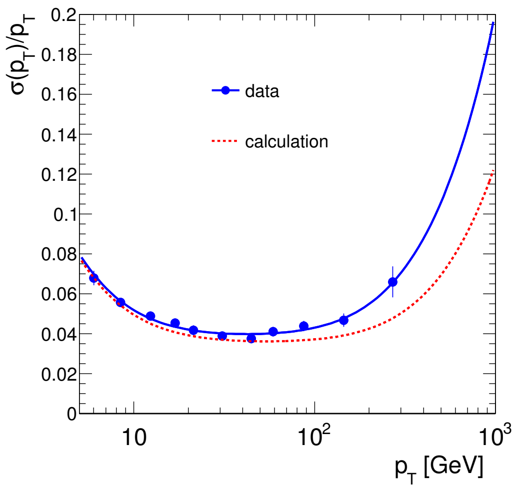

Figure 4.10: Muon Spectrometer momentum resolution for data and calculation [45].

In Section 3.6 we addressed some contributions to the muon momentum resolution. Figure 3.14 shows that for $p_T > 50$ GeV the contributions to the intrinsic resolution, e.g. alignment and calibration, form the most significant contributions. Several causes have been identified to explain a higher measured intrinsic resolution term:

- the magnetic field integral is significantly lower in the large MDT chambers compared to the small MDT chambers. This causes a degradation of the momentum resolution in the high-p_T region; 70% of the MS tracks used for the analysis are measured within the large chambers;
- the single tube resolution was affected by imperfect calibrations and the additional time jitter. The latter is a feature of cosmic-ray events as opposed to pp collision data and is not completely removed by the t_0 refit procedure (cf. Section 3.5.5). It has been checked that removing tracks with bad convergence in the t_0 refit decreased the intrinsic term by 30%;

- the alignment was not yet at the required level at the moment of data taking. The optical alignment system alone provided a precision at the level of 200 μm. When calibrated with sufficient statistics, the optical system is able to monitor chamber movements with a precision of 50 μm [42]. With the datasets used for the analysis this was only possible for the top sectors in the MS;
- several other effects were not yet corrected for in the data processing chain, such as chamber deformations, wire sagging and single chamber geometrical defects. However, these contributions are expected to have a small impact on the momentum resolution.

4.6 Results of combined cosmic data taking

Further studies [46] have been performed with cosmic-rays comparing the three basic momentum measurements: Muon Spectrometer (MS), Inner Detector (ID) and combined (CB) reconstruction algorithms. As discussed in Section 3.5 the MS and ID algorithms perform independent measurements of the muon track parameters. The CB algorithm uses the MS and ID tracks as input and performs a refit. Figure 4.11 shows the final result for $\sigma(p_T)/p_T$ of these studies, again for the barrel region only due to limited statistics in the endcaps. The data is fitted according to Equations 4.4, 4.5 and 4.6 for MS, ID and CB algorithms, respectively.

$$\frac{\sigma_{p_T}}{p_T} = P_1 \oplus P_2 \cdot p_T \tag{4.5}$$

$$\frac{\sigma_{p_T}}{p_T} = \frac{P_0 \cdot p_T}{\sqrt{1 + (P_3 \cdot p_T)^2}} \oplus P_1 \oplus P_2 \cdot p_T \tag{4.6}$$

P_0, P_1 and P_2 are defined as before and P_3 is needed for a correct description of the intermediate region where MS and ID resolutions are comparable.

From Figure 4.11 it can be seen that the ID provides the best resolution (about 2%) for the region below 40 GeV. This is expected because of the high resolution detector components that can measure soft (muon) tracks with high precision. Above 100 GeV the MS provides the best resolution measurement because of its larger bending power.

The obtained ID momentum resolution from cosmic-ray data is in fair agreement with previous studies using single muon tracks reconstructed with the aimed final calibration and perfect alignment [50]. The obtained MS momentum resolution, and the reasonable agreement with expectation at low-p_T and disagreement at high-p_T, was already discussed in Section 4.5.

In all p_T regions it can be observed that the CB follows the best available resolution measurement, as it is designed (and thus expected) to do. In the intermediate region the ID and MS contribute equally to the CB resolution. For example, at 90 GeV the individual ID and MS resolutions are 5% and 4.5% respectively. One thus expects the CB resolution to be about $1/\sqrt{(1/0.05)^2 + (1/0.045)^2} \approx 3.34\%$ which is approximately what we observe in Figure 4.11. The intermediate region is of particular interest to the $Z \rightarrow \mu^-\mu^+$ studies which will be further discussed in Chapter 5.

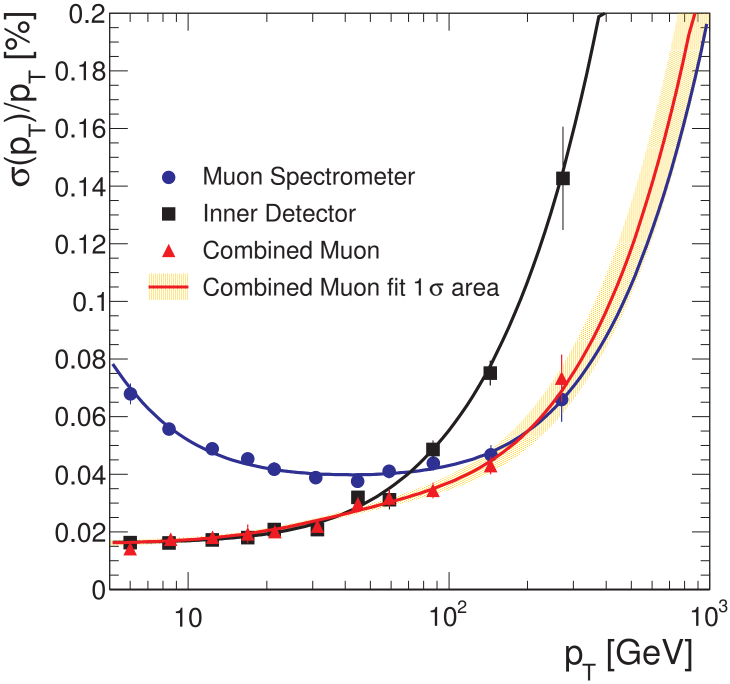

Figure 4.11: Fitted values for $\sigma(p_T)/p_T$ for MS (circles), ID (squares) and CB muons (triangles). All curves are fitted as described in the text.

4.7 Summary

The performance of the ATLAS Muon Spectrometer has been studied using cosmic-ray muons. Two complementary methods have been presented in this chapter. The results of the sagitta analysis and the momentum resolution analysis are in agreement.

Both studies show a higher multiple scattering term in data, indicating a material budget deficit of about $10-15\%$ in simulation/calculation. Further studies are needed to improve the understanding of the ATLAS material budget.

In addition, both analyses show an intrinsic resolution term that is higher in data than in simulation/calculation. This higher intrinsic resolution term causes the MS momentum resolution in data to be significantly higher than expected for $p_T > 50$ GeV. This indicates that there is quite some gain to be expected from improving the understanding of the various contributions to the intrinsic resolution term, including for example the magnetic field description and alignment.

The cosmic-ray data were extensively used for obtaining a good understanding of the ATLAS Muon Spectrometer. Already before the first proton-proton collision the performance of the Muon Spectrometer was shown to be good and in fair agreement with expectations for $p_T < 40$ GeV.

Chapter 5

Performance of the Muon Spectrometer with collision data

5

5.1 Introduction

After the commissioning phase with cosmic-ray muons, discussed in Chapter 4, the LHC started to deliver stable proton beams from November 2009 onwards. First proton-proton (pp) collisions were recorded at injection energy of 900 GeV. After a short run at 2.36 TeV the collision energy was ramped up to 7 TeV, half of the nominal value of the LHC but still 3.5 times more energetic than the Tevatron.

On the 30^{th} of March 2010 first collisions at 7 TeV were recorded and immediately the first muons from collisions were observed. In May 2010 the first $Z \to \mu\mu$ events[1] were recorded, one of the many di-muon resonances observed in the 2010 data-set. Figure 5.1 shows a spectrum of di-muon invariant masses observed in 2010 ATLAS data. Events in this plot are triggered by the presence of a muon above 15 GeV at the Event Filter trigger stage (cf. Section 3.2). The two muons are reconstructed by the `Muid` combined muon algorithm [38]. They have to be of opposite charge and the second muon, i.e. the muon that did not trigger the event, is required to have $p_T > 2.5$ GeV. In Figure 5.1 several well known particles can be identified. The peak around 91 GeV is of particular interest for this thesis as this is the region were we expect to observe Z bosons.

The muon reconstruction performance can be studied using $Z \to \mu\mu$ decays. We will discuss two studies. First a method to determine muon reconstruction efficiencies is discussed in Section 5.2. Afterwards a method to extract the muon momentum resolution is addressed in Section 5.3. Both methods provide important input for physics analyses using muons, like the ones that will be discussed in the next chapters.

5.2 Muon reconstruction efficiency

5.2.1 Tag and probe method

We apply a tag and probe method, using the well known Z boson to measure the muon reconstruction efficiency in a data-driven manner.

[1] We refer to $Z \to \mu^-\mu^+$ in this chapter without noting the opposite muon charges on every occasion.

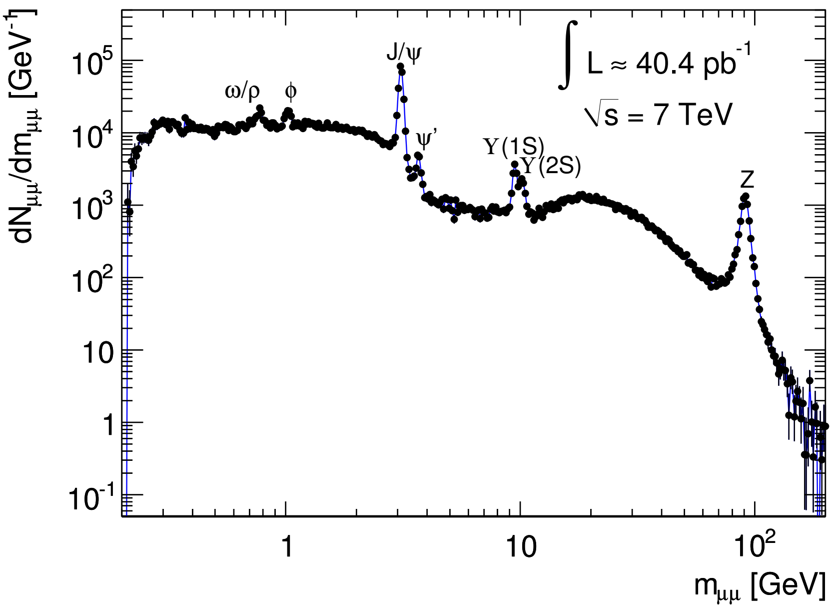

Figure 5.1: Di-muon invariant mass spectrum observed in the ATLAS 2010 data.

Consider the (fictitious) muon reconstruction algorithm A. To evaluate the efficiency of algorithm A with our tag and probe method we do the following:

- select a reconstructed muon to be our *tag*. Any reconstruction algorithm can be used for the tag muon but it needs to have triggered the event. This prevents a bias from trigger efficiencies;
- select another reconstructed muon to be our *probe*. The reconstruction algorithm of the probe muon should be independent of algorithm A and should cover the full $\eta - \phi$ acceptance of algorithm A;
- apply selections to the muon pair (e.g. opposite sign and invariant mass);
- count the number of times that algorithm A finds (N_f) and misses (N_m) the probe;
- compute the algorithm efficiency to be $\epsilon_A = N_f/(N_f + N_m)$.

This is the tag and probe method in a very general form. The requirements on the tag and the probe muon as applied in the presented analysis will be discussed below.

Tag muon requirements

A tag muon is required to be a combined muon passing several kinematic and track quality cuts. It is also required to have triggered the event, where the trigger requirement depends on the run number to which the event belongs.

The tag muon must have a $p_T > 20$ GeV and a polar angle that lies within the muon trigger acceptance, i.e. $|\eta| < 2.4$. Its longitudinal distance with respect to the primary vertex in the event should be less than 10 mm. The muon is required to be isolated from other tracks in the inner detector. The relative track isolation is determined by summing the p_T of all tracks that are in a cone of $\Delta R < 0.4$ around the muon track and dividing this sum by the muon p_T:

$$\mathrm{iso}_{\mathrm{track}} = \left(\sum_{\Delta R < 0.4} p_T \right) / p_T. \tag{5.1}$$

The muon track is excluded from the sum. If $\mathrm{iso}_{\mathrm{track}} < 0.2$, the muon is accepted.

In addition to the kinematic cuts Inner Detector track quality selections are applied:

- at least one hit in the inner Pixel layer;
- at least two Pixel hits in total;
- at least six SCT hits;
- at most 3 SCT+Pixel holes;
- the number of TRT outliers[2] should be less than 90% of the sum of hits and outliers in the TRT.

Dead modules and detector acceptances are taken into account in the track quality selections.

Probe muon requirements

The probe muon is required to be an Inner Detector track tagged by the calorimeter (cf. Section 3.5.4). Since this calorimeter tagged algorithm is independent of other muon reconstruction algorithms, this allows for an unbiased determination of the efficiency of these other algorithms. The same kinematic and isolation selections as applied to the tag muon are applied to the calorimeter probe muon. The only exception is the requirement on η. The allowed region is enlarged to $|\eta| < 2.5$ to match the Inner Detector acceptance.

The probe muon has to be of opposite charge sign compared to the tag muon, where the sign is taken from the Inner Detector measurement. The invariant mass of the two muons is required to be within 10 GeV of the world average value of the Z boson mass, which is 91.1876 GeV [15]. The Inner Detector measurements are used for the invariant mass calculation. A probe muon is then tested to have been reconstructed by the algorithm under study. We will show results for different categories: combined muons, tight muons and medium muons. The combined muons have been addressed in Section 3.5. The tight and medium muons require some further introduction.

[2]Outliers are hits on track that result in a bad fit but can still be used for particle identification.

Whereas *combined* refers to the algorithm used for reconstruction, *tight* and *medium* refer to quality definitions used to classify muons for physics analysis users [51]. A tight muon passes the most strict requirements in terms of the balance between efficiency and fake rate. Tight muons represent the category of highest quality muons for physics analysis. The medium muons have a higher efficiency and slightly higher fake rate than the tight muons. A third category exists, the *loose* muons, but this is not studied here.

The results presented in this thesis use the following muon quality definitions:

- **Tight -** this is a collection of combined muons, standalone muons at $\eta > 2.5$ and `MuGirl` [52] muons. The latter is an algorithm that matches an Inner Detector track to Muon Spectrometer hits, from which it builds muon segments, and subsequently performs a full refit of the track. Only the `MuGirl` muons with a successful refit are added to the tight category;
- **Medium -** these are tight muons with the addition of standalone muons from all η regions and `MuGirl` muons without a successful refit, i.e. segment tagged muons;
- **Loose -** these are medium muons with a last addition of the segment tagged muons from the other `Muid` segment tag algorithm (`MuTagIMO`).

The track quality cuts effectively remove the standalone muons because no Inner Detector track is associated to this type of muons.

5.2.2 Data-set and event selection

We present results for the tag and probe analysis with the full 2010 LHC data-set, corresponding to an integrated luminosity of about 40 pb^{-1}. The data-set is divided in periods labeled A to I. Trigger requirements depend on the period of data taking. For periods A to D a muon trigger of $p_T > 10$ GeV is required at L1. A muon trigger of $p_T > 10$ GeV is required at the Event Filter for periods E and F. In the periods G to I a muon trigger of $p_T > 13$ GeV is required at the Event Filter.

The event selection is simply the presence of a tag and a probe muon in the event. These have to pass the requirements as discussed before. After these selections we are left with about 20,000 muon pairs in data.

A simulated sample of $Z \rightarrow \mu\mu$ decays from `PYTHIA`[3] is used for comparison studies. The same requirements were applied on simulation as on data except for the trigger requirement. In the simulation a muon trigger of $p_T > 10$ GeV is required at L1.

5.2.3 Results

Figure 5.2 shows the invariant mass distribution of the muon pairs in data that pass the tag and probe muon requirements. The Inner Detector track parameters are used in the mass calculation. The selection on invariant mass of the two muons has not been applied in this plot. Opposite sign pairs show a clear peak around the Z boson mass. Same sign pairs constitute a background of only about 0.1% within 10 GeV of the peak.

[3] `mc10_7TeV.106047.PythiaZmumu_no_filter.recon.ESD.e574_s933_s946_r2215`

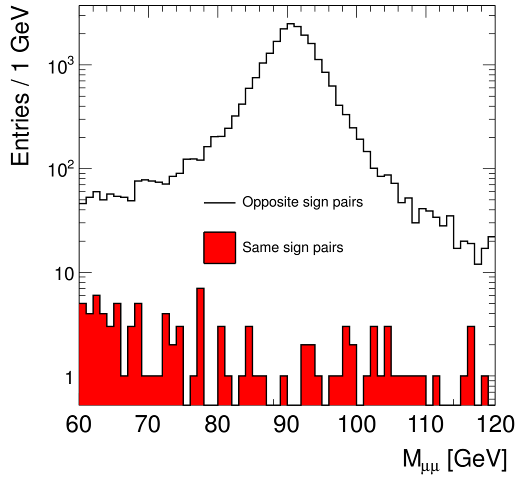

Figure 5.2: Invariant mass of muon pairs in data passing tag and probe requirements.

The efficiency is studied as a function of η and p_T. Ten symmetric bins in η are chosen to follow the Muon Spectrometer layout. The binning in $|\eta| = [0, 0.1, 1.05, 1.7, 2.0, 2.5]$ subsequently defines the crack region, the barrel region, the transition region, the endcap region and the CSC region. At $0 < |\eta| < 0.1$ there is a crack in the Muon Spectrometer acceptance so we treat this region separately. Eight bins in p_T are defined in the region $[20, 100]$ GeV. Six of them have a width of 5 GeV. The two highest p_T bins have a width of 10 and 40 GeV, respectively. Figure 5.3 shows the η and p_T distributions for the selected probes in data and simulation. A good agreement in η and p_T is observed.

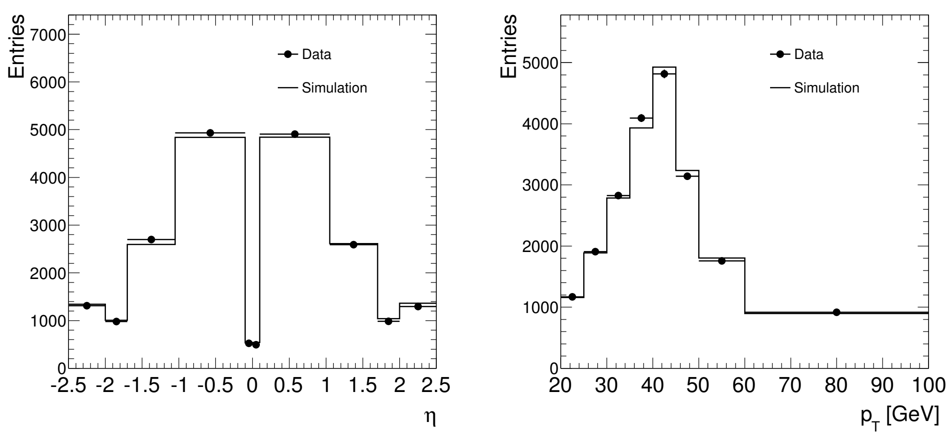

Figure 5.3: Normalized distributions of η and p_T for probe muons.

Figures 5.4 and 5.5 show the efficiencies measured in data and simulation for combined and tight muons, respectively. The small losses of efficiency in data for combined muons observed in the transition regions and positive endcap region are recovered in the tight muon results. The inefficiency observed around $|\eta| \approx 0$ is partly recovered by the tight muons. One does not expect the efficiency in this region to get significantly closer to 1 due to limited hardware coverage of the Muon Spectrometer in this region.

Table 5.1 summarizes the results for the η integrated efficiencies in the three studied cases. Scale factors are also computed for these integrated efficiencies and are listed in the table. In all cases the computed scale factor is close to one, indicating no significant differences between data and simulation samples. ATLAS has presented results quoting an efficiency of 0.958$\pm$0.001 and 0.980$\pm$0.001 for combined and tight muons, respectively [53,54]. For these results Inner Detector tracks are used as the probe muon. Nevertheless, these results are in good agreement with our results.

The difference in efficiency for combined and tight muons in data is on average about 1.7%. The use of tight muons is therefore interesting for physics analyses with multiple muons in the final state. For example, in the so-called golden channel for Higgs discovery $H \to ZZ^{(*)} \to \mu^-\mu^+\mu^-\mu^+$ a gain of about 6.5% would be possible when both Z bosons are on-shell. For analyses with one or more muons with $p_T < 20$ GeV the medium muons could add to the analysis since the muon tagger algorithms are designed to recover muons at low-p_T. However, for each analysis it will be important to study the trade off between an increase of efficiency (or signal) and a possible increase in fake rate (or background).

5

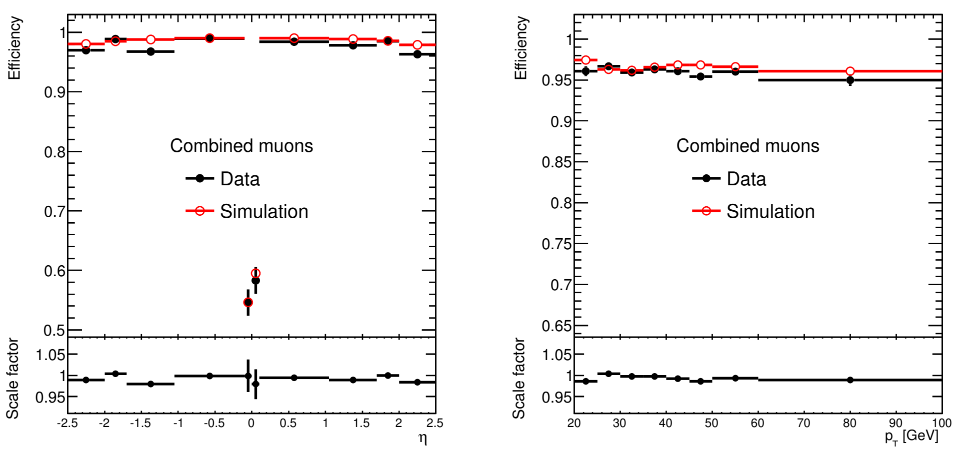

Figure 5.4: Efficiency of combined muons in data and simulation.

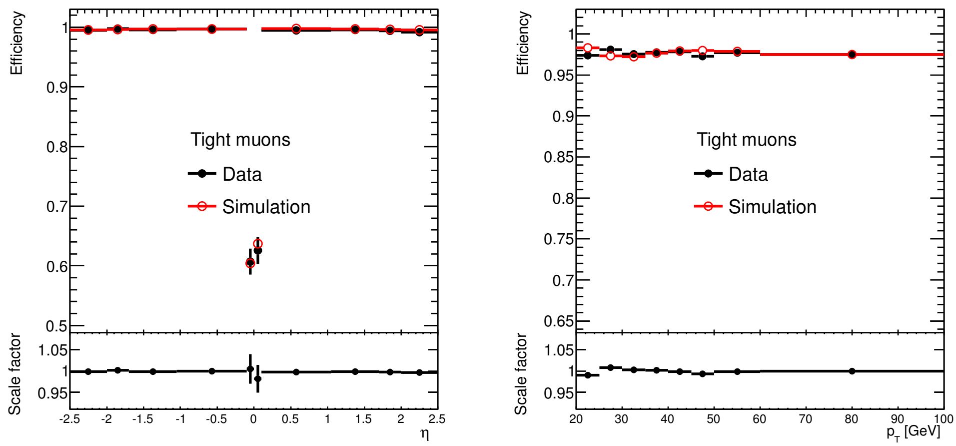

Figure 5.5: Efficiency of tight muons in data and simulation.

Muon type	Data	Simulation	Scale factor
Combined	0.960 ± 0.003	0.966 ± 0.002	0.994 ± 0.004
Tight	0.977 ± 0.003	0.977 ± 0.002	0.999 ± 0.003
Medium	0.979 ± 0.003	0.979 ± 0.002	1.000 ± 0.003

Table 5.1: Integrated efficiencies for muons in data and simulation.

5

Systematic uncertainties

Systematic uncertainties are studied on the simulated $Z \to \mu\mu$ sample by varying the selections on the di-muon invariant mass window, on muon p_T and on relative track isolation. The mass window is set to ± 8 GeV and ± 12 GeV of the world average value. The minimum value for the muon p_T is set to 15 GeV and 25 GeV. The relative track isolation, $\text{iso}_{\text{track}}$ (cf. Equation 5.1), is required to be smaller than 0.15 and 0.25.

Table 5.2 quotes the largest observed deviations (in %) per variable. The total systematic error is computed as the quadratic sum of the individual contributions. The η integrated systematic error is found to be 0.073%. An uncertainty of 0.1% is added to this to account for backgrounds (cf. Figure 5.2), resulting in a total systematic error of 0.173% for our method. The total systematic error and the statistical error in data are comparable in size for the η integrated results. ATLAS results quote a systematic error of 0.2% on the scale factor [53, 54], which is in agreement with our findings.

For the efficiency results as a function of η the systematic errors are added in quadrature to the statistical errors in each bin. For the results as a function of p_T we take the integrated systematic error and add this to the the statistical error in each bin. Figures 5.4 and 5.5 and Table 5.1 show the results after addition of the systematic errors.

η region	Data stat. error	Total syst. error	Systematic error from mass window	muon p_T	muon isolation
$[-2.5, -2.0]$	0.484	0.050	0.040	0.030	0.003
$[-2.0, -1.7]$	0.340	0.037	0.025	0.026	0.009
$[-1.7, -1.05]$	0.352	0.042	0.015	0.039	0.005
$[-1.05, -0.1]$	0.147	0.017	0.004	0.015	0.006
$[-0.1, 0]$	3.985	0.408	0.010	0.382	0.144
$[0, 0.1]$	3.805	0.717	0.212	0.682	0.062
$[0.1, 1, 05]$	0.179	0.017	0.014	0.009	0.002
$[1.05, 1.7]$	0.294	0.038	0.014	0.034	0.010
$[1.7, 2.0]$	0.397	0.050	0.047	0.017	0.004
$[2.0, 2.5]$	0.546	0.031	0.022	0.022	0.004
η integrated	0.142	0.073	0.006	0.073	0.005

Table 5.2: Systematic errors (%) for the presented efficiency measurements.

5

5.3 Muon momentum resolution studies

The muon momentum resolution is studied using $Z \to \mu\mu$ decays. The di-muon invariant mass lineshape as discussed in Section 2.3.3 is applied to the 2010 LHC data-set. Equation 2.21 is simplified to the following formula for the lineshape

$$N(x) = A\frac{1}{x^2} + B\frac{x^2 - M_Z^2}{(x^2 - M_Z^2)^2 + \Gamma_Z^2 M_Z^2} + C\frac{x^2}{(x^2 - M_Z^2)^2 + \Gamma_Z^2 M_Z^2}, \tag{5.2}$$

where x represents the di-muon invariant mass. This is a good approximation for the energy available in this process.

The `ROOFIT` fitting package [55] is used to perform our maximum likelihood fits. The fit parameters are fixed to the following values:

- M_Z and Γ_Z are fixed to their world average values of 91.1876 GeV and 2.4952 GeV, respectively [15];
- C is fixed to 1.

$N(x)$ is fitted to the lineshape at event generator level, leaving A and B as floating parameters in the fit. This gives a description of the *theoretical* Z lineshape. Form factors for the photon and Z boson are not taken into account in Equation 5.2. Figure 5.6 shows the lineshape after a fit at generator level and gives the fitted values for A and B. The successful fit to simulation indicates that the overall multiplicative factors from the form factors are not dominant for the shape of the invariant mass distribution. We therefore use Equation 5.2 as our lineshape parametrization.

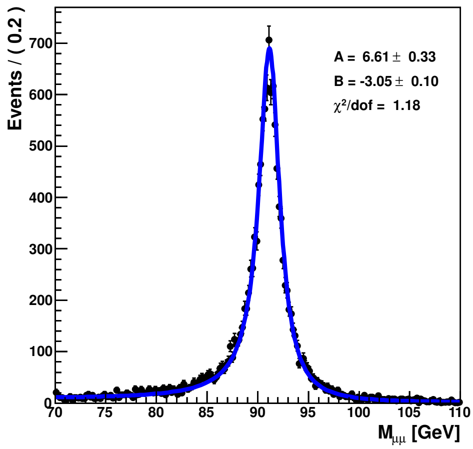

Figure 5.6: A fit of Equation 5.2 to the simulation at generator level.

5

Analyzing LHC data requires the inclusion of detector effects in our lineshape description. These effects are modeled by a double Gaussian function. The double Gaussian is chosen for the same reasons as in Chapter 4: a narrow Gaussian describes the core momentum resolution, a broad Gaussian describes the tails. This was studied in the context of the errors assigned to a muon track. The double Gaussian description showed a clear improvement compared to a single Gaussian description. Adding a third Gaussian slightly improves the description but implementing the third Gaussian in our $Z \to \mu\mu$ study resulted in unstable fits. The double Gaussian was thus chosen as the preferred description and adapted by the ATLAS Muon Combined Performance group [56].

The two Gaussian functions were given a common mean value, μ, that is fixed to 0. The value for σ of the broader Gaussian is fixed to twice the value for the narrow Gaussian. The ratio of the two Gaussians is fixed to 0.85, a value following from the muon track error studies mentioned above.

The double Gaussian is convoluted with $N(x)$ to get the *measured* lineshape $N_M(x)$:

$$N_M(x) = N(x) \otimes \left[\frac{0.85}{\sqrt{2\pi\sigma^2}} \cdot \exp\left(-\frac{x^2}{2\sigma^2}\right) + \frac{0.15}{\sqrt{2\pi(2\sigma)^2}} \cdot \exp\left(-\frac{x^2}{2(2\sigma)^2}\right)\right]. \qquad (5.3)$$

Fitting $N_M(x)$ to data is done as follows:

- A and B are fixed to the above obtained values and C is fixed to 1;
- Γ_Z is fixed to 2.4952 GeV;
- an unbinned fit is performed to data with M_Z and σ as floating parameters.

As M_Z is now a floating parameter we prefer to note it as $M_{\mu\mu}$ for fits to data. The resulting values for $M_{\mu\mu}$ and σ are a measure for the momentum scale and resolution.

5

5.3.1 Event selection

A pair of oppositely charged combined muons is required in the event. Both muons must have $p_T > 20$ GeV and pass Inner Detector track quality requirements (cf. Section 5.2). This selects about 15k and 230k muon pairs for data and simulation, respectively.

5.3.2 Results

For each muon pair a comparison is made between the reconstructed invariant mass using combined muon parameters (CB parameters), standalone muon parameters (SA parameters) and Inner Detector track parameters (ID parameters). The same binning as in Section 5.2 in η is chosen. Figure 5.7 shows two example fits using combined parameters for muon pairs in the barrel region. The fitted values for $M_{\mu\mu}$ and the Gaussian σ are displayed in the plot.

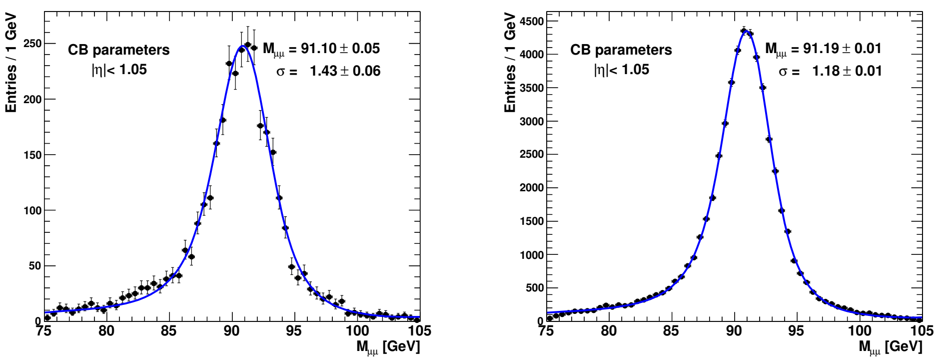

Figure 5.7: Fitted distributions for (a) data and (b) simulation.

Figures 5.8, 5.9 and 5.10 show the results for the momentum scale and resolution as a function of the η region where both muons are detected. The momentum scale is defined as the relative difference between the fitted value $M_{\mu\mu}$ and the world average. Nonzero scale values indicate systematic shifts in the measured muon momenta.

The scales of the CB, SA and ID parameters are within 1% over the full η range. For the CB parameters an asymmetry between positive and negative endcap regions is observed. This asymmetry is also visible in the scale of the ID parameters, but is not visible in the scale of the SA parameters. For the latter the scale in the barrel region is statistically compatible with simulation.

The resolution for CB, SA and ID parameters is larger in data than in simulation. The barrel region has the best resolution in all cases. For the CB and ID parameters a clear asymmetry between positive and negative endcaps is visible.

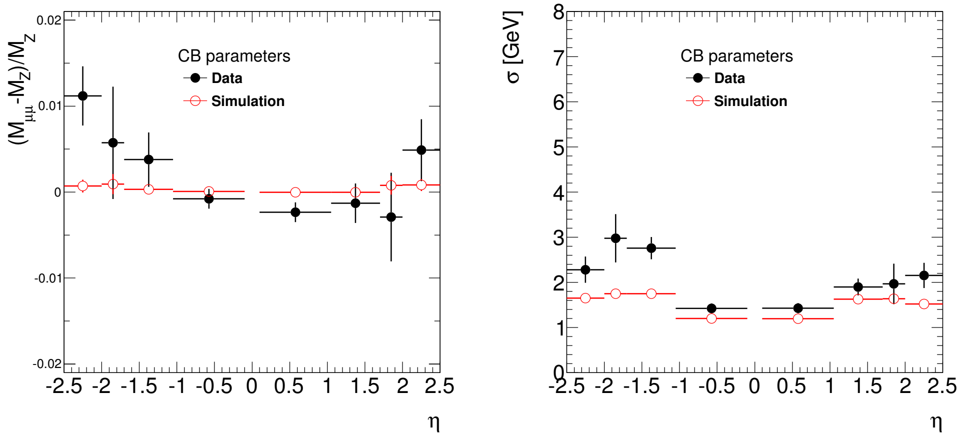

(a) (b)

Figure 5.8: Fitted (a) scale and (b) resolution for selected muon pairs using combined muon parameters.

5

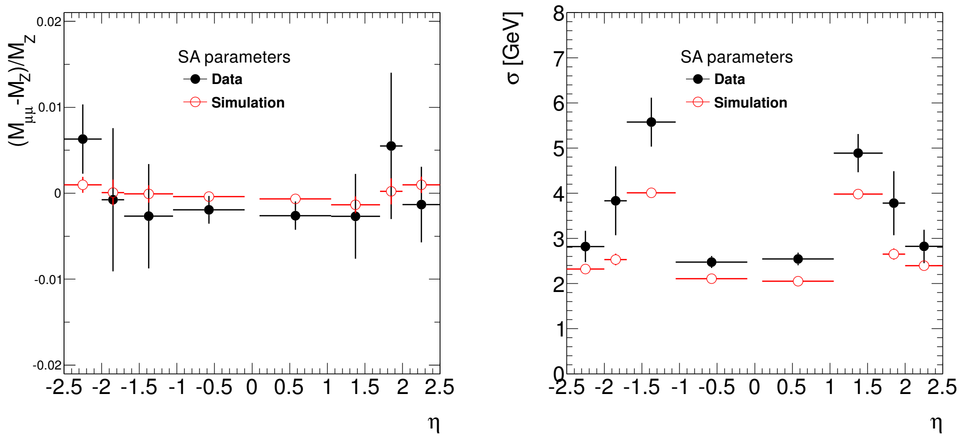

(a) (b)

Figure 5.9: Fitted (a) scale and (b) resolution for selected muon pairs using standalone muon parameters.

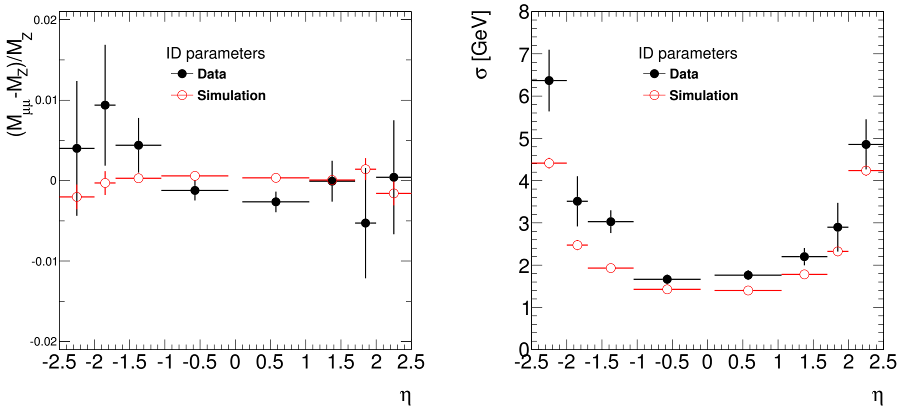

(a) (b)

Figure 5.10: Fitted (a) scale and (b) resolution for selected muon pairs using Inner Detector track parameters.

5

Interpretation

The observed asymmetry in the momentum scale for ID parameters is attributed to be mainly an effect of a *curl* weak mode misalignment[4] [57, 58]. This has an opposite effect on the momentum scale for the positive and negative endcaps. In addition to this, during reconstruction a symmetric magnetic field description is used while there is in fact an asymmetric field. Improved magnetic field descriptions have been provided but were not included in our studies [59]. Misalignments are not expected to have an effect on the momentum scale as they have an opposite effect on positive and negative muons.

A discrepancy over the full η range between data and simulation is observed in our resolution results for SA, ID and CB parameters. For SA parameters this is partially due to missing passive material in the detector description used in the simulation. As mentioned in Chapter 4, missing detector material is added to the detector description for simulation [49]. This is still ongoing work at the time of writing. For ID parameters the discrepancy is due to remaining misalignment of the Inner Detector. This was not yet corrected for in the `ATHENA` release used for the reconstruction of our results[5]. More recent results do not show this asymmetric feature anymore (see e.g. ref. [60]). The resolution from CB parameters suffers from both these effects.

Comparison to cosmic-ray data results

For all parameters (CB, SA and ID) the barrel region shows the best scale and resolution. The resolution for CB parameters in the barrel region is about 1.4 GeV in data. This

[4] A *weak mode* refers to a misalignment without much effect on χ^2 based alignment techniques. The *curl* weak mode indicates a shift in ϕ which is proportional to the radial distance R.

[5] Shown reconstruction was performed with release 16.6.2.31 of `AtlasProduction`.

is compatible with our results from cosmic-ray data taking: the value 1.4 needs to be multiplied by 1.15 because of our double Gaussian description of the detector resolution[6]. Then we need to take into account the p_T of the two muons. Unfortunately there were too little statistics to study the resolution as a function of muon p_T, as we did for the cosmic-ray data. However, if we make the assumption that both muons have $p_T = 40$ GeV (cf. Figure 5.3(b)) we can make a quantitative comparison to our cosmic-ray data results from Section 4.6. In this case $\sigma(M_Z) = \sqrt{2} \cdot \sigma(p_T)$ and we obtain $\sigma(p_T) = 1.4 \cdot 1.15/\sqrt{2} = 1.14$ GeV. For a muon with $p_T = 40$ GeV this implies a relative resolution $\sigma(p_T)/p_T = 1.14/40 \cdot 100\% = 2.8\%$, compatible with our cosmic-ray data results.

Misalignment

The momentum resolution contains various contributions (cf. Chapter 4). We have seen that the (missing) material description in the Muon Spectrometer and misalignments in the Inner Detector play a big role. However, the resolution results presented above show the net effect of both contributions. One possibility to disentangle the alignment contribution is by looking at the distribution of $1/p_T$ for negative and positive muons separately. In contrast to material interactions, misalignments are expected to have an opposite effect on the momentum measurement of positive and negative muons. A certain chamber misalignment will overestimate (underestimate) the curvature of a negative (positive) muon, or vice versa.

Figure 5.11 shows the difference in the average $1/p_T$ between positive and negative muons, for CB, SA and ID parameters. All plots show discrepancies with simulation around $\eta = 1.5$. For the ID parameters this is attributed to the remaining misalignments mentioned before. The SA parameters show discrepancies at $\eta = \pm 1.5$. This is the transition region between barrel and endcap where BEE and EEL/EES chambers are installed (cf. Section 3.4.3). These chambers were not yet aligned during reconstruction of our data-set. In addition barrel-endcap misalignments contribute in this region. A discrepancy is also visible in the CSC region at negative η. The CSC misalignments are confirmed by other studies and new alignment constants have been implemented recently [61].

Expected momentum resolution for a muon with a p_T of 1 TeV

From Figure 5.11 we can read off the expected muon momentum resolution from misalignments, which is the dominant contribution at 1 TeV. At 1 TeV the standalone measurement of the momentum resolution is required to be 10%. From Figure 5.11(b) we can read off a value of about $2 \cdot 10^{-4}$ GeV^{-1}, corresponding to 20% at 1 TeV, for SA parameters in the barrel region. This is obviously not yet the required resolution. However, it is in agreement with the intrinsic resolution term obtained in our cosmic-ray data results (cf. P_2 in Table 4.3).

[6]Coming from the fixed fractions and size of second sigma $\rightarrow 0.85 \cdot \sigma + 0.15 \cdot (2\sigma) = 1.15\sigma$.

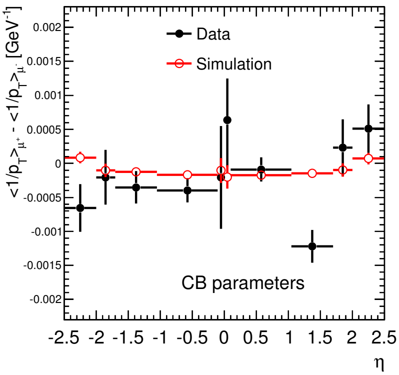

(a)

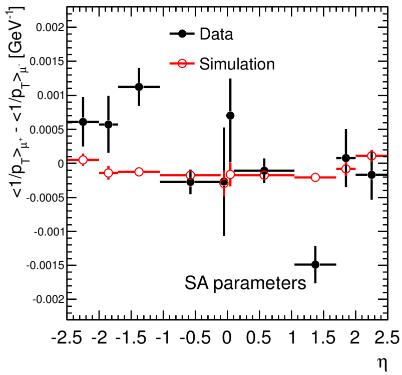

(b)

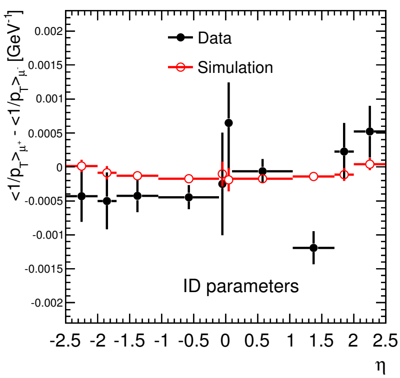

(c)

Figure 5.11: $< 1/p_T >_{\mu^+} - < 1/p_T >_{\mu^-}$ for (a) combined, (b) standalone and (c) Inner Detector parameters. Data is shown as filled points, simulation as open points.

5.4 Conclusions

From the first day onwards muons from proton-proton collisions were reconstructed and used in performance studies. In this chapter we have discussed two methods using muon pairs originating from the decay of Z bosons in ATLAS. Z boson decays like the one shown in Figure 5.12 have been exploited to determine the muon reconstruction efficiency and momentum resolution.

The efficiency was studied using a tag and probe method. For the category of *tight* muons an efficiency of 0.977 ± 0.003 was measured in the 2010 LHC data-set and found to be compatible with simulation. Following this and other results, tight muons are recommended to be used for physics analyses in ATLAS for the 2011 data. We will discuss an example of such an analysis in Chapter 7.

The momentum scale and resolution were studied in different detector regions. A theoretical description of the di-muon invariant mass distribution, or lineshape, was obtained from simulation and applied to data. The detector description was modeled using a double Gaussian.

The momentum scale was studied for CB, SA and ID parameters and found to be within 1% and 0.5% for the endcap and barrel regions, respectively.

The resolution for CB parameters in the barrel region was found to be 1.4 (1.2) GeV for data (simulation). For SA and ID parameters the obtained values in the barrel region are 2.5 (2.1) GeV and 1.7 (1.4) GeV, respectively. The derived results are consistent with the results from cosmic-ray data taking.

Misalignments were studied using $1/p_T$ distributions for positive and negative muons separately. Remaining Inner Detector misalignments were located to the region around $\eta = 1.5$. Muon Spectrometer misalignments were observed in the transition region, $|\eta| = [1.05, 1.7]$ and in the CSC region for negative η. The misalignment in both transition regions is due to misaligned BEE and EEL/EES stations in these regions. Both sources of misalignment were confirmed by other studies and have been corrected for in recent updates of the alignment constants.

In summary, the results presented in this chapter demonstrate the good performance of the Muon Spectrometer in collision data. Our results proved to be important for improving the understanding of the magnetic field description, the detector material and the alignment. While similar studies are still being performed, the confidence in the good performance allows the pursuit of interesting physics analyses. An example of such an analysis is given in the next chapter, in the context of heavy-ion collisions.

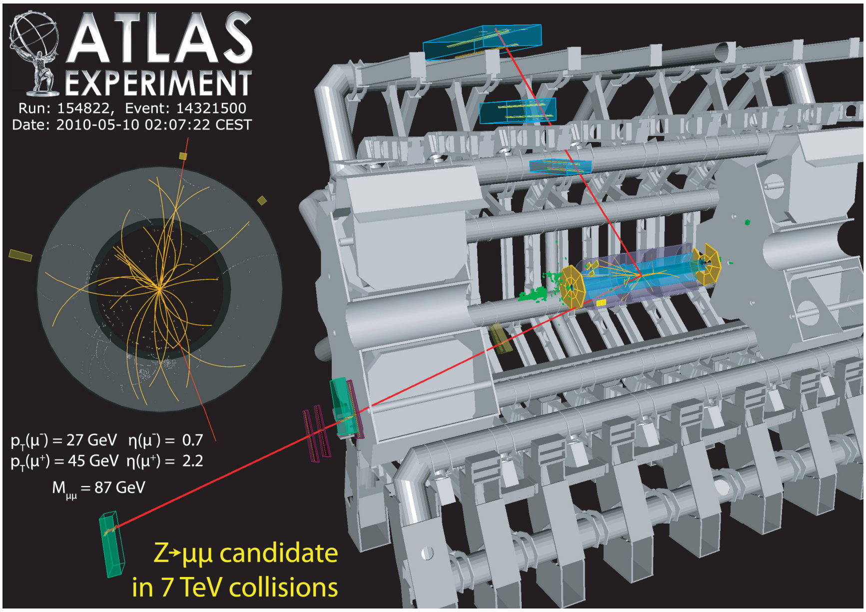

Figure 5.12: Event display of one of the first $Z \to \mu\mu$ candidates observed in ATLAS.

Chapter 6

Observation of $Z \rightarrow \mu^-\mu^+$ in $PbPb$ collisions at $\sqrt{s_{NN}} = 2.76$ TeV

The LHC heavy-ion programme

In addition to protons also heavy-ions are collided in the LHC. These collisions are scheduled for about one month per year, in the absence of proton-proton collisions. Each heavy-ion is composed of individual nucleons, i.e. protons and neutrons. The design nucleon-nucleon center of mass energy is $\sqrt{s_{NN}} = 5.5$ TeV, which exceeds that of the previous generation of heavy-ion colliders such as RHIC [62] by a factor 30. ALICE [63] is the experiment at the LHC dedicated to heavy-ion collisions but ATLAS and CMS also perform heavy-ion studies.

6

The LHC heavy-ion programme started in November 2010 when first lead-lead ($PbPb$) collisions were recorded at $\sqrt{s_{NN}} = 2.76$ TeV. Figure 6.1 shows the total accumulated luminosity by ATLAS in the 2010 heavy-ion physics run of the LHC.

Heavy-ion collisions provide an interesting experimental environment to study di-muon final states, such as those resulting from the decays of J/ψ's and Z bosons. The ATLAS collaboration has studied J/ψ's and Z di-muon decays in heavy-ion collisions and has published the results in Physics Letters B [64]. The published result is shown in the following pages. I have contributed to all the muon studies for this publication and to the final results of the J/ψ and Z yield as a function of centrality.

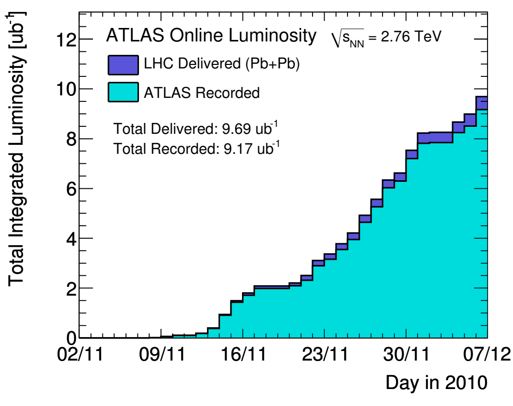

Figure 6.1: The accumulated luminosity for $PbPb$ collisions within ATLAS in 2010.

Measurement of the centrality dependence of J/ψ yields and observation of Z production in lead-lead collisions with the ATLAS detector at the LHC

G. Aad *et al.* (The ATLAS Collaboration),

6

Abstract

Using the ATLAS detector, a centrality-dependent suppression has been observed in the yield of J/ψ mesons produced in the collisions of lead ions at the Large Hadron Collider. In a sample of minimum-bias lead-lead collisions at a nucleon-nucleon centre of mass energy $\sqrt{s_{NN}} = 2.76$ TeV, corresponding to an integrated luminosity of about 6.7 μb^{-1}, J/ψ mesons are reconstructed via their decays to $\mu^+\mu^-$ pairs. The measured J/ψ yield, normalized to the number of binary nucleon-nucleon collisions, is found to significantly decrease from peripheral to central collisions. The centrality dependence is found to be qualitatively similar to the trends observed at previous, lower energy experiments. The same sample is used to reconstruct Z bosons in the $\mu^+\mu^-$ final state, and a total of 38 candidates are selected in the mass window of 66 to 116 GeV. The relative Z yields as a function of centrality are also presented, although no conclusion can be inferred about their scaling with the number of binary collisions, because of limited statistics. This analysis provides the first results on J/ψ and Z production in lead-lead collisions at the LHC.

Keywords: ATLAS, LHC, Heavy Ions, J/psi, Z Boson, Centrality dependence

1. Introduction

The measurement of quarkonia production in ultra-relativistic heavy ion collisions provides a potentially powerful tool for studying the properties of hot and dense matter created in these collisions. If deconfined matter is indeed formed, then colour screening is expected to prevent the formation of quarkonium states when the screening length becomes shorter than the

Preprint submitted to Elsevier *December 27, 2010*

quarkonium size [1]. Since this length is directly related to the temperature, a measurement of a suppressed quarkonium yield may provide direct experimental sensitivity to the temperature of the medium created in high energy nuclear collisions [2].

The interpretation of J/ψ suppression in terms of colour screening is generally complicated by the quantitative agreement between the overall levels of J/ψ suppression measured by the NA50 experiment at the CERN SPS [3] ($\sqrt{s_{NN}} = 17.3$ GeV) and the PHENIX experiment at RHIC [4] ($\sqrt{s_{NN}} = 200$ GeV). Data from proton-nucleus and deuteron-gold collisions also show decreased rates of J/ψ production [5], indicating that other mechanisms may come into play. Finally, there exist proposals for J/ψ *enhancement* at high energies from charm quark recombination [6]. Measurements at higher energies, with concomitantly higher temperatures and heavy quark production rates, are clearly needed to address these debates with new experimental input. The production of Z bosons, only available in heavy ion collisions at LHC energies, can serve as a reference process for J/ψ production, since Z's are not expected to be affected by the hot, dense medium, although modifications to the nuclear parton distribution functions must be considered [7].

The LHC heavy ion program, which commenced in November 2010, offers an opportunity to measure J/ψ and Z production in nuclear collisions at the highest energies ever achieved. The ATLAS detector provides excellent muon detection capabilities down to momenta of about 3 GeV, and J/ψ mesons and Z bosons can be readily detected via their decays to $\mu^+\mu^-$ final states. This Letter presents the first measurements of the relative yields of J/ψ meson and Z boson decays in lead-lead collisions at a nucleon-nucleon center of mass energy of $\sqrt{s_{NN}} = 2.76$ TeV. The yields are measured in four bins of collision centrality, and the variation of the yields with centrality is compared to the dependence expected if hard scattering processes scale according to expectations from nuclear geometry. No attempts are made to account for "normal nuclear suppression" [3], nor for feed-down of J/ψ from higher mass charmonium states or B hadron decay.

2. Di–muon event selection

Muons are measured by combining independent measurements of the muon trajectories from the Inner Detector (ID) and the Muon Spectrometer (MS). A detailed description of these detectors and their performance in proton-proton collisions can be found in Refs. [8, 9]. The ID volume is within the 2 T field of a superconducting solenoid, and measures the trajectories of charged particles in the pseudorapidity region $|\eta| < 2.5$ [1]. A charged particle typically traverses three layers of silicon pixel detectors, eight silicon strip sensors (SCT detector) arranged in four layers of double-sided modules, and a transition radiation tracker composed of straw tubes. The MS surrounds the calorimeters and provides tracking for muons with $|\eta| < 2.7$ and triggering in the range $|\eta| < 2.4$. The muon momentum determination is based on three stations of precision drift chambers that measure the trajectory of each muon in a toroidal magnetic field produced by three air-core toroids. In order to reach the MS, muons have to cross the electromagnetic and hadronic calorimeters, losing typically 3 to 5 GeV of energy, depending on the muon pseudorapidity. The calorimeters efficiently absorb the copious charged and neutral hadrons produced in lead-lead collisions.

The trigger system has three stages, the first of which (Level-1) is hardware based. The Level-1 minimum-bias trigger uses either the two sets of Minimum-Bias Trigger Scintillator (MBTS) counters, covering $2.1 < |\eta| < 3.9$ on each side of the experiment, or the two Zero-Degree Calorimeters (ZDC), each positioned at 140 m from the collision point, detecting neutrons and photons with $|\eta| > 8.3$. No muon-specific triggers were used to select the data presented here. The MBTS trigger was configured to require at least one hit above threshold from each side of the detector. A Level-2 timing requirement on a coincidence of signals from the MBTS was then imposed to remove beam backgrounds. The trigger efficiency was studied using an independent trigger probing random filled bunch crossings at Level-1. For these triggers, empty events were removed by testing for a minimal level of activity in the silicon detectors. The combined trigger and event selection efficiency is discussed in section 3.2.

In the offline analysis, minimum-bias triggered events are required to have a reconstructed primary vertex, at least one hit in each set of MBTS counters, and a time difference between the sides of less than 3 ns to reject beam-halo and other beam-related background events. Measurements of the

[1] In the right-handed ATLAS coordinate system, the pseudorapidity η is defined as $\eta = -\ln[\tan(\theta/2)]$, where the polar angle θ is measured with respect to the LHC beamline. The azimuthal angle ϕ is measured with respect to the x-axis, which points towards the centre of the LHC ring. The z-axis is parallel to the anti-clockwise beam viewed from above. Transverse momentum and energy are defined as $p_{\mathrm{T}} = p\sin\theta$ and $E_{\mathrm{T}} = E\sin\theta$, respectively.

3

6

muon trajectories from both the ID and MS are combined, resulting in a relative momentum resolution ranging from about 2% at low momentum up to about 3% at $p_T \sim 50$ GeV. For this analysis, oppositely charged muons are selected with a minimum p_T of 3 GeV each and within the region $|\eta| < 2.5$.

The data sample consists of approximately 6.7 μb^{-1} from the 2010 LHC heavy ion run. In order to determine the $J/\psi \to \mu^+\mu^-$ reconstruction efficiency, Monte Carlo (MC) samples have been produced superimposing J/ψ and Z events from PYTHIA [10] into simulated lead-lead events generated with the HIJING [11] event generator. HIJING was run in a mode with effects from jet quenching turned off, since they have not been adjusted to agree with existing experimental data. Elliptic flow was imposed on the events subsequent to generation, with a magnitude and p_T dependence derived from RHIC data. The detector response to the complete PYTHIA+HIJING event is simulated [12] using GEANT4 [13].

Lead-lead collision centrality percentiles are defined from the total transverse energy, ΣE_T^{FCal}, measured in the forward calorimeter (FCal), which covers $3.2 < |\eta| < 4.9$. The same conventions and bins for centrality are used as in our previous publication [14]. The centrality dependence of the muon detection efficiency is parameterized as a function of the total number of hits per unit of pseudorapidity detected in the first pixel layer. This is strongly correlated to ΣE_T^{FCal}, but gives a more direct measure of the ID occupancy. The full data sample is divided into four bins of collision centrality, 40-80%, 20-40%, 10-20%, and 0-10%. The most peripheral 20% of collisions are excluded from this analysis due to larger systematic uncertainties in estimating the number of binary nucleon-nucleon collisions in these events.

The $J/\psi \to \mu^+\mu^-$ reconstruction efficiency is obtained from the MC samples as a function of the event centrality. The inefficiency gradually increases from peripheral to central collisions, due primarily to an occupancy-induced inefficiency in the ID tracking, as shown in Table 1. The $Z \to \mu^+\mu^-$ reconstruction efficiency is obtained in a similar way.

An example of the very good agreement between data and MC in different centrality bins is presented in Figure 1, which shows the numbers of Pixel and SCT hits associated to tracks selected with a looser $p_T > 0.5$ GeV cut than that for the J/ψ. The figure shows results for data and MC at two different centralities (0–10% and 40–80%). The distributions of the number of hits averaged over η and the average number of hits as a function of η are shown. The slight decrease of the number of SCT hits on track as a function of centrality is well reproduced by the simulation, demonstrating that the

4

6

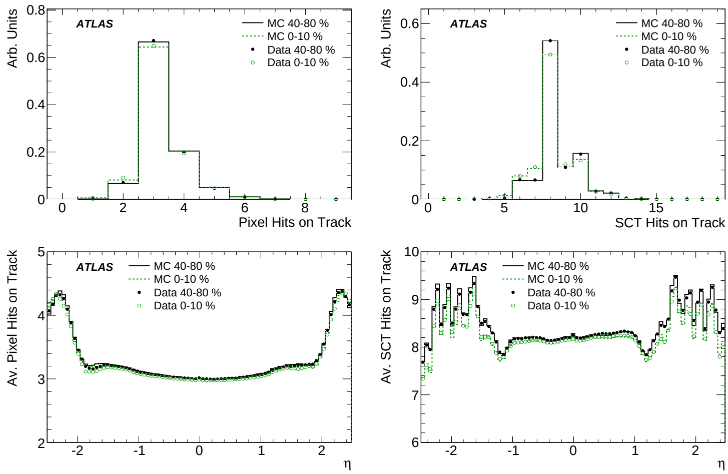

Figure 1: (top row) The number of Pixel (left) and SCT (right) hits on tracks for data (points with errors) and MC (histogram) for two different centrality bins: 0-10% (open/dotted) and 40-80% (closed/solid). (bottom row) The average number of Pixel (left) and SCT (right) hits as a function of η for MC and data in the same two centrality bins.

dense environment of the most central collisions is reasonably well modelled.

3. J/ψ production as a function of centrality

The oppositely-charged di–muon invariant mass spectra in the J/ψ region after the selection are shown in Figure 2. The number of $J/\psi \to \mu^+\mu^-$ decays is then found by a simple counting technique. The signal mass window is defined by the range 2.95–3.25 GeV. The background is derived from two mass sidebands, 2.4–2.8 GeV and 3.4–3.8 GeV, with a linear extrapolation. To determine the uncertainties related to the signal extraction, an alternative method based on a maximum likelihood fit with the mass resolution left as a free parameter is used as a cross check, as explained in section 3.1.

6

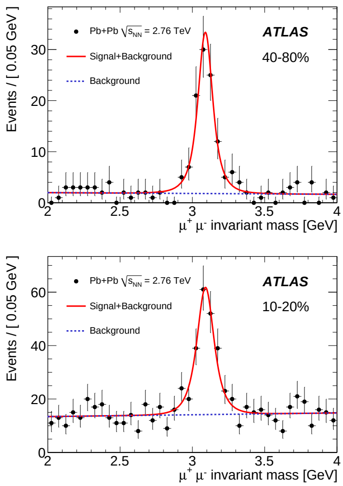

Figure 2: Oppositely-charged di–muon invariant mass spectra in the four considered centrality bins from most peripheral (40-80%) to most central (0-10%). The J/ψ yields in each centrality bin are obtained using a sideband technique. The fits shown here are used as a cross check.

Centrality-dependent efficiency corrections, derived from Monte Carlo events, are applied to the resulting signal yields. The number of J/ψ decays after background subtraction, but before any other correction, are listed in Table 1. With the chosen transverse momentum cuts on the decay muons, 80% of the reconstructed J/ψ have $p_T > 6.5$ GeV.

The measured J/ψ yields at different centralities are corrected by the reconstruction efficiency ϵ_c for $J/\psi \to \mu^+\mu^-$, derived from MC and parameterized in each centrality bin, and the width of the centrality bin, W_c, which represents a well-defined fraction of the minimum bias events. The corrected yield of J/ψ mesons is given by:

$$N_c^{\mathrm{corr}}(J/\psi \to \mu^+\mu^-) = \frac{N^{\mathrm{meas}}(J/\psi \to \mu^+\mu^-)_c}{\epsilon(J/\psi)_c \cdot W_c}. \quad (1)$$

The "relative yield" is defined by normalizing to the yield found in the most

6

Centrality	$N^{\rm meas}(J/\psi)$	$\epsilon(J/\psi)_c/$ $\epsilon(J/\psi)_{40-80}$	Systematic Uncertainty		
			Reco. eff.	Sig. extr.	Total
0-10%	190 ± 20	0.93 ± 0.01	6.8 %	5.2 %	8.6 %
10-20%	152 ± 16	0.91 ± 0.02	5.3 %	6.5 %	8.4 %
20-40%	180 ± 16	0.97 ± 0.01	3.3 %	6.8 %	7.5 %
40-80%	91 ± 10	1	2.3 %	5.6 %	6.1 %

Table 1: The measured numbers of J/ψ signal events per centrality bin before any correction, with their statistical errors, are listed in the second column. The relative efficiency corrections derived from the simulation are also shown, with the MC statistical error. The last columns give the experimental systematic uncertainties on the reconstruction efficiency and signal extraction, as well as the total uncertainty.

peripheral 40-80% centrality bin: $R_c = N_c^{\rm corr}/N_{40-80\%}^{\rm corr}$. Note that the uncertainties in the 40-80% bin are not propagated into this ratio for the more central bins. Finally, the "normalized yield" is defined by scaling the relative yield by the ratio $R_{\rm coll}$ of the mean number of binary collisions $N_{{\rm coll},c}$, detailed in section 3.2, in each centrality bin to that for the most peripheral (40-80%) bin: $R_{cp} = R_c/R_{\rm coll}$.

6

3.1. Experimental systematic uncertainties

Several experimental systematic effects are considered. These are grouped into those affecting the J/ψ reconstruction efficiency, and those from the extraction of the number of signal events from the di–muon mass spectra. Since this measurement only determines the relative yields as a function of centrality, only the centrality dependence of these effects is relevant. Any uncertainty on the absolute value cancels out in the ratio. The variation of the J/ψ reconstruction efficiency with centrality observed in simulation is mainly due to the larger occupancy in the ID. Because of the low occupancy in the MS by the primarily-soft tracks produced in heavy ion collisions, the fraction of muons from J/ψ decays with a reconstructed track in the MS is independent of centrality within the MC statistical uncertainty. On the other hand, to improve the reliability of the ID track reconstruction in the dense environment, rather stringent track quality requirements are made, relative to those defined for proton-proton collisions [15]. In particular, there must be at least nine silicon hits on each track, with no missing pixel hits and not more than one missing SCT hit, in both cases where such hits are expected. In order to evaluate systematic uncertainties, comparisons have been made between the distributions of hits associated with tracks and missing hits between data and MC as a function of centrality. The differences between the fraction of tracks with associated or missing hits close to the track selection cuts have been used to derive the systematic uncertainties on the ID track reconstruction that range between 1 and 3% as a function of the centrality. These uncertainties are fully correlated for both muons from the J/ψ decay, resulting in a systematic uncertainty up to about 7% on the J/ψ reconstruction efficiency. As an additional cross-check, the ID reconstruction was run with looser cuts on the number of missing pixel and SCT hits, in order to study directly the number of tracks lost because of the cuts on these quantities. The resulting track losses, as a function of centrality in data and simulation, were compatible with the systematic uncertainties derived with the hit comparison method described above. Further cross-checks have been made by studying the matching between the MS and ID momentum measurements, and by examining variables such as the track multiplicity distribution in a cone of $\Delta R < 0.1$ (where $\Delta R^2 = \Delta\phi^2 + \Delta\eta^2$) around muon candidates, and by evaluating the relative momentum difference between the two independent measurements of the same muon candidate. The fraction of muons measured in the MS but not matched to any ID track has also been compared in data and MC as a function of centrality. All of these studies show that the MC reproduces well the behaviour of the data as a function of centrality. The relative statistical uncertainty on the MC efficiency corrections ranges between 1.6 and 3.2% and this is combined in quadrature with the other uncertainties.

To address the uncertainties associated with the J/ψ signal extraction, an independent method based on an unbinned maximum likelihood fit is used to evaluate the number of signal events from the di–muon mass spectra. An overall scale factor on the event-by-event mass resolution is a free parameter of the fit, allowing for possible variations of resolution with centrality. Two different background parameterizations are used, with either a first or second order polynomial. The maximum deviation of the fitted yield compared to the sideband subtraction method is taken as the systematic uncertainty on the signal extraction.

The systematic uncertainties from the different sources are listed in Table 1.

3.2. Definition of N_{coll}

The mean number of binary nucleon-nucleon collisions, N_{coll}, corresponding to each centrality bin was calculated using a Glauber Monte Carlo package that has been applied extensively at RHIC energies [16, 17]. The impact parameter is selected randomly event by event, and both the number of participating nucleons which undergo at least one inelastic collision (N_{part}) and the number of binary collisions (i.e. the total number of nucleon-nucleon collisions, N_{coll}) are calculated for each event. The primary experimental inputs to the Glauber calculation are the radius (R) and skin depth (a) parameters of the Wood-Saxon parameterization of the nuclear density ($\rho(r) = \rho_0/[1+\exp((r-R)/a)]$), $R = 6.62 \pm 0.06$ fm and $a = 0.546 \pm 0.010$ fm, respectively [18], and the nucleon-nucleon inelastic cross-section, assumed to be $\sigma_{\text{inel}} = 64 \pm 6$ mb from an extrapolation of lower energy data. Using these parameters, the Glauber calculations give a total inelastic cross section of 7.6 barns, which is defined as the "geometric" cross section below.

Systematic uncertainties on the resulting R_{coll} values are estimated by separately varying R, a and σ_{inel} by one standard deviation. The variations of R and a are found to give results of the same magnitude but opposite sign, indicating that the uncertainties on the two parameters are correlated. However, they are conservatively treated as uncorrelated for the error analysis used in these studies.

Any possible variation in the fraction of the geometric cross section selected by the combination of trigger and event selection criteria, ε_{mb}, as a function of centrality must also be considered in evaluating systematic uncertainties on the lead-lead collision geometry, so that the centrality percentiles correspond to the correct fractions of the efficiency-corrected geometric cross section. The uncertainty is estimated by examining the distribution of $\Sigma E_{\text{T}}^{\text{FCal}}$ in the independent data sample selected by a random trigger and filtered by requiring a minimal amount of Inner Detector activity. The event selection criteria described above are also applied, with an additional requirement that both ZDCs see energies consistent with the presence of at least one neutron. This combination of vertex, MBTS and ZDC selections efficiently rejects photonuclear interactions [19]. The total selected fraction of the geometric cross section is estimated using a fit to the resulting $\Sigma E_{\text{T}}^{\text{FCal}}$ distribution, assuming the transverse energy in each event results from a superposition of participating nucleons and binary collisions (a similar assumption to that used in Ref. [20]):

$$\Sigma E_{\mathrm{T}}^{\mathrm{FCal}} = E_{\mathrm{T}}^{pp}\left\{(1-x)\frac{N_{\mathrm{part}}}{2} + xN_{\mathrm{coll}}\right\}. \quad (2)$$

In this formula, E_{T}^{pp} is the value of $\Sigma E_{\mathrm{T}}^{\mathrm{FCal}}$ when $N_{\mathrm{part}} = 2$ and $N_{\mathrm{coll}} = 1$ (the values for a single proton-proton collision) and x controls the relative contribution of participants and binary collisions in lead-lead events. An additional constant noise term is also included to account for the low energy part of the distribution. Distributions of $\Sigma E_{\mathrm{T}}^{\mathrm{FCal}}$ are generated for 500k MC events and fitted to the data for a range of values of x (from 0.09 to 0.15), and also varying E_{T}^{pp} and the noise term. For all cases, the integral of the observed distribution in data accounts for around 98% of the best fit to the simulated distribution, with a variation of around 1%. This provides an estimate of the total event selection efficiency $\varepsilon_{\mathrm{mb}}$ relative to the geometric cross section. An absolute systematic error of $\pm 2\%$ is assigned to $\varepsilon_{\mathrm{mb}}$ with the positive range also accounting for the possible leakage of photonuclear events into the event sample used to obtain the $\Sigma E_T^{\mathrm{FCal}}$ distribution.

Centrality	R_{coll}	Uncertainty
0-10%	19.5	5.3 %
10-20%	11.9	4.7 %
20-40%	5.7	3.2 %
40-80%	1.0	–

Table 2: The correction factors R_{coll}, together with the relative systematic uncertainty, stated as a 1σ value.

The total systematic uncertainties on the ratios R_{coll} are evaluated by combining the variations with R, a, σ_{inel} and $\varepsilon_{\mathrm{mb}}$, in quadrature. The values of R_{coll} and their systematic uncertainties are reported in Table 2. It should be noted that the estimate of $\varepsilon_{\mathrm{mb}}$ leads to correlations between the extracted values of N_{coll}, and thus the uncertainties on R_{coll} are also correlated bin-to-bin.

3.3. J/ψ yields

The relative J/ψ yields after normalization and efficiency corrections as in equation 1, R_c, are compared to the expected R_{coll} values in the left panel of Figure 3. The yield errors are computed by adding the statistical and

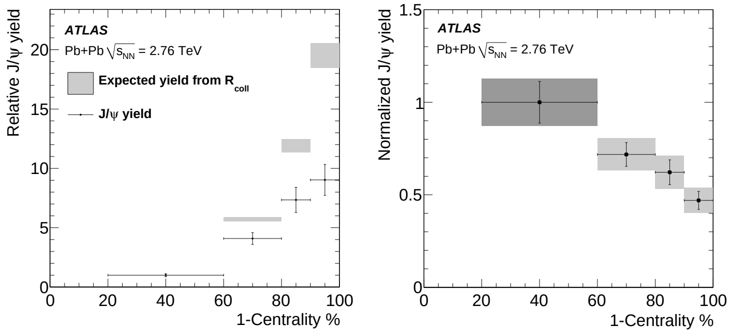

Figure 3: (left) Relative J/ψ yield as a function of centrality normalized to the most peripheral bin (black dots with errors). The expected relative yields from the (normalized) number of binary collisions (R_{coll}) are also shown (boxes, reflecting 1σ systematic uncertainties). (right) Value of R_{cp}, as described in the text, as a function of centrality. The statistical errors are shown as vertical bars while the grey boxes also include the combined systematic errors. The darker box indicates that the 40-80% bin is used to set the scale for all bins, but the uncertainties in this bin are not propagated into the more central ones.

systematic uncertainties in quadrature. A clear difference is observed as a function of centrality between the measured relative J/ψ yield and the prediction based on R_{coll}, indicating a deviation from the simplest expectation based on QCD factorization. The ratio of these two values, R_{cp}, is shown as a function of centrality in the right panel of Figure 3. The data points are not consistent with their average, giving a $P(\chi^2, N_{\text{DOF}})$ value of 0.11% with three degrees of freedom, computed conservatively ignoring any correlations among the systematic uncertainties. Instead, a significant decrease of R_{cp} as a function of centrality is observed.

4. *Z* production as a function of centrality

Z candidates are selected by requiring a pair of oppositely charged muons with $p_{\text{T}} > 20$ GeV and $|\eta| < 2.5$ [21]. An additional cosmic ray rejection cut on the sum of the pseudorapidities of the two muons, $|\eta_1 + \eta_2| > 0.01$, is also applied. The invariant mass distribution of the selected pairs is shown in the

Centrality	N(Z)	$\epsilon(Z)_c/\epsilon(Z)_{40-80}$
0-10%	19	0.99 ± 0.01
10-20%	5	0.97 ± 0.01
20-40%	10	0.98 ± 0.01
40-80%	4	1

Table 3: The number of Z events per centrality bin and the relative efficiency corrections derived from the simulation.

left panel of Figure 4. With this selection, 38 Z candidates are retained in the signal mass window of 66 to 116 GeV. The background after this selection is expected to be below 2%, and is not corrected for in the result. The number of Z events in each centrality bin is given in Table 3.

The R_{cp} variable for the Z candidates is computed in the same way as for the J/ψ sample. The relative efficiency corrections determined from dedicated MC samples are given in Table 3. For high transverse momentum tracks, the reconstruction is expected to perform as well as or better than in the low p_{T} regime characteristic of the J/ψ study. For this reason, the same systematic uncertainties as for the J/ψ results have been applied to the Z relative yield measurements. Several cross-checks have been performed to support this assumption. In addition to the tracks reconstructed with the combined ID and MS information, tracks reconstructed by the MS alone have been checked, and only one additional candidate was found. This candidate has been inspected and an ID track was in fact found but with too few hits to pass the stringent reconstruction requirements. The Z selection was also applied to same charge muon pairs, and no candidates were selected within the 66–116 GeV mass window. To control the residual background from cosmic rays, the distribution of the difference of the transverse impact parameters of the two muons from Z candidates was examined and found to be compatible with that expected for collision muons.

The measured Z yields are displayed in the right panel of Figure 4, normalized to the yield in the most peripheral bin and to the number of binary collisions (R_{cp}). Although, within the large statistical uncertainty, they appear to be compatible with a linear scaling with the number of binary collisions, the low statistics preclude drawing any conclusion.

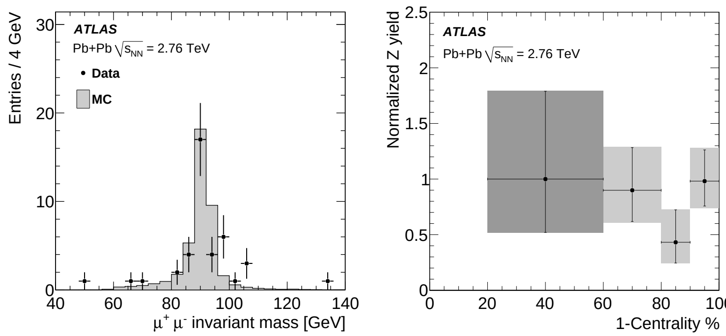

Figure 4: The di–muon invariant mass (left) after the selection described in the text. The value of R_{cp} (right) computed with the 38 selected Z candidates. The statistical errors are shown as vertical bars while the grey boxes also include the combined systematic errors. The darker box indicates that the 40-80% bin is used to set the scale for all bins, but the uncertainties in this bin are not propagated into the more central ones.

5. Conclusion

The first results on J/ψ and $Z \to \mu^+\mu^-$ relative yields measured in lead-lead collisions obtained with the ATLAS detector at the LHC, have been presented. In a sample of events with oppositely charged muon pairs with a transverse momentum above 3 GeV and with $|\eta| < 2.5$, a centrality dependent suppression is observed in the normalized J/ψ yield. The relative yields of the 38 observed Z candidates as a function of centrality are also presented, although no conclusion can be inferred about their scaling with the number of binary collisions.

Acknowledgements

We thank CERN for the efficient commissioning and operation of the LHC during this initial heavy ion data taking period as well as the support staff from our institutions without whom ATLAS could not be operated efficiently.

We acknowledge the support of ANPCyT, Argentina; YerPhI, Armenia; ARC, Australia; BMWF, Austria; ANAS, Azerbaijan; SSTC, Belarus; CNPq and FAPESP, Brazil; NSERC, NRC and CFI, Canada; CERN; CONICYT, Chile; CAS, MOST and NSFC, China; COLCIENCIAS, Colombia; MSMT CR, MPO CR and VSC CR, Czech Republic; DNRF, DNSRC and Lundbeck Foundation, Denmark; ARTEMIS, European Union; IN2P3-CNRS, CEA-DSM/IRFU, France; GNAS, Georgia; BMBF, DFG, HGF, MPG and AvH Foundation, Germany; GSRT, Greece; ISF, MINERVA, GIF, DIP and Benoziyo Center, Israel; INFN, Italy; MEXT and JSPS, Japan; CNRST, Morocco; FOM and NWO, Netherlands; RCN, Norway; MNiSW, Poland; GRICES and FCT, Portugal; MERYS (MECTS), Romania; MES of Russia and ROSATOM, Russian Federation; JINR; MSTD, Serbia; MSSR, Slovakia; ARRS and MVZT, Slovenia; DST/NRF, South Africa; MICINN, Spain; SRC and Wallenberg Foundation, Sweden; SER, SNSF and Cantons of Bern and Geneva, Switzerland; NSC, Taiwan; TAEK, Turkey; STFC, the Royal Society and Leverhulme Trust, United Kingdom; DOE and NSF, United States of America.

The crucial computing support from all WLCG partners is acknowledged gratefully, in particular from CERN and the ATLAS Tier-1 facilities at TRIUMF (Canada), NDGF (Denmark, Norway, Sweden), CC-IN2P3 (France), KIT/GridKA (Germany), INFN-CNAF (Italy), NL-T1 (Netherlands), PIC (Spain), ASGC (Taiwan), RAL (UK) and BNL (USA) and in the Tier-2 facilities worldwide.

References

[1] T. Matsui and H. Satz, Phys. Lett. **B178** (1986) 416.

[2] A. Mocsy and P. Petreczky, Phys. Rev. Lett. **99** (2007) 211602.

[3] NA50 Collaboration, B. Alessandro *et al.*, Eur. Phys. J. **C39** (2005) 335-345.

[4] PHENIX Collaboration, A. Adare *et al.*, Phys. Rev. Lett. **98** (2007) 232301.

[5] NA3 Collaboration, J. Badier *et al.*, Z. Phys. C **20** (1983) 101. NA38 Collaboration, M. C. Abreu *et al.*, Phys. Lett. **B444** (1998) 516. FNAL E866 Collaboration, M. J. Leitch *et al.*, Phys. Rev. Lett. **84** (2000) 3256. NA50 Collaboration, B. Alessandro *et al.*, Eur. Phys. J. C **33** (2004) 31. NA50 Collaboration, B. Alessandro *et al.*, Eur. Phys. J. C **48** (2006) 329. HERA-B Collaboration, I. Abt *et al.*, Eur. Phys. J. C **60** (2009) 525. PHENIX Collaboration, A. Adare *et al.*, arXiv:1010.1246 [nucl-ex], submitted to Phys. Rev. Lett.

[6] R. L. Thews and M. L. Mangano, Phys. Rev. **C73** (2006) 014904.

[7] R. Vogt, Phys. Rev. **C64** (2001) 044901.

[8] ATLAS Collaboration, G. Aad *et al.*, JINST **3** S08003 (2008).

[9] ATLAS Collaboration, G. Aad *et al.*, CERN-OPEN-2008-020.

[10] T. Sjostrand, S. Mrenna and P. Z. Skands, JHEP **0605** (2006) 026.

[11] X. -N. Wang and M. Gyulassy, Phys. Rev. **D44** (1991) 3501-3516.

[12] ATLAS Collaboration, G. Aad *et al.*, Eur. Phys. J. C **70** (2010) 823-874.

[13] GEANT4 Collaboration, S. Agostinelli *et al.*, Nucl. Instrum. Meth. A **506** (2003) 250.

[14] ATLAS Collaboration, G. Aad *et al.*, Phys. Rev. Lett. **105** (2010) 252303.

[15] ATLAS Collaboration, G. Aad *et al.*, Phys. Lett. **B688**, (2010) 21-42.

[16] B. Alver, M. Baker, C. Loizides *et al.*, arXiv:0805.4411 [nucl-ex].

[17] M. L. Miller, K. Reygers, S. J. Sanders *et al.*, Ann. Rev. Nucl. Part. Sci. **57** (2007) 205-243.

[18] H. De Vries, C. W. De Jager and C. De Vries, Atom. Data Nucl. Data Tabl. **36** (1987) 495-536.

[19] O. Djuvsland and J. Nystrand, arXiv:1011.4908 [hep-ph].

[20] ALICE Collaboration, K. Aamodt *et al.*, arXiv:1012.1657 [nucl-ex].

[21] ATLAS Collaboration, G. Aad *et al.*, arXiv:1010.2130v1 [hep-ex], accepted by JHEP.

Chapter 7

Search for $H \to ZZ^{(*)} \to \mu^-\mu^+\mu^-\mu^+$ in 1 fb^{-1} of 7 TeV pp collisions

7.1 Introduction

In Chapters 4 and 5 we have discussed the performance of the Muon Spectrometer in cosmic-data taking as well as in collision data taking. Di-muon final states were used to evaluate the efficiency and muon momentum resolution of the muon reconstruction algorithms. In this chapter we use muons for a physics analysis: the search for Standard Model Higgs bosons decaying into a four muon final state via two intermediate Z bosons. In Section 7.2 the data-set used for the analysis is described. Section 7.3 covers the applied event selections and shows the observed candidates in simulation and in data after these selections. The significance of the observed signal candidates in data is evaluated in Section 7.4.

7.2 Data-set

Before mentioning the actual data-set used for this analysis we need to define the signal we are searching for. Afterwards, the relevant backgrounds to this particular signal are introduced. The event selections in Section 7.3 aim at reducing these backgrounds while keeping as much signal as possible.

Signal

In this analysis the signal is defined as a Standard Model Higgs boson decaying into four muons via two intermediate Z bosons. Section 2.5 discussed the Higgs production and its decay at the LHC. The dominant production mechanism at the LHC is via gluon-gluon fusion. The branching ratio $H \to ZZ$ depends on the mass of the Higgs boson (cf. Figure 2.10(b)). Given its mass, a precise prediction can be made of the number of Higgs bosons that we expect to observe in ATLAS. However, the mass of the Higgs boson is an unknown parameter in the Standard Model. Therefore a search is presented for Higgs masses in the range of 115 to 500 GeV.

Backgrounds

The Standard Model has several processes other than $H \to ZZ^{(*)} \to \mu^-\mu^+\mu^-\mu^+$ which can result in a final state with four muons. We will refer to these processes as Standard Model background. The major component of the background consists of a continuum from irreducible ZZ events. Other important backgrounds are from $Zb\bar{b}$ and $t\bar{t}$ events. In $Zb\bar{b}$ events the semi-leptonic decay of the b quarks can result in two (extra) muons. In $t\bar{t}$ events the decay of the top quark almost always produces a W boson and a b quark. If both W bosons decay to a muon and a neutrino and the b quarks decay semi-leptonically this also results in a four muon final state.

Data-set

We have searched for the presence of a Standard Model Higgs signal in the 2011 LHC data-set recorded up till June 26$^{\text{th}}$. Events are triggered at the Event Filter stage by a muon of $p_T > 18$ GeV. The recorded integrated luminosity for this choice of trigger is 1.05 ± 0.04 fb^{-1}. The uncertainty on the luminosity is 3.7% [65].

A full overview of the simulated data-sets used in this analysis can be found in Appendix B. These include Higgs samples from gluon-gluon fusion in a mass range of 110 to 600 GeV as well as samples for the relevant backgrounds. The ZZ sample from `PYTHIA` has been reweighted according to `MCFM 6.0` [66, 67]. All samples are produced centrally and are greatly reduced in size, i.e. *skimmed*, by selecting events with four leptons [68]. The leptons can be either electrons or muons with some minor quality selections applied. Combined or segment-tagged muons are selected with a $p_T > 7$ GeV. Standalone muons are only added in the forward region, i.e. $|\eta| > 2.5$.

7.3 Event selection

The event selections aim at reducing the Standard Model background while keeping as many signal candidates as possible. We apply the selections on simulation and look at the resulting distributions of the four muon invariant mass, $M_{4\mu}$. Table 7.1 gives the numbers after several selection steps, which we discuss below, for simulation and data.

Our signal is a Standard Model Higgs boson decaying to a four muon final state via two intermediate Z bosons. Some obvious preselections can be applied. A primary vertex with at least three associated tracks is required. At least four `MUID` muons should be present, each with a transverse distance[1] to the primary vertex $|d_0| < 1$ mm. Muons from heavy quark decays are expected to originate from displaced secondary vertices, where the leptons from Z boson decays originate from the primary vertex. One of the muons in the event must have triggered the event. The trigger used is `EF_mu18_MuGirl`, which is the lowest p_T unprescaled single muon trigger. The same Inner Detector track quality cuts as discussed in Section 5.2.1 are applied.

[1]The transverse distance is defined as the distance in the transverse plane, i.e. $|d_0| \equiv \sqrt{x_0^2 + y_0^2}$.

By selecting opposite sign muon pairs and calculating the di-muon invariant mass one obtains multiple Z candidates. From these we select a *primary* Z candidate and a *secondary* Z candidate. The primary Z candidate has a di-muon invariant mass closest to the world average value of the Z mass, i.e. 91.1876 GeV, with a maximum allowed deviation of 15 GeV from this value. The secondary Z candidate (or *off-shell* Z^*) is the candidate that has the second closest mass while using two other muons. The selections discussed up to this point are referred to as *preselections* in Table 7.1. Figure 7.1 shows the masses of the primary and secondary Z candidates in simulation after preselections. In the ZZ sample the generated mass of the secondary Z is always greater than 12 GeV.

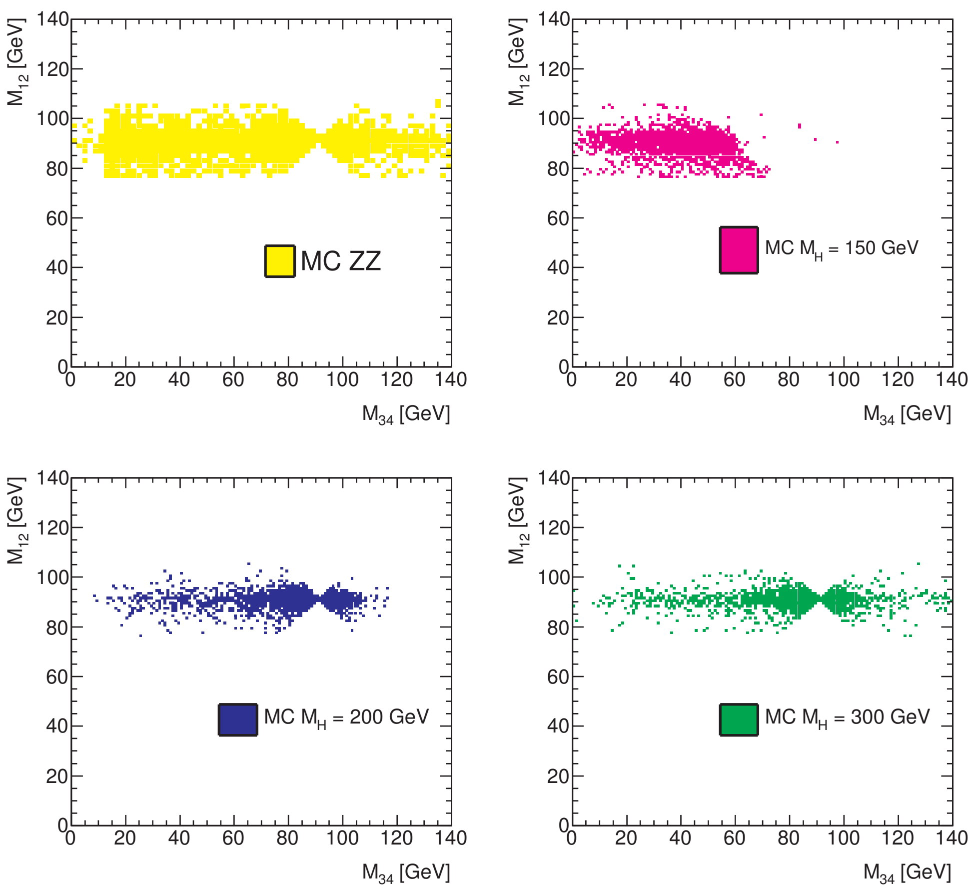

Figure 7.1: The mass of the primary Z candidate (M_{12}) versus the mass of the secondary Z candidate (M_{34}) after the preselections. Simulations of the ZZ background, a 150 GeV Higgs, a 200 GeV Higgs and a 300 GeV Higgs are shown.

Our signal contains at least one on-shell Z boson, i.e. the primary Z candidate. Therefore we ask for at least two high-p_T muons ($p_T > 20$ GeV) in an event. The four muons from the two Z candidates are required to be separated in η and ϕ by demanding $\Delta R > 0.10$ for all muon combinations. Table 7.1 shows that this selection substantially reduces the background from heavy quark decays.

The background from heavy quark decays is further reduced by requiring that the muons are isolated from other tracks in the Inner Detector and from energy deposits in the calorimeter. For sufficient track isolation the muons should have `ptcone20`$< 0.15 \cdot p_T$, where `ptcone20` is the summed p_T of tracks within a cone of $\Delta R < 0.20$ around the muon. The muon itself is excluded from the sum. Calorimetric isolation uses a similar variable `etcone20`: the summed energy deposits in a cone of $\Delta R < 0.20$ around the muon. Again the muon itself is excluded from the sum. The selection on the calorimetric isolation is `etcone20`$< 0.20 \cdot p_T$. To correct for pile-up the value of `etcone20` is lowered by 33.5 MeV for each additional primary vertex observed in the event [69]. Table 7.1 shows that these isolation criteria have a large impact on the backgrounds from heavy quark decays.

Sample	H150	H200	H300	ZZ	$t\bar{t}$	$Zb\bar{b}$	Z	data
Total entries	5721	5539	5545	149969	$5 \cdot 10^5$	$66 \cdot 10^6$	$5 \cdot 10^5$	-
Events after:								
preselections	2957	3734	3882	11025	307	$4 \cdot 10^6$	9	169
	(100%)	(100%)	(100%)	(100%)	(100%)	(100%)	(100%)	(100%)
≥ 2 high-p_T μ's	2898	3721	3873	10953	271	$3.6 \cdot 10^6$	8	130
ΔR	2874	3693	3869	10910	153	$2.8 \cdot 10^6$	3	31
track isolation	2684	3442	3703	10458	1	234923	0	12
calo isolation	2650	3381	3622	10247	1	181683	0	12
$\lvert d_0\rvert/\sigma(d_0)$<3.5	2619	3342	3599	10161	1	66532	0	12
all tight muons	2539	3245	3472	9892	1	64017	0	10
	(85.9%)	(86.9%)	(89.4%)	(89.7%)	(3.3%)	(1.6%)	(0%)	(5.9%)
Higgs reco. eff	44.4%	58.6%	61.8%	-	-	-	-	-
Events in 1 fb^{-1}	0.52	1.04	0.62	5.46	0.02	0.04	0.0	10

Table 7.1: Number of events passing the subsequent selections.

If all selection criteria are fulfilled the four muon invariant mass, $M_{4\mu}$, is computed. The primary Z candidate is constrained to the world average Z mass in this computation. This effectively results in a scaling of the measured muon momentum parameters. If $M_{4\mu}$ is smaller than 190 GeV an additional selection is applied on the impact parameter significance of the two softest muons in the event: $|d_0|/\sigma(d_0) < 3.5$. This substantially reduces the $Zb\bar{b}$ background with only a small effect on the signal (cf. Table 7.1).

The event selections reduce $Zb\bar{b}$ and $t\bar{t}$ down to a rate well below the ZZ background. The ZZ background is irreducible and results in a non-negligible background over the full mass range in this study. Further reduction can possibly be accomplished by exploiting possible differences between ZZ and Higgs samples, e.g. using the mass of the secondary Z candidate or the p_T of the 4μ combination. We have not looked into this possibility but acknowledge the fact that this can improve the strength of this analysis in the future. Figure 7.2 shows the total Standard Model background after all event selections with results for Higgs masses of 150, 200 and 300 GeV added to this.

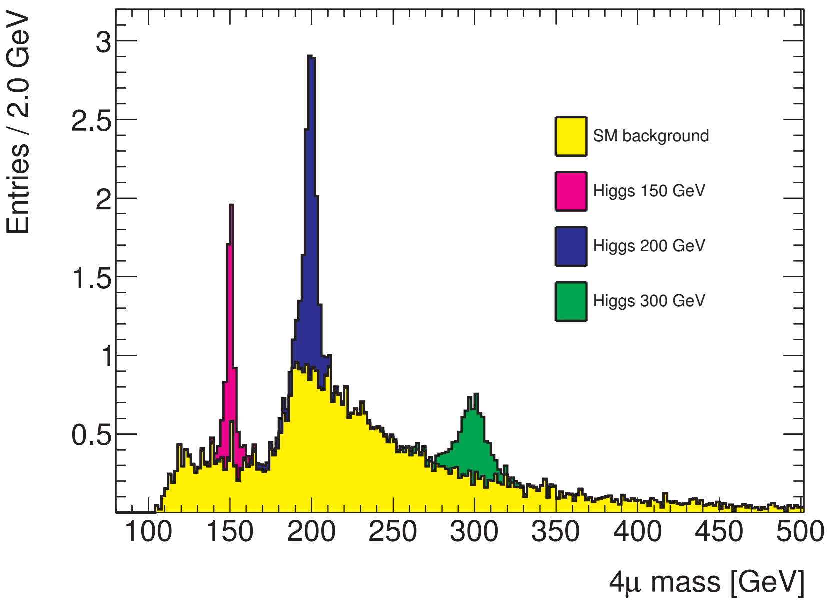

Figure 7.2: Four muon invariant mass after event selections for simulation of Standard Model background plus several Higgs samples. All samples are normalized to 1 fb^{-1}.

Higgs reconstruction efficiency

For the various Higgs masses the efficiency of the event selection is evaluated. Figure 7.3 shows the Higgs reconstruction efficiency as a function of the simulated Higgs mass. The Higgs reconstruction efficiency is defined as the efficiency for a Higgs decay with a four muon final state to pass all analysis selections, i.e. including preselections.

At low Higgs masses (≤ 200 GeV) a lower efficiency is observed: muons in this region will be relatively soft because of the low mass of the secondary Z. Soft muons will less often pass our kinematic cuts and isolation requirements. The isolation requirements are nevertheless needed, especially in this region, to reduce backgrounds from $Zb\bar{b}$ and $t\bar{t}$. At high Higgs masses the efficiency reaches a plateau around 70% mainly as a result of the acceptance of the Muon Spectrometer. For $|\eta| < 2.5$ this is about 90%.

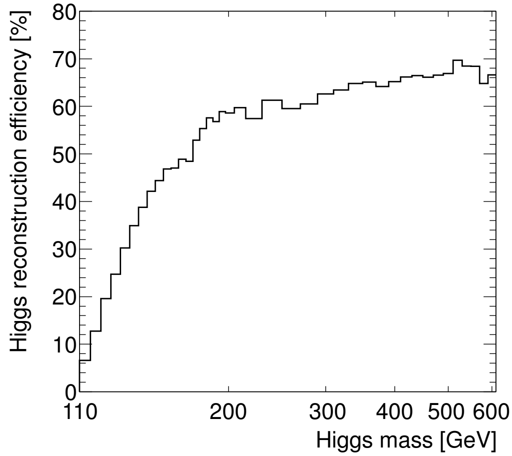

Figure 7.3: Higgs reconstruction efficiency as a function of the simulated Higgs mass.

Data

There are ten events observed in data that pass all event selections. Figure 7.4 shows an event display of one of the observed candidates. Table 7.2 gives the run number, event number and invariant mass of the observed 4μ candidates. It also gives the masses of the primary and secondary Z candidates as M_{12} and M_{34}, respectively[2].

Run	Event	4μ mass [GeV]	M_{12} [GeV]	$M_{34} [GeV]$
180124	3972690	138.6	92.3	9.4
182486	33852512	196.9	99.3	73.1
182766	5404925	240.7	89.8	83.8
183003	121099952	620.7	83.5	99.7
183003	44433120	210.0	92.9	94.3
183081	101085720	144.2	91.6	47.4
183272	44764944	101.8	80.3	4.2
183391	19834576	208.8	90.7	94.7
183426	47756740	449.1	91.4	89.5
183580	5574469	200.8	92.1	88.9

Table 7.2: Events in data passing all event selections.

[2]No cut on the lower value of M_{34} is applied in this analysis. In the simulation of the ZZ background such a cut was applied at 12 GeV. However, the effect of this cut on data is expected to be small as most of the four muon events with $M_{34} < 12$ GeV will not pass the muon p_T requirements. Only a small fraction of events will survive all event selections, creating no artifical peaks in the 4μ mass distribution.

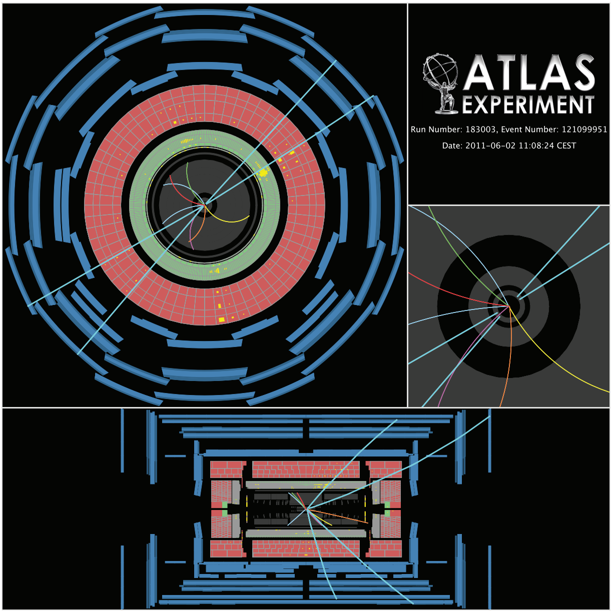

Figure 7.4: `Atlantis` [70] event display of one $H \to ZZ \to 4\mu$ candidate in data.

Figure 7.5 shows the 4μ invariant mass distribution for events passing all selections in data and simulation. We expect a total of 5.52 events from Standard Model background processes. How to interpret the observed *excess* of candidates is discussed next.

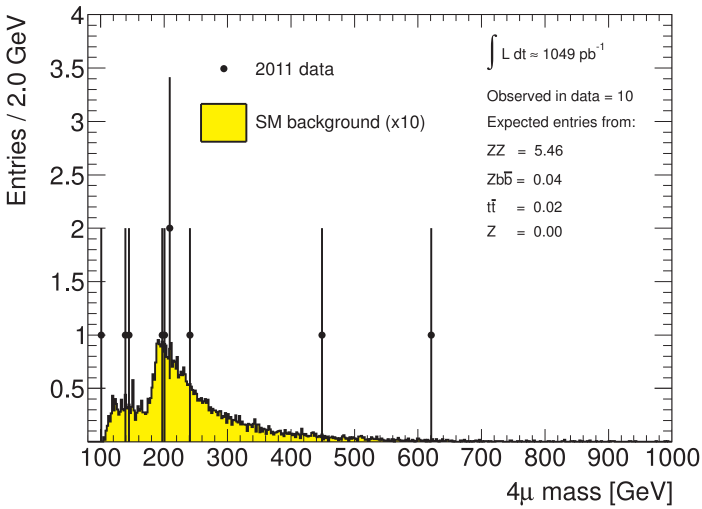

Figure 7.5: Four muon invariant mass for selected events in data and simulation.

7.4 Discovery/exclusion of a Higgs signal

Our event selections result in 10 observed candidates in data, where 5.52 events are expected from Standard Model (SM) background processes. Is this excess of candidates sufficient to claim a *discovery* of the SM Higgs boson? And if not, can we *exclude* a SM Higgs boson? We will answer these questions for a Higgs mass range of 115 to 500 GeV. First, some concepts need to be introduced.

Test statistic and likelihood functions

The observed excess can either be the result of a SM Higgs boson or of an upward fluctuation of SM background events. These two hypotheses form the basis for the study to quantify our results. The first step is to define a *test statistic*, i.e. a variable that distinguishes between the two hypotheses. Our test statistic uses *likelihood functions*, $\mathcal{L}$, to answer the following question:

> *How much more likely is it that the observed data is the result of a Higgs boson decay on top of Standard Model background processes than from Standard Model background processes alone?*

To answer this question two templates are built of the four muon invariant mass distributions: one for the summed background and one for the Higgs signal (cf. Figure 7.2). All templates are normalized to an integrated luminosity of 1 fb^{-1}. The templates are used to construct the likelihood functions $\mathcal{L}_b$ and $\mathcal{L}_{s+b}$ for the background-only and signal-plus-background hypothesis, respectively. We take the construction of $\mathcal{L}_b$ as an example:

7

For each mass bin i of the background template we compute the Poisson probability $P(N^i_{obs}|f^i_b)$, where N^i_{obs} is the number of observed events in data and f^i_b is the background template value for bin i. All bins i in a mass range of 115 to 500 GeV are taken into account. The likelihood function is defined as $\mathcal{L}_b = \prod_i P(N^i_{obs}|f^i_b)$ and similarly $\mathcal{L}_{s+b} = \prod_i P(N^i_{obs}|(f^i_s + f^i_b))$.

The background normalization is the dominant systematic in our study [71]. To account for this uncertainty we fit the normalization to the data when building our likelihood functions[3]. This effectively changes our likelihood functions to *profile likelihood functions*: $\mathcal{L}_b \to \mathcal{L}_b(\mu_s = 0, \hat{\hat{\theta}}_{b_b})$, where μ_s is the (fixed) scaling of the signal template and $\hat{\hat{\theta}}_{b_b}$ is the scaling of the background template that maximizes the likelihood function.

The ratio of the computed likelihoods is used to construct our eventual *test statistic*:

$$\mathrm{X} = -2\ln(Q) = -2\ln\left(\frac{\mathcal{L}_{s+b}(\mu_s = 1, \hat{\hat{\theta}}_{b_{s+b}})}{\mathcal{L}_b(\mu_s = 0, \hat{\hat{\theta}}_{b_b})}\right). \tag{7.1}$$

[3]We do so by choosing the background scaling that maximizes the likelihood function. This method, and its effect on our analysis, is discussed in more detail in Appendix C.

By taking the logarithm of the likelihoods we obtain a sum instead of products in the definition of $\mathcal{L}$. The factor -2 is a convention to make the search for the most likely value a search for a minimum value instead of a maximum value. As a result of this definition we observe the following qualitative feature: a higher value for the test statistic indicates a more background-like signal.

Toy Monte Carlo

To quantify the significance of the observed value of the test statistic we need to compare this value with distributions from many simulated experiments, obtained with so-called toy Monte Carlo (MC) techniques. A toy mass distribution is built up from our templates as follows: each mass bin is filled by a random number generator from a Poisson distribution, taking the expected number of events from the background (+signal) template in that mass bin as the Poisson mean value for the background-only (signal-plus-background) hypothesis. A test statistic is computed for the toy mass distribution. Each toy MC experiment gives a value for the test statistic. From 100,000 toy MC experiments we obtain two test statistic distributions: one for the background only hypothesis and one for the hypothesis with a Higgs signal added to the background.

Confidence levels

Figure 7.6 shows example test statistic distributions for two hypotheses. The signal-plus-background hypothesis is indicated with the dotted line. The background-only hypothesis is shown as a solid line. Two *confidence levels* (CL) are indicated for a given observed test statistic value, $\mathrm{X_{obs}}$:

- $1 - \mathrm{CL_b}$ indicates the fraction of experiments in the background-only test statistic distribution that have an equal or lower test statistic value than $\mathrm{X_{obs}}$, i.e. that are equally signal like or more signal like than $\mathrm{X_{obs}}$;
- $\mathrm{CL_{s+b}}$ indicates the fraction of experiments in the signal-plus-background test statistic distribution that have an equal or higher test statistic value than $\mathrm{X_{obs}}$, i.e. that are equally background like or more background like than $\mathrm{X_{obs}}$.

By combining these two confidence levels we obtain $\mathrm{CL_s}$, what some people refer to as *"an approximate confidence in the signal-only hypothesis"* [72]. $\mathrm{CL_s}$ is defined as $\mathrm{CL_{s+b}}/\mathrm{CL_b}$ [4] and was introduced during Higgs searches at LEP. By normalizing $\mathrm{CL_{s+b}}$ to $\mathrm{CL_b}$ one prevents wrongly claiming an exclusion when the analysis is in fact not sensitive to differences between the two hypotheses[5]. But when can a discovery or exclusion actually be claimed?

[4] $\mathrm{CL_s}$ is set to 0 if $\mathrm{CL_b} = 0$.

[5] One example of this is when the two test statistic distributions are very similar.

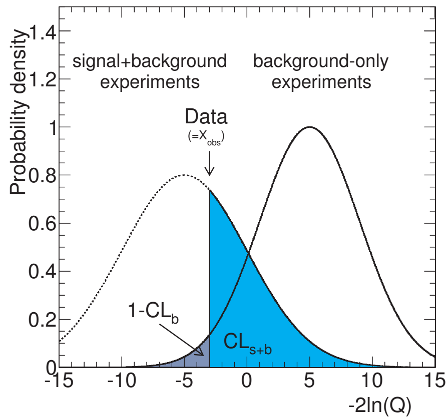

Figure 7.6: Example test statistic distributions for the background-only (right) and signal-plus-background (left) hypotheses. For a given observed test statistic, $\mathrm{X_{obs}}$, confidence levels $1 - \mathrm{CL_b}$ and $\mathrm{CL_{s+b}}$ are colored and labeled accordingly.

Claiming a discovery or excluding a signal

By convention, a discovery can be claimed if it is improbable that the observed test statistic value is the result of the background-only hypothesis. In this case a value of $1 - \mathrm{CL_b} \leq 5.7 \cdot 10^{-7}$, i.e. a 5σ deviation for a Gaussian distribution, is considered as improbable. If no discovery can be claimed the next step is to study whether a signal can be excluded. A signal is excluded if it is improbable that the observed test statistic value is the result of the signal-plus-background hypothesis. For an exclusion a value of $\mathrm{CL_s} \leq 0.05$, i.e. a 2σ deviation for a Gaussian distribution, is considered as improbable.

7.4.1 Results

We apply the procedure described above to our data, assuming a Higgs with a mass of 200 GeV. Figure 7.7 shows the toy MC distributions. The shapes of the two distributions are not Gaussian-like because we are dealing with a low number of expected events. The background-only hypothesis is displayed with a solid line. The bands corresponding to $\pm 1\sigma$ and $\pm 2\sigma$ for this hypothesis are colored green and yellow, respectively[6]. The figure indicates the test statistic value obtained in data, i.e. -1.81. The corresponding values for $1 - \mathrm{CL_b}$ and $\mathrm{CL_s}$ are 0.26 and 0.78, respectively. From these obtained confidence levels it can be concluded that neither a discovery nor an exclusion can be claimed.

To see if we actually *expect* to be able to claim a discovery or an exclusion we look at the median values of the two test statistic distributions. For the median of the signal-plus-background hypothesis $1 - \mathrm{CL_b}$ is computed to be 0.187. This indicates that no discovery is expected. The median of the background-only hypothesis $\mathrm{CL_s}$ is computed to be 0.418. This indicates that no exclusion is expected either.

[6]The bands are defined such that 84.1% (97.9%) is within $\pm 1\sigma$ ($\pm 2\sigma$) of the median value.

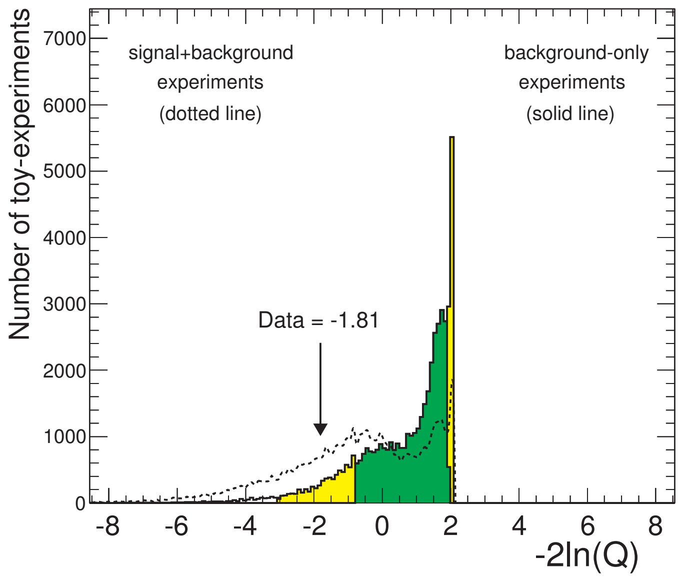

Figure 7.7: Test statistics for data and toy MC for a 200 GeV Higgs signal.

Table 7.3 summarizes the results for a Higgs with a 200 GeV mass. The same studies have been performed over the mass range of 115 to 500 GeV with similar results.

	data	s+b	b-only
$1 - \mathrm{CL_b}$	0.26	0.187	0.500
$\mathrm{CL_s}$	0.78	0.615	0.418

Table 7.3: Confidence levels obtained for a 200 GeV Higgs signal.

Scaling cross-section and luminosity for a 200 GeV Higgs

We have found that for the mass range of 115 to 500 GeV no discovery or exclusion can be claimed with the current integrated luminosity and assuming the Standard Model cross section for the Higgs signal. However, it is possible to study at what point an exclusion (a discovery) is *expected* by scanning the signal cross section (integrated luminosity). Figure 7.8 shows results of such scans for a Higgs mass of 200 GeV.

Figure 7.8(a) shows the $\mathrm{CL_s}$ curves for data, for the median value of the background-only hypothesis and for the median value of the signal-plus-background hypothesis. The background curve drops below 0.05 at 3.5, i.e. we *expect* to exclude a signal at $\sigma = 3.5 \cdot \sigma_{SM}$. The data showed an excess in this mass region (cf. Figure 7.5) and drops below 0.05 at a higher value of σ/σ_{SM}, i.e. data excludes a signal at $\sigma = 6.4 \cdot \sigma_{SM}$.

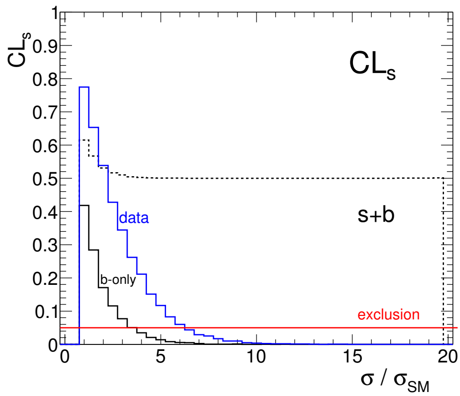

(a)

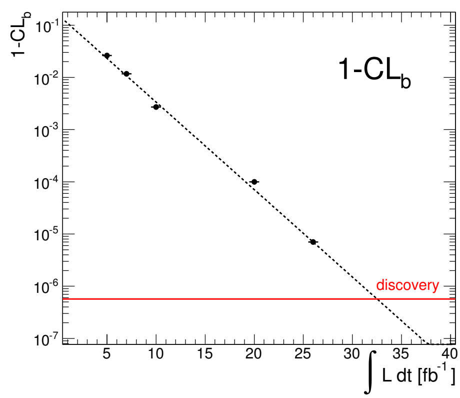

(b)

Figure 7.8: For a Higgs mass of 200 GeV a scan is performed over (a) signal cross section and (b) integrated luminosity. In both figures a line is drawn to indicate at what point an exclusion/a discovery is expected.

A scan over the integrated luminosity is computationally much more expensive than our cross section scan[7]. Figure 7.8(b) shows five obtained points. The results are fitted with an exponential curve which is extrapolated to higher values of integrated luminosity. A discovery is expected at 32.5 fb^{-1}.

Scaling cross-section for a Higgs in the mass range of 115 to 500 GeV

Exclusion analyses were performed in the Higgs mass range of 115 to 500 GeV. At each Higgs mass the expected and observed cross section scaling where an exclusion can be claimed was determined. In Figure 7.8(a) we showed where for a 200 GeV Higgs the *median* value of the background-only test statistic distribution dropped below 0.05. Likewise, the $\pm 1\sigma$ and $\pm 2\sigma$ bands of the background-only distribution were evaluated. Figure 7.7 shows the $\pm 1\sigma$ and $\pm 2\sigma$ bands as colored bands. These colored bands are translated into the final plot of our results in Figure 7.9. This shows, as a function of the Higgs mass, the cross section scaling where an exclusion can be claimed. The expected values are shown as the dashed line and colored bands for the median values and the $\pm 1\sigma$ and $\pm 2\sigma$ bands, respectively. The observed values are indicated with the solid line.

In the region of 160 to 190 GeV a large bump is observed. This is due to the large decrease of branching ratio for our decay channel in this mass region. Figure 2.10(b) shows that the $H \to WW$ decay channel is by far the dominant decay channel in this mass region. A decrease in $H \to ZZ$ branching ratio is also behind the increase visible at masses below 150 GeV. The increase at higher mass can not be explained by a decrease in branching ratio. In fact, this increase reflects the decreasing Higgs production cross section at higher masses (cf. Figure 2.10(a)).

[7]One has to run at least 10^7 toy MC experiments to find a value of $5.7 \cdot 10^{-7}$ for $1 - \mathrm{CL_b}$.

Our analysis shows to have the largest sensitivity for a Higgs signal with a mass around 200 GeV. It is also in this region that we observe an excess of events above 2σ from expectation. With updates of the analysis this excess needs to be studied further.

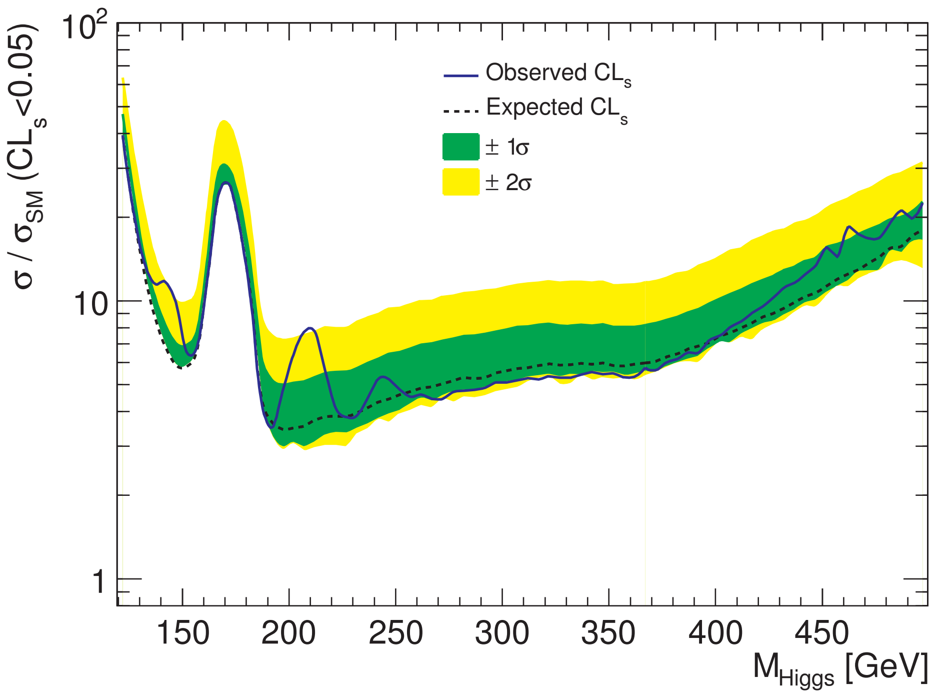

Figure 7.9: The expected and observed exclusion limits on the Higgs cross section as a function of the mass of the Higgs boson.

7.5 Conclusions

A search for the Standard Model (SM) Higgs boson was performed with 1 fb^{-1} of 7 TeV proton-proton collisions. The four muon final state was selected from data and simulation samples. Ten candidates were observed in data. The compatibility of the observed candidates with the background-only and signal-plus-background hypotheses was evaluated using toy Monte Carlo techniques. No discovery or exclusion of a SM Higgs in the mass range of 115 to 500 GeV can be claimed with the current integrated luminosity This is in accordance with expectation. With increasing luminosity a discovery in this decay channel alone can be expected at 32.5 fb^{-1}.

With the current integrated luminosity a 200 GeV Higgs is observed (expected) to be excluded at about 6.4 (3.5) times the SM cross section. Figure 7.9 shows the results of our exclusion analysis in a mass range of 115 to 500 GeV. Expectation and observation are in reasonable agreement and the features of this result are understood qualitatively.

While our exclusion results with a four muon final state do not reach the Standard Model cross section, the $H \to ZZ^* \to 4l$ results including electrons (i.e. 4μ, 4e and $2e2\mu$ final states) do approach this already with an integrated luminosity of 1 fb^{-1} [73]. In addition to this, several limits on a Standard Model with a fourth generation of heavy fermions can be set with the $4l$ decay channels [74]. In a Standard Model with a fourth generation the productions cross sections increase by a factor of about 4 to 9 for the high and low Higgs mass regions, respectively. This results in an increased sensitivity and therefore more stringent exclusion limits.

Outlook

Our $H \to ZZ^* \to 4\mu$ analysis can benefit from further developments. For example, increased sensitivity is (obviously) expected when the integrated luminosity of the data sample increases. In addition, the analysis could possibly benefit from further optimizations of the event selections. Because of the increasing understanding of the Muon Spectrometer muons could be added to the analysis which at this moment are not yet considered, such as standalone muons and calorimeter tagged muons. Also, the profile likelihood functions used in this analysis can be expanded to incorporate more information. This should provide better separation of the signal from the background. With an updated analysis the search for a Standard Model Higgs boson in a four muon final state can continue to be an exciting physics analysis. It will be very interesting, to say the least, to see the development of this analysis in the near future.

Chapter 8

Summary and conclusions

On the 30$^{\text{th}}$ of March, in the year 2010, experimental particle physics entered a new era. On that day, the large hadron collider (LHC) started delivering proton-proton collisions, at an unprecedented center of mass energy of 7 TeV, to the four experiments located around the LHC. At this record breaking collision energy the leading theory in particle physics, the Standard Model, can be studied at the TeV scale. Studied, confirmed, extended, or perhaps even falsified! The Standard Model precisely predicts the properties of elementary particles, and their interactions, at energy scales up to the TeV scale. The LHC provides an environment to test these predictions. In addition, a mechanism can be tested that is thought to account for particle masses: the Higgs mechanism. *If* this Higgs mechanism, proposed in 1964 by Higgs, Brout and Englert, is in fact how nature works *then* a new particle, the Higgs boson, must exist.

The Higgs boson is an unstable particle that can, in principle, be identified by studying its decay products. Up to the time of writing, it has not been observed at previous experiments nor at the LHC. This is not because people don't look hard enough, it is because the mass of the Higgs boson falls, unluckily, outside the kinematic range of previous particle accelerators. The value for the mass of the Higgs boson is not predicted by theory. With the mass of the Higgs boson also the expected decay products, or decay channels, vary. *If* the mass is known *then* several precise Standard Model predictions can be made about the decay channels. First step is therefore to discover the Higgs. Once discovered, one is able to test the Standard Model predictions. These two things were a great motivation to plan the LHC and its four experiments, some 25 years ago.

8

How do you detect a particle that was never observed before, with a detector that is unique in its kind, without actually knowing where to look? Two of the four LHC experiments, i.e. ATLAS and CMS, are so-called *general purpose* detectors, built to detect a wide range of possible physics signals, including Higgs decays. In this thesis we present results for a Higgs search with the Muon Spectrometer of ATLAS. Before such a search can be performed a lot of effort is spent on making sure that the detector performs the way it was *expected* to perform. The only way to do this is to use physics signals that have well known properties. These processes allow for a *calibration* of the detector. By studying and understanding these signals one gains confidence to look for new, and maybe also *unexpected*, signals.

ATLAS has shown excellent performance from the very first proton-proton collision onwards. The Muon Spectrometer (MS) of ATLAS forms no exception to this. This good performance is partly due to an elaborate commissioning effort using cosmic-ray data, before proton-proton collisions were delivered. The performance of the MS in cosmic-ray data is presented in Chapter 4. The relative momentum resolution is parametrized by

$$\frac{\sigma_{p_T}}{p_T} = \frac{P_0}{p_T} \oplus P_1 \oplus P_2 \cdot p_T,$$

where three contributing terms are identified. The uncertainty on the energy loss corrections is denoted by P_0, the multiple scattering term by P_1 and the intrinsic resolution term by P_2. The values obtained from a fit to cosmic-ray data (simulation) in the barrel region are 0.35 ± 0.02 (0.35) GeV, 0.038 ± 0.001 (0.035) % and $2.0 \pm 0.3\ 10^{-4}$ (1.2) GeV^{-1} for P_0, P_1 and P_2, respectively. The multiple scattering term is underestimated due to missing material in the simulated detector description. For muons with a transverse momentum, p_T, below 40 GeV the data show a good agreement with the predictions from simulation. At higher values of p_T the resolution in data is worse due to additional contributions from calibration, alignment and the description of the magnetic field.

Further performance studies were carried out with proton-proton collision data. Chapter 5 gives the results of our performance studies using $Z \to \mu^-\mu^+$ decays, one of the physics signals with well known properties that we referred to before. The reconstruction efficiency was evaluated using a tag-and-probe method. For combined muons the efficiency in data (simulation) was found to be 0.960 ± 0.003 (0.966 ± 0.002). The category of tight muons has an efficiency of 0.977 ± 0.003 (0.977 ± 0.002). This increase is mostly located in the $|\eta|$ region above 1.05 and at $|\eta| \approx 0$. In these regions the *tagger* algorithms recover part of the efficiency.

The $Z \to \mu^-\mu^+$ decays were also used to study the muon momentum scale and resolution. A description of the di-muon invariant mass distribution was constructed and fitted to simulation. Subsequently, detector effects were added to the model and fits to distributions from data were performed. Both the momentum scale and the resolution were studied using either combined (CB), standalone (SA) or Inner Detector (ID) track parameters. The momentum scale with ID and CB parameters showed an asymmetry in positive and negative endcaps that is mainly attributed to misalignments in the Inner Detector. The resolution for CB, SA and ID parameters shows higher values in data for the full η range. This is partially due to missing material in the detector description used in simulation. Remaining misalignments and the symmetric magnetic field description also contribute to the observed discrepancies. The measured resolutions for CB parameters in the barrel region are in agreement with our cosmic-ray results.

An observation of di-muon final states in heavy-ion (lead-lead) collisions was presented in Chapter 6 of this thesis. The production cross sections of $J/\psi \to \mu^-\mu^+$ and $Z \to \mu^-\mu^+$ decays were studied as a function of the event multiplicity, or centrality. A decreasing cross section was observed for J/ψ decays, beyond statistical and systematic uncertainties. This decrease can be explained in terms of J/ψ suppression by the quark-gluon-plasma. No decrease was observed in the Z decays, although the limited statistics prevent drawing definite conclusions in this case.

Finally, in Chapter 7 of this thesis, we presented a search for the Standard Model Higgs boson in a final state with four muons. We used 1 fb^{-1} of the 2011 ATLAS data-set for this analysis. Figure 8.1 shows one of the candidates that was observed in data. In total 10 candidates were observed and 5.52 were expected from Standard Model background processes. The significance of this excess was evaluated in the mass range of 115 to 500 GeV. We found that no discovery or exclusion can be claimed. The signal cross section was scaled to determine at what point an exclusion is expected to be claimed. The best sensitivity is at a Higgs mass of 200 GeV where we expect to exclude a signal at 3.5 times the Standard Model cross section. The observed limit for this mass is 6.4 times the Standard Model cross section. The further development of this signal, if more data is analyzed and other Higgs channels are added, will be exciting next steps in a decisive phase of the search for this elusive particle. Will the era of the Higgs hypothesis end soon? Only time (and LHC data) will tell.

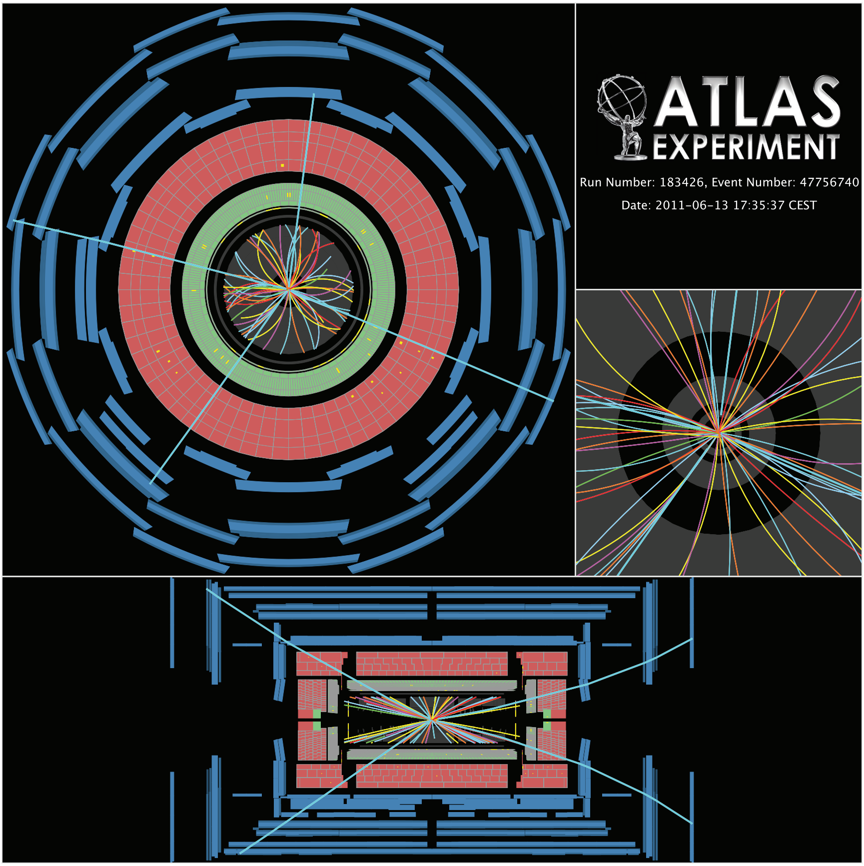

Figure 8.1: One of the possible Higgs candidates with a four muon final state. The four muon invariant mass is 449 GeV. The mass of the primary and secondary Z candidate is 91.4 GeV and 89.5 GeV, respectively.

8

Appendix A

Momentum resolution

A.1 Uncertainties

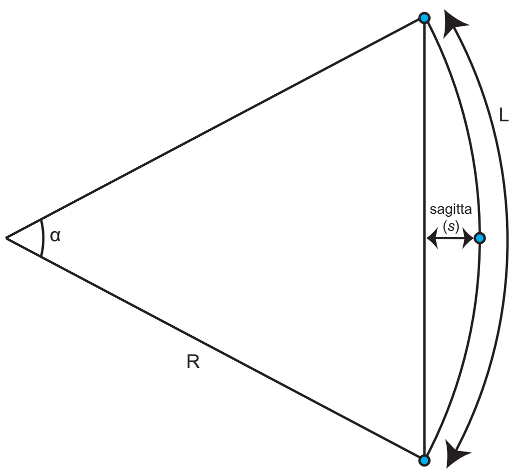

Figure A.1: The definition of the sagitta

The basic equation for the momentum of a charged particle in a magnetic field B is

$$p = q\ R\ B = 0.3\ R[m]\ B[T]. \tag{A.1}$$

The sagitta s is defined as

$$s = R(1 - \cos\frac{\alpha}{2}) \approx \frac{R\alpha^2}{8}, \tag{A.2}$$

where the cosine series expansion was applied.

Using Equation A.2 we can rewrite Equation A.1 as

$$p = 0.3\ B\ \frac{R^2\alpha^2}{8s}. \tag{A.3}$$

When evaluating the momentum resolution we make use of the error propagation formula, which is

$$\sigma_p^2 = \left(\frac{\partial p}{\partial B}\right)^2 \sigma_B^2 + \left(\frac{\partial p}{\partial R}\right)^2 \sigma_R^2 + \left(\frac{\partial p}{\partial \alpha}\right)^2 \sigma_\alpha^2 + \left(\frac{\partial p}{\partial s}\right)^2 \sigma_s^2. \tag{A.4}$$

After some algebra and rewriting this gives us

$$\left(\frac{\sigma_p}{p}\right)^2 = \left(\frac{\sigma_B}{B}\right)^2 + \left(2\frac{\sigma_R}{R}\right)^2 + \left(2\frac{\sigma_\alpha}{\alpha}\right)^2 + \left(\frac{\sigma_s}{s}\right)^2. \tag{A.5}$$

A.2 Comparing $\sigma(s)$ to $\sigma(p_T)/p_T$

If one want to compare results from the sagitta analysis to results from the momentum analysis from Chapter 4 the following relation should be used [45]:

$$\frac{\sigma(p_T)}{p_T} = \frac{\frac{1}{p_{Treco}} - \frac{1}{p_{Ttrue}}}{\frac{1}{p_{Ttrue}}} = \frac{p_{Ttrue} - p_{Treco}}{p_{Treco}}. \tag{A.6}$$

The definition for $\sigma(p_T)$

$$\sigma(p_T) = p_{Ttrue} - p_{Treco}, \tag{A.7}$$

leads to

$$\frac{\sigma(p_T)}{p_{Treco}} = \frac{p_{Ttrue} - p_{Treco}}{p_{Treco}} = \frac{\sigma(p_T)}{p_T}. \tag{A.8}$$

And similarly for $\sigma(s) = \sigma\left(\frac{1}{p_T}\right)$ with the definition

$$\sigma\left(\frac{1}{p_T}\right) = \frac{1}{p_{Ttrue}} - \frac{1}{p_{Treco}}, \tag{A.9}$$

leads to

$$\sigma\left(\frac{1}{p_T}\right) = \frac{1}{p_{Ttrue}}\left(\frac{\frac{1}{p_{Ttrue}} - \frac{1}{p_{Treco}}}{\frac{1}{p_{Ttrue}}}\right) = \frac{1}{p_{Ttrue}}\frac{\sigma(p_T)}{p_T}. \tag{A.10}$$

Combining Equations A.8 and A.10 gives

$$\sigma(s) = \sigma\left(\frac{1}{p_T}\right) = \frac{\sigma(p_T)}{p_{Ttrue}\, p_{Treco}} \approx \frac{\sigma(p_T)}{p_T^2} = \frac{1}{p_T}\frac{\sigma(p_T)}{p_T}, \tag{A.11}$$

bringing us to the end result

$$p_T\ \sigma(s) = \frac{\sigma(p_T)}{p_T}. \tag{A.12}$$

This helps when comparing Equations 4.1 and 4.4.

Appendix B

Samples used for Higgs studies

Signal

mc10_7TeV.116611.PowHegPythia_ggH130_ZZ4lep.merge.NTUP_HSG2.e773_s933_s946_r2302_r2300_p598_tid430426_00
mc10_7TeV.116612.PowHegPythia_ggH200_ZZ4lep.merge.NTUP_HSG2.e773_s933_s946_r2302_r2300_p598_tid430440_00
mc10_7TeV.116761.PowHegPythia_ggH110_ZZ4lep.merge.NTUP_HSG2.e773_s933_s946_r2302_r2300_p598_tid430422_00
mc10_7TeV.116762.PowHegPythia_ggH115_ZZ4lep.merge.NTUP_HSG2.e773_s933_s946_r2302_r2300_p598_tid430423_00
mc10_7TeV.116763.PowHegPythia_ggH120_ZZ4lep.merge.NTUP_HSG2.e773_s933_s946_r2302_r2300_p598_tid430424_00
mc10_7TeV.116764.PowHegPythia_ggH125_ZZ4lep.merge.NTUP_HSG2.e773_s933_s946_r2302_r2300_p598_tid430425_00
mc10_7TeV.116765.PowHegPythia_ggH135_ZZ4lep.merge.NTUP_HSG2.e773_s933_s946_r2302_r2300_p598_tid430427_00
mc10_7TeV.116766.PowHegPythia_ggH140_ZZ4lep.merge.NTUP_HSG2.e773_s933_s946_r2302_r2300_p598_tid430428_00
mc10_7TeV.116767.PowHegPythia_ggH145_ZZ4lep.merge.NTUP_HSG2.e773_s933_s946_r2302_r2300_p598_tid430429_00
mc10_7TeV.116768.PowHegPythia_ggH150_ZZ4lep.merge.NTUP_HSG2.e773_s933_s946_r2302_r2300_p598_tid430430_00
mc10_7TeV.116769.PowHegPythia_ggH155_ZZ4lep.merge.NTUP_HSG2.e773_s933_s946_r2302_r2300_p598_tid430431_00
mc10_7TeV.116770.PowHegPythia_ggH160_ZZ4lep.merge.NTUP_HSG2.e773_s933_s946_r2302_r2300_p598_tid430432_00
mc10_7TeV.116771.PowHegPythia_ggH165_ZZ4lep.merge.NTUP_HSG2.e773_s933_s946_r2302_r2300_p598_tid430433_00
mc10_7TeV.116772.PowHegPythia_ggH170_ZZ4lep.merge.NTUP_HSG2.e773_s933_s946_r2302_r2300_p598_tid430434_00
mc10_7TeV.116773.PowHegPythia_ggH175_ZZ4lep.merge.NTUP_HSG2.e773_s933_s946_r2302_r2300_p598_tid430435_00
mc10_7TeV.116774.PowHegPythia_ggH180_ZZ4lep.merge.NTUP_HSG2.e773_s933_s946_r2302_r2300_p598_tid430436_00
mc10_7TeV.116775.PowHegPythia_ggH185_ZZ4lep.merge.NTUP_HSG2.e773_s933_s946_r2302_r2300_p598_tid430437_00
mc10_7TeV.116776.PowHegPythia_ggH190_ZZ4lep.merge.NTUP_HSG2.e773_s933_s946_r2302_r2300_p598_tid430438_00
mc10_7TeV.116777.PowHegPythia_ggH195_ZZ4lep.merge.NTUP_HSG2.e773_s933_s946_r2302_r2300_p598_tid430439_00
mc10_7TeV.116779.PowHegPythia_ggH210_ZZ4lep.merge.NTUP_HSG2.e773_s933_s946_r2302_r2300_p598_tid430441_00
mc10_7TeV.116780.PowHegPythia_ggH220_ZZ4lep.merge.NTUP_HSG2.e773_s933_s946_r2302_r2300_p598_tid430442_00
mc10_7TeV.116781.PowHegPythia_ggH240_ZZ4lep.merge.NTUP_HSG2.e773_s933_s946_r2302_r2300_p598_tid430443_00
mc10_7TeV.116782.PowHegPythia_ggH260_ZZ4lep.merge.NTUP_HSG2.e773_s933_s946_r2302_r2300_p598_tid430444_00
mc10_7TeV.116783.PowHegPythia_ggH280_ZZ4lep.merge.NTUP_HSG2.e773_s933_s946_r2302_r2300_p598_tid430445_00
mc10_7TeV.116784.PowHegPythia_ggH300_ZZ4lep.merge.NTUP_HSG2.e773_s933_s946_r2302_r2300_p598_tid430446_00
mc10_7TeV.116785.PowHegPythia_ggH320_ZZ4lep.merge.NTUP_HSG2.e773_s933_s946_r2302_r2300_p598_tid430447_00
mc10_7TeV.116786.PowHegPythia_ggH340_ZZ4lep.merge.NTUP_HSG2.e773_s933_s946_r2302_r2300_p598_tid430448_00
mc10_7TeV.116787.PowHegPythia_ggH360_ZZ4lep.merge.NTUP_HSG2.e773_s933_s946_r2302_r2300_p598_tid430449_00
mc10_7TeV.116788.PowHegPythia_ggH380_ZZ4lep.merge.NTUP_HSG2.e773_s933_s946_r2302_r2300_p598_tid430450_00
mc10_7TeV.116789.PowHegPythia_ggH400_ZZ4lep.merge.NTUP_HSG2.e773_s933_s946_r2302_r2300_p598_tid430451_00
mc10_7TeV.116790.PowHegPythia_ggH420_ZZ4lep.merge.NTUP_HSG2.e773_s933_s946_r2302_r2300_p598_tid430452_00
mc10_7TeV.116791.PowHegPythia_ggH440_ZZ4lep.merge.NTUP_HSG2.e773_s933_s946_r2302_r2300_p598_tid430453_00

mc10_7TeV.116792.PowHegPythia_ggH460_ZZ4lep.merge.NTUP_HSG2.e773_s933_s946_r2302_r2300_p598_tid430454_00
mc10_7TeV.116793.PowHegPythia_ggH480_ZZ4lep.merge.NTUP_HSG2.e773_s933_s946_r2302_r2300_p598_tid430455_00
mc10_7TeV.116794.PowHegPythia_ggH500_ZZ4lep.merge.NTUP_HSG2.e773_s933_s946_r2302_r2300_p598_tid430456_00
mc10_7TeV.116795.PowHegPythia_ggH520_ZZ4lep.merge.NTUP_HSG2.e773_s933_s946_r2302_r2300_p598_tid430457_00
mc10_7TeV.116796.PowHegPythia_ggH540_ZZ4lep.merge.NTUP_HSG2.e773_s933_s946_r2302_r2300_p598_tid430458_00
mc10_7TeV.116797.PowHegPythia_ggH560_ZZ4lep.merge.NTUP_HSG2.e773_s933_s946_r2302_r2300_p598_tid430459_00
mc10_7TeV.116798.PowHegPythia_ggH580_ZZ4lep.merge.NTUP_HSG2.e773_s933_s946_r2302_r2300_p598_tid430460_00
mc10_7TeV.116799.PowHegPythia_ggH600_ZZ4lep.merge.NTUP_HSG2.e773_s933_s946_r2302_r2300_p598_tid430461_00

Backgrounds

mc10_7TeV.109292.Pythiazz4l_3MultiLeptonFilterElecMu.merge.NTUP_HSG2.e632_s933_s946_r2302_r2300_p537_tid362018_00
mc10_7TeV.109345.T1_McAtNlo_Jimmy_2LeptonsMll60GeV.merge.NTUP_HSG2.e598_s933_s946_r2302_r2300_p598_tid430219_00
mc10_7TeV.109345.T1_McAtNlo_Jimmy_2LeptonsMll60GeV.merge.NTUP_HSG2.e598_s933_s946_r2302_r2300_p598_tid430220_00
mc10_7TeV.116965.AlpgenHWfZmumubbNp0_4LepM.merge.NTUP_HSG2.e773_s933_s946_r2302_r2300_p537_tid359107_00
mc10_7TeV.116966.AlpgenHWfZmumubbNp1_4LepM.merge.NTUP_HSG2.e773_s933_s946_r2302_r2300_p537_tid359108_00
mc10_7TeV.116967.AlpgenHWfZmumubbNp2_4LepM.merge.NTUP_HSG2.e773_s933_s946_r2302_r2300_p537_tid359109_00
mc10_7TeV.116968.AlpgenHWfZmumubbNp3_4LepM.merge.NTUP_HSG2.e773_s933_s946_r2302_r2300_p537_tid359110_00
mc10_7TeV.116955.AlpgenHWfZmumubbNp0_Veto4LepM_Pass3Lep.merge.NTUP_HSG2.e773_s933_s946_r2302_r2300_p537_tid359115_00
mc10_7TeV.116956.AlpgenHWfZmumubbNp1_Veto4LepM_Pass3Lep.merge.NTUP_HSG2.e773_s933_s946_r2302_r2300_p537_tid359116_00
mc10_7TeV.116957.AlpgenHWfZmumubbNp2_Veto4LepM_Pass3Lep.merge.NTUP_HSG2.e773_s933_s946_r2302_r2300_p537_tid359117_00
mc10_7TeV.116958.AlpgenHWfZmumubbNp3_Veto4LepM_Pass3Lep.merge.NTUP_HSG2.e773_s933_s946_r2302_r2300_p537_tid359118_00
mc10_7TeV.107660.AlpgenJimmyZmumuNp0_pt20.merge.NTUP_HSG2.e737_s933_s946_r2302_r2300_p598_tid430185_00
mc10_7TeV.107661.AlpgenJimmyZmumuNp1_pt20.merge.NTUP_HSG2.e737_s933_s946_r2302_r2300_p598_tid430186_00
mc10_7TeV.107662.AlpgenJimmyZmumuNp2_pt20.merge.NTUP_HSG2.e737_s933_s946_r2302_r2300_p598_tid430187_00
mc10_7TeV.107663.AlpgenJimmyZmumuNp3_pt20.merge.NTUP_HSG2.e737_s933_s946_r2302_r2300_p598_tid430188_00
mc10_7TeV.107664.AlpgenJimmyZmumuNp4_pt20.merge.NTUP_HSG2.e737_s933_s946_r2302_r2300_p598_tid430189_00
mc10_7TeV.107665.AlpgenJimmyZmumuNp5_pt20.merge.NTUP_HSG2.e737_s933_s946_r2302_r2300_p598_tid430190_00
mc10_7TeV.106047.PythiaZmumu_no_filter.merge.NTUP_HSG2.e574_s933_s946_r2302_r2300_p598_tid430218_00

Appendix C

More on the profile likelihood function

C

The analysis presented in Chapter 7 uses profile likelihood functions in the definition of its test statistic:

$$-2\ln(Q) = -2\ln\left(\frac{\mathcal{L}_{s+b}(\mu_s = 1, \hat{\hat{\theta}}_{b_{s+b}})}{\mathcal{L}_b(\mu_s = 0, \hat{\hat{\theta}}_{b_b})}\right). \tag{C.1}$$

The profile likelihood functions used in Equation C.1 are obtained by scaling the background template normalization, a method used before for several LEP and Tevatron results (e.g. ref. [19]). The background scaling that maximizes the likelihood is used in Equation C.1. The motivation to perform this scaling comes from the uncertainty on the background normalization, which is the dominant systematic in our study [71]. Another way to incorporate this uncertainty is by smearing the background template by a Gaussian function when generating the toy MC distributions. At the time of doing the analysis the technical implementation of this alternative was not yet available and we used the profile likelihood method. Here we evaluate how this affects our end result: the exclusion plot in Figure 7.9.

We compare the profile likelihood functions (PLFs) to the regular likelihood functions (LFs), i.e. setting the background scaling to 1, for three values of the Higgs mass assuming Standard Model cross sections. Table C.1 shows the results for $-2\ln(Q)$, $\mathrm{CL_s}$ and $\mathrm{CL_b}$ for data and the median values of the b-only and s+b hypotheses.

The $\mathrm{CL_s}$ values for the b-only median value show little difference between PLFs and LFs for the three mass points. For data we observe a significant difference between PLF and LF for a 200 GeV Higgs: 0.8204 vs 0.7854. The values for $-2\ln(Q)$ show a similar discrepancy. This is the mass region where we observed an excess of events in the four muon invariant mass plot (cf. Figure 7.5). It seems that the PLF method is less sensitive to this excess than the LF method. One could imagine that the excess results in an overestimation of the background normalization, therefore decreasing the sensitivity to signal. This hypothesis is supported by the values for the median of the s+b hypothesis: $-2\ln(Q)$ is systematically lower for LF than for PLF, indicating more signal-like distributions for the LF method.

		150 GeV		200 GeV		300 GeV	
		LF	PLF	LF	PLF	LF	PLF
Data	$-2\ln Q$	-0.16	0.16	-2.70	-1.81	1.07	1.12
	$\mathrm{CL_s}$	0.6468	0.6380	0.8204	0.7854	0.5754	0.5613
	$\mathrm{CL_b}$	0.8381	0.8819	0.9737	0.9396	0.4022	0.2247
Median b-only hypothesis	$-2\ln Q$	1.01	1.01	1.22	1.17	0.87	0.86
	$\mathrm{CL_s}$	0.5988	0.6010	0.4181	0.4266	0.5907	0.5933
Median s+b hypothesis	$-2\ln Q$	0.18	0.27	-0.59	-0.54	-0.07	-0.06
	$\mathrm{CL_b}$	0.8032	0.7938	0.8320	0.8085	0.7590	0.7549

Table C.1: Comparison of results for three Higgs masses obtained using a likelihood function (LF) or profile likelihood (PLF).

However, what we truly wish to evaluate in the context of our study is how our choice for PLF influences the observed and expected exclusion. Table C.2 shows the $\mathrm{CL_s}$ values for a 200 GeV Higgs and the relevant signal cross sections. The observed and expected exclusion limits are obtained by interpolating these numbers and evaluating at which point $\mathrm{CL_s} = 0.05$.

	$\sigma/\sigma_{SM} = 3.0$		3.5		6.0		6.5	
	LF	PLF	LF	PLF	LF	PLF	LF	PLF
$\mathrm{CL_s}$ data	-	-	-	-	0.0603	0.0652	0.0427	0.0466
$\mathrm{CL_s}$ median b-only	0.0694	0.0767	0.0468	0.0493	-	-	-	-

Table C.2: Comparison of results for a 200 GeV Higgs obtained using a likelihood function (LF) or profile likelihood (PLF).

For a 200 GeV Higgs the observed exclusion limits for σ/σ_{SM} in data when using PLFs and LFs are 6.4 and 6.3, respectively. For the expected exclusion this is 3.5 and 3.4 for PLFs and LFs, respectively. We therefore conclude that the limits that we obtained from PLFs will be in agreement with limits obtained from LFs. We do acknowledge, as was mentioned before, that more advanced methods exist that can be used to incorporate the uncertainty on the background normalization in our analysis. This is a likely improvement for future updates of the presented Higgs boson search.

References

R

[1] A. Petersen, *The Philosophy of Niels Bohr*, Bulletin of the Atomic Scientists **19** (1963) 8–14.

[2] F. Close, *Particle Phyics: a very short introduction.* Oxford University Press, 2004.

[3] F. Zwicky, *Die Rotverschiebung von extragalaktischen Nebeln*, Helvetica Physica Acta **6** (1933) 110–127.

[4] V. C. Rubin et al., *Rotational properties of 21 SC galaxies with a large range of luminosities and radii, from NGC 4605 (R = 4kpc) to UGC 2885 (R = 122kpc)*, Astrophysical Journal **238** (1980) 471–487.

[5] F. Halzen and A. D. Martin, *Quarks and Leptons.* John Wiley & Sons, Inc., 1985.

[6] D. Griffiths, *Introduction to Elementary Particles.* John Wiley & Sons, Inc., 1987.

[7] R. K. Ellis, W. J. Stirling, and B. R. Webber, *QCD and Collider Physics.* Cambridge University Press, 1996.

[8] T.-P. Cheng and L.-F. Li, *Gauge theory of elementary particle physics.* Oxford University Press, 1984.

[9] F. Englert and R. Brout, *Broken Symmetry and the Mass of Gauge Vector Mesons*, Phys. Rev. Lett. **13** (Aug, 1964) 321–323.

[10] P. W. Higgs, *Broken Symmetries and the Masses of Gauge Bosons*, Phys. Rev. Lett. **13** (Oct, 1964) 508–509.

[11] G. S. Guralnik, C. R. Hagen, and T. W. B. Kibble, *Global Conservation Laws and Massless Particles*, Phys. Rev. Lett. **13** (Nov, 1964) 585–587.

[12] *SPS Operation Home Page*, `http://ab-dep-op-sps.web.cern.ch/ab-dep-op-sps/`.

[13] G. Arnison et al., *Experimental observation of isolated large transverse energy electrons with associated missing energy at*, Physics Letters B **122** (1983) no. 1, 103 – 116.
`http://www.sciencedirect.com/science/article/pii/0370269383911772`.

[14] G. Arnison et al., *Experimental observation of lepton pairs of invariant mass around 95 GeV/c^2 at the CERN SPS collider*, Physics Letters B **126** (1983) no. 5, 398 – 410.
`http://www.sciencedirect.com/science/article/pii/0370269383901880`.

[15] K. Nakamura and Particle Data Group, *Review of Particle Physics*, Journal of Physics G: Nuclear and Particle Physics **37** (2010) no. 7A, 075021.
`http://stacks.iop.org/0954-3899/37/i=7A/a=075021`.

[16] C. S. Wu, E. Ambler, R. W. Hayward, D. D. Hoppes, and R. P. Hudson, *Experimental Test of Parity Conservation in Beta Decay*, Phys. Rev. **105** (Feb, 1957) 1413–1415.

[17] R. L. Garwin, L. M. Lederman, and M. Weinrich, *Observations of the Failure of Conservation of Parity and Charge Conjugation in Meson Decays: the Magnetic Moment of the Free Muon*, Phys. Rev. **105** (Feb, 1957) 1415–1417.

[18] LEP Working Group for Higgs boson searches Collaboration, R. Barate et al., *Search for the standard model Higgs boson at LEP*, Phys. Lett. **B565** (2003) 61–75, `arXiv:hep-ex/0306033`.

[19] The CDF and D0 Collaborations, New Phenomena & Higgs Working Group, *Combined CDF and D0 Upper Limits on Standard Model Higgs Boson Production with up to 8.6 fb^{-1} of Data*, `arXiv:1107.5518 [hep-ex]`.

[20] T. Hambye and K. Riesselmann, *Matching conditions and Higgs mass upper bounds revisited*, Phys. Rev. **D55** (1997) 7255–7262, `arXiv:hep-ph/9610272`.

[21] Martin, A. D. and Stirling, W. J. and Thorne, R. S. and Watt, G., *Parton distributions for the LHC*, Eur. Phys. J. **C63** (2009) 189–285, `arXiv:0901.0002 [hep-ph]`.

[22] Drell, Sidney D. and Yan, Tung-Mow, *Massive Lepton-Pair Production in Hadron-Hadron Collisions at High Energies*, Phys. Rev. Lett. **25** (Sep, 1970) 902.

[23] *Athena core software*, `http://atlas-computing.web.cern.ch/atlas-computing/packages/athenaCore/athenaCore.php`.

[24] S. Agostinelli et al., *G4 - A simulation toolkit*, Nuclear Instruments and Methods in Physics Research Section A: Accelerators, Spectrometers, Detectors and Associated Equipment **506** (2003) no. 3, 250 – 303.

[25] K. Assamagan et al., *The ATLAS Monte Carlo Project*, Tech. Rep. ATL-SOFT-INT-2010-002, CERN, Geneva, Feb, 2010.

[26] J. C. Collins, D. E. Soper, and G. F. Sterman, *Factorization of Hard Processes in QCD*, Adv.Ser.Direct.High Energy Phys. **5** (1988) 1–91.

[27] M. Gosselink, *Radiating Top Quarks.* PhD thesis, Nikhef, Amsterdam, 2010.

[28] LHC Higgs Cross Section Working Group, S. Dittmaier, C. Mariotti, G. Passarino, and R. Tanaka (Eds.), *Handbook of LHC Higgs Cross Sections: 1. Inclusive Observables*, `arXiv:1101.0593 [hep-ph]`.

[29] S. Alioli, P. Nason, C. Oleari, and E. Re, *NLO Higgs boson production via gluon fusion matched with shower in POWHEG*, JHEP **04** (2009) 002, `arXiv:0812.0578 [hep-ph]`.

[30] ATLAS Collaboration, G. Aad et al., *The ATLAS Experiment at the CERN Large Hadron Collider*, JINST **3** (2008) S08003.

[31] Atlas Collaboration, G. Aad et al., *Performance of the ATLAS Trigger System in 2010*, `arXiv:1110.1530 [hep-ex]`.

[32] J. Stelzer, *Trigger Operation Public Results*, `https://twiki.cern.ch/twiki/bin/view/AtlasPublic/TriggerOperationPublicResults`.

[33] J. Adelman, *Public TRT plots for collision data*, `https://twiki.cern.ch/twiki/bin/view/AtlasPublic/TRTPublicResults`.

[34] N. Van Eldik, *The ATLAS muon spectrometer: calibration and pattern recognition.* PhD thesis, Nikhef, Amsterdam, 2007.

[35] A. Koutsman, *On the road to supersymmetry with ATLAS.* PhD thesis, Nikhef, Amsterdam, 2011.

[36] P. Hough, *Machine Analysis of Bubble Chamber Pictures*, in *International Conference on High Energy Accelerators and Instrumentation, CERN.* 1959.

[37] J. Snuverink, *The ATLAS muon spectrometer: commissioning and tracking.* PhD thesis, Nikhef, Amsterdam, 2009.

[38] P. Kluit, *Muon Reconstruction Documentation - The* `MUID` *Muon Collection*, `https://twiki.cern.ch/twiki/bin/view/AtlasProtected/MuidMuonCollection`.

[39] J. F. Laporte, *Muon Reconstruction Documentation - The* `STACO` *Muon Collection*, `https://twiki.cern.ch/twiki/bin/view/AtlasProtected/StacoMuonCollection`.

[40] Z. Van Kesteren, *Identification of muons in ATLAS.* PhD thesis, Nikhef, Amsterdam, 2010.

[41] M. Raas, *Muon Reconstruction Documentation - The* `CALO` *Muon Collection*, `https://twiki.cern.ch/twiki/bin/viewauth/Atlas/CaloMuonContainer`.

[42] ATLAS Collaboration, G. Aad et al., *Commissioning of the ATLAS Muon Spectrometer with cosmic rays*, The European Physical Journal C - Particles and Fields **70** 875–916.

[43] P. Branchini, F. Ceradini, S. Di Luise, M. Iodice, and F. Petrucci, *Global Time Fit for Tracking in an Array of Drift Cells: The Drift Tubes of the ATLAS Experiment*, Nuclear Science, IEEE Transactions on **55** (feb., 2008) 620 –627.

[44] *ATLAS muon spectrometer: Technical Design Report.* Technical Design Report ATLAS. CERN, Geneva, 1997. distribution.

[45] ATLAS Collaboration, G. Aad et al., *Expected Performance of the ATLAS Experiment - Detector, Trigger and Physics*, `arXiv:0901.0512 [hep-ex]`.

[46] ATLAS Collaboration, G. Aad et al., *Studies of the performance of the ATLAS detector using cosmic-ray muons*, `arXiv:1011.6665 [hep-ex]`.

[47] P. Kluit, R. Aben, and E. van der Poel, *Sagitta analysis code*, `http://alxr.usatlas.bnl.gov/lxr-stb4/source/atlas/MuonSpectrometer/MuonCalib/MuonCalibExtraTree/MuonCalibExtraNtuple/src/SagittaAnalysis.cxx`.

[48] A. Dar, *Atmospheric Neutrinos, Astrophysical Neutrons, and Proton-Decay Experiments*, Phys. Rev. Lett. **51** (Jul, 1983) 227–230.

[49] J. Meyer, *Muon Geometry and Performance Updates*, `https://indico.cern.ch/getFile.py/access?contribId=7&resId=0&materialId=slides&confId=142697`.

[50] T. Cornelissen, M. Elsing, I. Gavrilenko, W. Liebig, and A. Salzburger, *Single Track Performance of the Inner Detector New Track Reconstruction (NEWT)*, Tech. Rep. ATL-INDET-PUB-2008-002. ATL-COM-INDET-2008-004, CERN, Geneva, Mar, 2008.

[51] R. Sandstroem, *Quality definitions MUID*, `https://twiki.cern.ch/twiki/bin/view/AtlasProtected/QualityDefinitionMuid`.

[52] P. Jussel, *MuGirl reconstruction software*, `https://twiki.cern.ch/twiki/bin/viewauth/Atlas/MuGirl`.

[53] *Determination of the muon reconstruction efficiency in ATLAS at the Z resonance in proton-proton collisons at* $\sqrt{s}$*=7 TeV*, Tech. Rep. ATLAS-CONF-2011-008, CERN, Geneva, Feb, 2011.

[54] *Muon reconstruction efficiency in reprocessed 2010 LHC proton-proton collision data recorded with the ATLAS detector*, Tech. Rep. ATLAS-CONF-2011-063, CERN, Geneva, Apr, 2011.

[55] W. Verkerke and D. Kirby, *The RooFit toolkit for data modeling*, `http://roofit.sourceforge.net/`.

R

[56] K. Mueller, *Dimuon mass resolution fit optimization*, https://indico.cern.ch/getFile.py/access?contribId=1&resId=1&materialId=slides&confId=111098.

[57] L. Skinnari, A. Morley, and S. Marti, *Inner Detector Alignment Performance Plots using $Z \to \mu\mu$*, Tech. Rep. ATL-COM-PHYS-2011-865, CERN, Geneva, Jul, 2011.

[58] J. Stahlman, *Rel. 17 Alignment Validation using $Z \to \mu\mu$*, https://indico.cern.ch/getFile.py/access?contribId=11&resId=0&materialId=slides&confId=147770.

[59] P. Bruckman De Renstrom, D. Dul, S. Marti, and A. Morley, *Inner detector alignment performance plots*, Tech. Rep. ATL-COM-PHYS-2011-643, CERN, Geneva, Jun, 2011.

[60] W. Liebig and O. Kortner, *Muon Performance Public Plots - ID resolution vs eta*, https://twiki.cern.ch/twiki/pub/AtlasPublic/MuonPerformancePublicPlots/res_ID_vs_eta.png.

[61] P.-F. Giraud, *Muon alignment validation for release 17*, https://indico.cern.ch/getFile.py/access?contribId=48&sessionId=8&resId=0&materialId=slides&confId=141677.

[62] *Relativistic Heavy Ion Collider at Brookhaven National Lab*, http://www.bnl.gov/rhic/.

[63] ALICE Collaboration, K. Aamodt and other, *The ALICE experiment at the CERN LHC*, Journal of Instrumentation **3** (Aug, 2008) .

[64] Atlas Collaboration, G. Aad et al., *Measurement of the centrality dependence of J/ψ yields and observation of Z production in lead-lead collisions with the ATLAS detector at the LHC*, Phys. Lett. **B697** (2011) 294–312.

[65] G. Aad et al., *Luminosity Determination in pp Collisions at sqrt(s) = 7 TeV using the ATLAS Detector in 2011*, Tech. Rep. ATLAS-CONF-2011-116, CERN, Geneva, Jul, 2011.

[66] J. M. Campbell, R. K. Ellis, and C. Williams, *Vector boson pair production at the LHC*, JHEP **07** (2011) 018, arXiv:1105.0020 [hep-ph].

[67] J. Butterworth, E. Dobson, U. Klein, B. Mellado Garcia, T. Nunnemann, J. Qian, D. Rebuzzi, and R. Tanaka, *Single Boson and Diboson Production Cross Sections in pp Collisions at $\sqrt{s}$=7 TeV*, Tech. Rep. ATL-COM-PHYS-2010-695, CERN, Geneva, Aug, 2010.

[68] A. Di Simone, *Higgs Sub Group 2 DPD production*, https://twiki.cern.ch/twiki/bin/view/AtlasProtected/HSG2DPDs.

[69] L. Skinnari et al., *Update on muon isolation studies*, https://indico.cern.ch:443/getFile.py/access?contribId=0&resId=0&materialId=slides&confId=140775.

[70] *Atlantis event display for ATLAS*, http://www.hep.ucl.ac.uk/atlas/atlantis.

[71] *Combination of the Searches for the Higgs Boson in 1 fb^{-1} of Data Taken with the ATLAS Detector at 7 TeV Center-of-Mass Energy*, Tech. Rep. ATLAS-CONF-2011-112, CERN, Geneva, Aug, 2011.

[72] A. L. Read, *Presentation of search results: The CL(s) technique*, J. Phys. **G28** (2002) 2693–2704.

[73] *Search for the Standard Model Higgs boson in the decay channel $H \to ZZ^* \to 4l$ with the ATLAS detector*, Tech. Rep. ATLAS-CONF-2011-131, CERN, Geneva, Aug, 2011.

[74] G. Passarino, C. Sturm, and S. Uccirati, *Complete Electroweak Corrections to Higgs production in a Standard Model with four generations at the LHC*, arXiv:1108.2025 [hep-ph].

R

Samenvatting

Muon prestatie studies in ATLAS op weg naar een zoektocht naar het Standaard Model Higgs boson

Op 30 maart 2010 heeft de experimentele deeltjes fysica een nieuw tijdperk betreden. Op die dag leverde de "large hadron collider" (LHC) voor de eerste keer proton-proton botsingen, bij een niet eerder vertoonde botsingsenergie van 7 TeV, aan de vier experimenten rond de LHC. Bij deze recordbrekende botsingsenergie kan de leidende theorie van de deeltjes fysica, het Standaard Model, bestudeerd worden bij de TeV schaal. Bestudeerd, bevestigd, uitgebreid, of misschien zelfs weerlegd! Het Standaard Model doet precieze voorspellingen van de eigenschappen van elementaire deeltjes, en hun onderlinge interacties, bij energieën tot de TeV schaal. De LHC creëert een omgeving waarin deze voorspellingen getest kunnen worden. Bovendien kan een mechanisme getest worden wat verantwoordelijk wordt gehouden voor de massa van deeltjes: het Higgs mechanisme. *Als* het Higgs mechanisme, voorgesteld in 1964 door Higgs, Brout en Englert, inderdaad beschrijft hoe de natuur in elkaar steekt, *dan* moet er een nieuw deeltje bestaan als gevolg hiervan: het Higgs boson.

Het Higgs boson is een instabiel deeltje dat, in principe, geïdentificeerd kan worden door zijn vervalsproducten te bestuderen. Op het moment van schrijven is het Higgs deeltje nog niet geobserveerd bij vorige experimenten noch bij de LHC. Dit komt niet omdat men niet hard genoeg zoekt, maar doordat de massa van het Higgs deeltje helaas buiten het bereik ligt van eerdere deeltjesversnellers. De massa van het Higgs boson wordt niet voorspeld door de theorie. Met de massa van het Higgs boson veranderen ook de verwachte vervalsproducten, of vervalskanalen. *Als* de massa van het Higgs boson bekend zou zijn, *dan* kunnen enkele precieze Standaard Model voorspellingen gedaan worden over de verschillende vervalskanalen en hun relatieve frequenties. De eerste stap is daarom de ontdekking van het Higgs boson. Daarna is de massa bekend en kunnen de precieze Standaard Model voorspellingen getest worden. Deze twee zaken vormden belangrijke motivaties voor het plannen en bouwen van de LHC en zijn vier experimenten, zo'n 25 jaar geleden.

Hoe detecteer je een deeltje dat niet eerder is geobserveerd, met een detector die uniek is, zonder echt te weten waar je moet zoeken? Twee van de vier LHC experimenten, ATLAS en CMS, zijn zogenaamde "algemene" detectoren, gebouwd om een breed scala aan mogelijke fysica signalen te meten, waaronder Higgs verval. In dit proefschrift presenteren we resultaten van een Higgs zoektocht met de Muon Spectrometer van ATLAS. Voordat een dergelijke zoektocht uitgevoerd kan worden is een hoop moeite gedaan om zeker te weten dat de detector zich gedraagt zoals *verwacht*. De enige manier om dit te doen is door gebruik te maken van andere fysica signalen met goed bekende eigenschappen. Met behulp van deze processen kan de detector *gekalibreerd* worden. Door te verifiëren dat de bekende processen gedetecteerd worden zoals verwacht kan met vertrouwen gezocht worden naar nieuwe, en misschien ook *onverwachte*, signalen.

Vanaf dag één met proton-proton botsingen heeft de ATLAS detector zeer goed gepresteerd. De Muon Spectrometer van ATLAS vormt hierop geen uitzondering. De goede prestaties zijn deels te danken aan het werk dat gedaan is met muonen vanuit kosmische straling, voordat er proton-proton botsingen beschikbaar waren. De prestaties van de Muon Spectrometer met muonen van kosmische straling zijn gepresenteerd in Hoofdstuk 4. De relatieve momentum resolutie wordt daarin geparametriseerd als

$$\frac{\sigma_{p_T}}{p_T} = \frac{P_0}{p_T} \oplus P_1 \oplus P_2 \cdot p_T,$$

waarin drie contributies kunnen worden herkend. De onzekerheid van energieverlies correcties wordt genoteerd als P_0, de term van meervoudige verstrooiing als P_1 en de intrinsieke resolutie term als P_2. De waarden zoals verkregen uit fits aan de kosmische stralings data (simulatie) in de barrel regio zijn 0.35 ± 0.02 (0.35) GeV, 0.038 ± 0.001 (0.035) % and $2.0 \pm 0.3\ 10^{-4}$ (1.2) GeV^{-1} voor respectievelijk P_0, P_1 and P_2. De term voor de meervoudige verstrooiing wordt onderschat door een gebrek aan materiaal in de beschrijving van de detector in de simulatie. Voor muonen met een transverse momentum, p_T, lager dan 40 GeV is er een goede overeenkomst tussen data en simulatie. Bij hogere waarden van p_T is er in de data een slechtere resolutie zichtbaar door verschillende oorzaken, waaronder kalibratie, de uitlijning van detector componenten en de beschrijving van het magnetische veld (cf. Hoofdstuk 4).

Verdere detector prestatie studies zijn uitgevoerd met data van proton-proton botsingen. Hoofdstuk 5 geeft de resultaten van onze studies met het $Z \to \mu^-\mu^+$ verval, een van de fysica signalen met goed bekende eigenschappen waar we eerder aan refereerden. De reconstructie efficiëntie is bestudeerd met een zogenaamde "tag-and-probe" methode. De efficiëntie voor gecombineerde muonen in data (simulatie) is 0.960 ± 0.003 (0.966 ± 0.002). De categorie van "tight" muonen heeft een efficiëntie van 0.977 ± 0.003 (0.977 ± 0.002). Deze toename is voornamelijk gelokaliseerd in de $|\eta|$ regio boven de 1.05 en bij $|\eta| \approx 0$. In deze regio's dragen de *tagger* algoritmes bij aan de reconstructie efficiëntie.

Het $Z \to \mu^-\mu^+$ verval is ook gebruikt voor studies naar de momentum schaal en resolutie. Een beschrijving van de di-muon invariante massa is opgesteld en gefit aan simulatie. Vervolgens zijn detector effecten aan de beschrijving toegevoegd en zijn fits aan distributies uit data uitgevoerd. Zowel de momentum schaal als de resolutie zijn bestudeerd voor gecombineerde (CB), standalone (SA) of Inner Detector (ID) track parameters. De momentum schaal voor ID en CB parameters liet een asymmetrie zien in positieve en negatieve endcaps. De asymmetrie wordt voornamelijk toegewezen aan een uitlijnings problemen in de ID. De resoluties voor CB, SA en ID parameters laten allen hogere waarden zien in data, voor alle η regionen. Dit is deels te wijten aan missend materiaal in de detector beschrijving van de simulatie. Verdere uitlijnings problemen en het gebruik van een symmetrische magnetisch veld beschrijving dragen ook bij aan de geobserveerde discrepanties. De resolutie van CB parameters in de barrel regio is in overeenstemming met onze resultaten in kosmische straling data.

De observatie van di-muon eind toestanden in zware-ionen (lood-lood) botsingen zijn gepresenteerd in Hoofdstuk 6 van dit proefschrift. De werkzame doorsnedes van het $J/\psi \to \mu^-\mu^+$ en $Z \to \mu^-\mu^+$ verval zijn bestudeerd als functie van de multipliciteit van deeltjes na de botsing. Een afnemende werkzame doorsnede is geobserveerd voor het J/ψ verval. Het effect is significant sterker dan de statistische en systematische onzekerheden. De afname kan verklaard worden in termen van J/ψ suppressie door het quark-gluon-plasma. In het Z verval is geen afname gezien, hoewel de beperkte statistiek ons weerhoudt van definitieve conclusies in dit geval.

Ten slotte presenteerden we, in Hoofdstuk 7 van dit proefschrift, een zoektocht naar het Standaard Model Higgs boson in een eindtoestand met vier muonen. We hebben hiervoor 1 fb^{-1} van de 2011 ATLAS data-set gebruikt. Figuur 1 laat een van de geobserveerde kandidaten zien. In totaal waren er 10 kandidaten, waar er 5.52 verwacht werden van Standaard Model achtergrond processen. De significantie van dit *teveel* aan kandidaten is geëvalueerd voor mogelijke Higgs massa's van 115-500 GeV. We hebben aangetoond dat er geen ontdekking of uitsluiting geclaimd kon worden. De werkzame doorsnede van het signaal is opgeschaald om te bepalen op welk moment een claim van uitsluiting verwacht wordt. De grootste gevoeligheid is bij een Higgs massa van 200 GeV, waar we verwachten een signaal met 3.5 keer de Standaard Model werkzame doorsnede te kunnen uitsluiten. De geobserveerde limiet bij deze massa is 6.4 keer de Standaard Model werkzame doorsnede. De verdere ontwikkelingen in deze, en andere Higgs zoektochten, zullen spannende volgende stappen zijn in een beslissende fase van de zoektocht naar dit beroemde deeltje. Zal het tijdperk van de Higgs hypothese snel eindigen? De tijd (en LHC data) zal het leren.

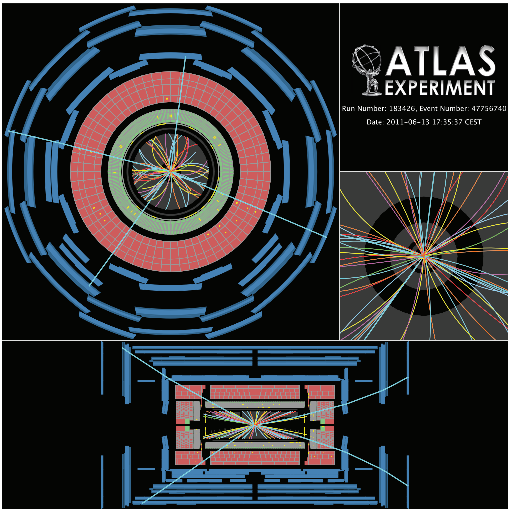

Figuur 1: Een van de Higgs kandidaten zoals geobserveerd in de data.

Acknowledgements

It is time to pay tribute to all people that helped me in putting together this thesis. To do this, I will switch back and forth between English and Dutch. I apologize for the parts in Dutch that you can not understand en het spijt me als er stukken in het Engels zijn die voor u niet te begrijpen zijn.

Mijn tijd op Nikhef bestrijkt inmiddels bijna 5 jaar. Het eerste jaar als Master student vanuit Delft, daarna 4 jaar als onderzoeker in opleiding (oio). Het is bij voorbaat onmogelijk om ieder contact expliciet te bedanken. Daarom nu al excuses aan een ieder die zich vergeten voelt... Voor klachten kunt u zich wenden tot vergeten@eggevanderpoel.com. Dat gezegd hebbende kunnen we beginnen.

Allereerst een woord van dank aan mijn promotor, Frank Linde. Frank heeft naast zijn erg drukke bezigheden nog tijd weten te vinden om de door mij opgeschreven studies van commentaar te voorzien. Zijn hulp is voor mij van grote waarde geweest.

Als u daadwerkelijk de hoofdstukken hiervoor heeft gelezen dan heeft u veel gelezen over muonen. Wie muonen zegt op Nikhef, zegt Peter Kluit. Peter is mijn copromotor en heeft gedurende 4 jaar veel tijd en energie in mijn werk gestoken. Zijn kennis en kunde is voor mij nog steeds van een verbluffend niveau en ik prijs me gelukkig dat hij het vier jaar met mij heeft uitgehouden.

De laatste loodjes van mijn proefschrift ben ik gemotiveerd door de kwinkslagen van Els en Auke-Pieter, waarvoor dank. Voor de Higgs analyse kon ik (onophoudelijk) putten uit de kennis en ervaring van Ivo. Together with Ivo and Antonio C. I managed to do a very nice Higgs analysis that for me is the icing on the cake. I started the analysis on the Thalys to Paris. This trip therefore did not only resulted in witnessing one of the greatest tennis matches ever but also in a nice thesis chapter later on...

Many other ATLAS people have helped me at one point, so I owe you all a big thanks. Especially to the two group leaders, Stan and Paul, I want to say thanks as they do an excellent job in creating and maintaining a nice group of motivated people.

Mijn promotieonderzoek aan muonen in ATLAS staat in een lange traditie van muon proefschriften binnen Nikhef. Al mijn voorgangers ben ik daarom al per definitie schatplichtig. Ik beschouw het als een eer de traditie te hebben mogen voortzetten.

Als oio op Nikhef mag je van geluk spreken dat je met leuke collega's en lotgenoten te maken hebt. Ik heb met veel toffe mensen mogen praten over deeltjes, punk, surfen, reggae, auto's, voetbal, quantumvelden fluctuaties, bowlen en (Duits/Belgisch/Texels) bier. Een (onvolledige) opsomming uit het blote hoofd: Mamanouk en Koutsman, mijn eerste kamergenoten, betekende halfnaakte mannen aan de muur en Russische teksten aan de telefoon. Herrschaft Manuel heeft mij en Saskia ingeleid in de wondere wereld van Genève (en reggae). From Geneva I want to thank the Hamblor, who introduced us to The Boss and Roland Garros. Rikard and Giuseppe were my cool officemates in B54, with the magnificent view on the Mont Blanc. Dr Dox heeft samen met mij de woeste golven op Texel getrotseerd. Gordon was indrukwekkend snel (op het veld welteverstaan). Gossie was de vraagbaak van ATLAS wat betreft Monte Carlo samples en computing (en uitgaan tot ver na de dageraad...). Jochem wist alles over muonen en toen hij weg was nam Zdenko die rol probleemloos over. Hegoi has taught me that it is in fact possible to fall asleep while sitting down (in an ashtray). Met Tristan en Daan heb ik Rijnmondse lol gehad bij het maken van een onvergetelijke TV Rijnmond raportage (hulde aan Justus!). Het mooiste hieraan waren de 34 takes die nodig waren om Tristan mooi met zijn gezicht in een berg sneeuw te zien vallen. Vooral omdat deze scène het uiteindelijk toch niet gered heeft in de montage... Rosemarie heeft gefungeerd als testlezer bij een groot deel van het proefschrift: ontzettend bedankt! Wow, this is taking too long... all the other (former) Nikhef colleagues: thanks for the great time!

Alle NOR en COR leden, bedankt voor de leerzame tijd.

I am grateful to have John and Ido as my paranimfs. I have no doubt in my mind that we will end up having a great time at the defense, or at least at the party...

Ik heb veel fijne nieuwe mensen leren kennen tijdens mijn periode als oio. Helaas heb ik ook afscheid moeten nemen van enkele hele fijne mensen. Dit proefschrift is een eerbetoon aan hen. Voor de steun die ik vanuit Nikhef heb gekregen tijdens deze moeilijke perioden ben ik iedereen, en Teus in het bijzonder, zeer dankbaar.

Ook buiten Nikhef hebben velen te lijden gehad onder mijn werk. Veel familieleden en vrienden die op iedere verjaardag wéér dat verhaal over dat Higgs deeltje moesten aanhoren... Of niet, als ik er (weer) eens niet was... Dank voor jullie geduld en (geveinsde) interesse. Dank ook voor alle fantastische momenten die helemaal niks met muonen of het Higgs deeltje te maken hadden. De mooie voetbalwedstrijden, verjaardagsfeestjes (al dan niet verkleed), wintersport reizen (al dan niet verkleed), Ardennen uitjes (al dan niet verkleed), derde kerstdagen, vierde kerstdagen, jaarwisselingen (al dan niet verkleed), etc... Alle vriendjes en vriendinnetjes, apen en apinnen, bedankt!

Daniel Karso wil ik expliciet bedanken voor de cover: hij schopt behoorlijk kont!

Een groot woord van dank ook aan de PP'ts: AvdE, EvdE, EK en RKvdB. Jullie zijn kanjers en wat hebben we genoten!

Mijn ouders ben ik dankbaar voor het feit dat ik een goede opleiding heb mogen genieten. Zonder hun steun was dit natuurlijk nooit mogelijk geweest.

Mama, bedankt voor je vele kleurrijke bijdragen aan mijn leven.

Papa, bedankt voor je (wiskundige) nieuwsgierigheid en je adviezen.

Lieve Matthijs, Yolande en Isa, bedankt voor de warmte die jullie mij geven. Dit heeft me op enkele moeilijke momenten heel veel geholpen.

Lieve Tessa, je blijft mijn kleine zusje en ik ben trots op hoe je bent. En al moest ik er aan wennen, je kan een heerlijk biertje tappen hoor!

Lieve Sas, jij hebt misschien nog wel het meest moeten lijden onder mijn onderzoek. Maar je hebt me altijd omringd met je onvoorwaardelijke liefde. Bedankt daarvoor. Ik hoop dat we nog heel lang net zoveel samen genieten en lachen als de afgelopen 12 jaren!

You know how the time flies
only Yesterday was the time of our lives

Adele - Someone like you